

**The Influence of Electron Beam Welding
Parameters on Heat Affected Zone
Cracking in AllVac 718Plus Alloy**

by

Qiang Li

Thesis submitted to the Engineering Faculty of the University of
Manitoba for the degree of

Master of Science

in

Mechanical and Manufacturing Engineering

Dr. M.C. Chaturvedi Chairman

Dr. N.L Richards

June 5, 2006

Department of Mechanical and Manufacturing Engineering

Winnipeg, Manitoba

Copyright © 2006 by Qiang Li

**THE UNIVERSITY OF MANITOBA
FACULTY OF GRADUATE STUDIES

COPYRIGHT PERMISSION**

**The Influence of Electron Beam Welding
Parameters on Heat Affected Zone
Cracking in AllVac 718Plus Alloy**

BY

Qiang Li

A Thesis/Practicum submitted to the Faculty of Graduate Studies of The University of

Manitoba in partial fulfillment of the requirement of the degree

OF

MASTER OF SCIENCE

Qiang Li © 2006

Permission has been granted to the Library of the University of Manitoba to lend or sell copies of this thesis/practicum, to the National Library of Canada to microfilm this thesis and to lend or sell copies of the film, and to University Microfilms Inc. to publish an abstract of this thesis/practicum.

This reproduction or copy of this thesis has been made available by authority of the copyright owner solely for the purpose of private study and research, and may only be reproduced and copied as permitted by copyright laws or with express written authorization from the copyright owner.

ACKNOWLEDGMENTS

I would like to express my greatest appreciation to my supervisor, Dr. M.C. Chaturvedi, for giving me the opportunity to study this interesting project and his instruction, timely suggestion, encouragement and support. I appreciate Dr. N.L. Richards for his help and suggestion in my research work.

I acknowledge Allvac Inc. for providing the materials and the relevant reports, and Bristol Aerospace for implement electron beam welding.

Sincere gratitude is extended to John Van Dorp, Don Mardis, Dan McCooeye and Mike Boskwick for their technical assistance.

I express my warm appreciation to Dr. K Mount in the department of statistics for helping me to do statistical analysis.

I would like to thank Dr. R. G. Ding, Dr. O. A. Ojo, Dr. Y. L. Wang, Dr. R. Sidhu and Dr. L. Xiao for their help and significant discussion. Thanks are given to Ms Vishwakarma, Mr. Q. Y. Li, Mr. Seun and Mr. Dotun for their assistance.

I appreciate Prof. R. Schilling and Dr. J.R. Cahoon for their help and encouragement during my academic life at the University of Manitoba.

Finally, I would like to thank my wife S. L. Sui and my son G. Y. Li for their patience, love, understanding and continuous encouragement throughout my studentship at the University of Manitoba.

The Influence of Electron-Beam Welding Parameters on Heat- Affected-Zone Cracking in AllVac 718Plus Alloy

by

Qiang Li

(ABSTRACT)

AllVac 718Plus alloy is a new nickel base superalloy with better mechanical properties at elevated temperature, which was recently developed by AllVac Inc. In this study, the influence of Electron-Beam (EB) welding parameters on Heat-Affected-Zone (HAZ) cracking in AllVac 718Plus alloy was investigated. The welding was done with electron-beam-welding equipment at Bristol Aerospace. Sixty groups of welding parameters varying in beam current, welding speed and oscillation amplitude in longitudinal and cross directions were designed to study the effect of welding parameters on the weldability of AllVac 718Plus alloy. The average total crack length in eight cross sections of a weld and its HAZ area were measured by

means of an optical microscope with image analysis system. The crack index (CI) i.e. the crack length per HAZ area, was used to evaluate the HAZ cracking tendencies of the alloy. Cracks distributions and morphologies as well as microstructure changes in HAZ were also examined by using the Scanning Electron Microscope (SEM). Typical precipitates in base metal and the HAZ of welds were also observed through the Transmission Electron Microscope (TEM). The experimental results showed that (1) Small γ phases (diameter in range of 1-3 nm) were distributed homogenously in the matrix of the base metal heat-treated at 950⁰C /1h and quenched into water. (2) Acicular δ phase particles were observed along grain boundaries in the matrix. (3) All of the cracks in the HAZ were along the grain boundaries. (4) The welding crack indexes of the alloy decreased rapidly with increase in heat input rate during welding. (5) The dissolution of δ phases occurred in the region close to the Fusion Zone (FZ). (6) Statistical analysis indicated that welding velocity and beam current among the varied four welding parameters play a key role in determining the HAZ cracking of welds in the EM welding process. Based on the analysis of temperature and temperature gradient in the HAZ, the effects of welding speed and beam current on the HAZ cracking are discussed.

Table Contents

Table 2-1	Chemical compositions of Inconel 718 and Allvac 718Plus alloys	37
Table 2-2	Critical phase transformation temperatures of Allvac 718Plus alloy	39
Table 3-1	Chemical compositions of Allvac 718 Plus alloy (wt.%)	41
Table 3-2	Critical Phase Transformation Temperature of Allvac 718Plus Alloy	41
Table 3-3	Electron beam-welding parameters.	45
Table 4-1	Measured and calculated distance of (h k l) plane of Laves phase	51
Table 4-2	Measured crack lengths and geometric parameters of EB welds	72
Table 4-3	Multiple regression analysis results-A	65
Table 4-4	Multiple regression analysis results-B	66
Table 4-5	Multiple regression analysis results-C	67

Figure Captions

Fig. 2-1	Schematic diagram of electron-beam welding process	7
Fig. 2-2	Moving coordinate system	12
Fig. 2-3	Schematic diagram of ductility change with temperature	23
Fig. 2-4	Cylindrical particle	25
Fig. 4-1	SEM micrograph showing the microstructure of the base metal of Allvac 718Plus alloy after solution-heat treatment	76
Fig. 4-2	Delta phase morphology around grain boundary in the base metal of Allvac 718Plus alloy after solution-heat treatment. a) SEM micrograph b) TEM micrograph (BF) with diffraction pattern, and c) EDS and the compositions of delta phase by TEM	77 78
Fig. 4-3	DF image of small γ' phase in the base metal taken with FEG TEM	79
Fig. 4-4	Second phase [NbX(B,C)] being in a grain (a) and on a grain boundary	80
Fig. 4-5	Schematic diagram showing factors affecting the HAZ cracking in welding	82
Fig. 4-6	A typical nail-head shape of weld obtained with EB welding and its geometrical parameters	83
Fig. 4-7	SEM micrograph illustrating cracks distribution in HAZ of an EB weld	84
Fig. 4-8	SEM micrographs illustrating cracks with the resolidified-products and the compositions of the resolidified-products from EDS	85
Fig. 4-9	SEM micrograph showing a crack without the resolidified-products	86

Fig. 4-10	SEM micrograph (a) showing the resolidified products on a grain boundary in HAZ, EDS analysis (b) demonstrated the resolidified products rich in Nb.	87
Fig. 4-11	TEM micrograph showing Laves phase in HAZ extracted on carbon replica (a) morphology along GB, (b) and (c) diffraction patterns from zone axes of $[14\bar{1}]$ and $[\bar{5}1\bar{2}]$ respectively, (d) EDS.	88
Fig. 4-12	TEM micrograph showing the morphology of carbides in HAZ extracted on carbon replica with indexed diffraction pattern and compositions from EDS	89
Fig. 4-13	SEM micrographs showing the delta phase dissolution in the region close to fusion line in HAZ	90
Fig. 4-14	SEM micrographs showing the triple GB without delta phase in HAZ (a) and (b) taken in different directions and the relative rotation angle between (a) and (b) is about 15°	91
Fig. 4-15	TEM micrographs showing the triple GB without delta phase in HAZ (a) and (b) taken in different directions and the relative rotation angle between (a) and (b) is about 15°	92
Fig. 4-16	Solidification constitution diagram for Inconel 718 from ref.[43]	93
Fig. 4-17	X-ray mapping revealing cracking occurred along B/Nb rich particles	94
Fig. 4-18	SEM micrograph shows a crack connected with two particles, EDS analysis showing one particle being rich in Nb, the being rich in Ti	95
Fig. 4-19	The top width of weld increases linearly with an increase of heat input rate (Q) in EB welding process	96

Fig. 4-19	The product of top width time depth of welds linearly increasing with heat input rate	97
Fig. 4-20	The crack index (CI) decreasing rapidly with an increase in heat input rate (Q) in EB welding process	98
Fig. 4-21	The CI decreasing rapidly with an increase in heat input rate when the oscillations were kept constant (a) $A_{mx}=A_{my}=50$, (b) $A_{mx}=A_{my}=25$	99
Fig. 4-22	The relation between the CI and the oscillation score factor along tow directions when the other parameters are unchangeable (a) CI vs A_{mx} , (b) CI vs A_{my}	100
Fig. 4-23	The top width of weld is not changed with the variation of oscillation score factor when the heat input rate is 261.7 J/mm (a) the oscillation score factor along the cross direction is a constant of 50, (b) the oscillation score factor along the longitudinal direction is a constant of 50	101
Fig. 4-24	Diagrams showing the CI increasing with EB welding velocity when the other three parameters are kept at the constant, (a) beam current is 67.5mA, $A_{mx}=A_{my}=25$, (b) beam current is 85mA, $A_{mx}=A_{my}=50$, (c) beam current is 102.5mA, $A_{mx}=A_{my}=25$.	102 103
Fig. 4-25	Diagrams showing the CI decreasing slightly with an increase of beam current when the welding velocity is unchangeable, (a) welding velocity is 22.5in/min. (b) welding velocity is 35 in/min. (c) welding velocity is 47.5in/min.	104 105

Fig. 4-26	The plot of residual versus predicted CI	106
Fig. 4-27	Electron beam oscillation amplitude vs score factor [68].	107
Fig. 4-28	(a) computed temperature distribution in HAZ at the neck of welds obtained in different welding velocities, (b) computed temperature gradient changes with respect to the distance from the fusion line	108

Contents

Acknowledgments	ii
Abstract	iii
Table contents	v
Figure caption	vi
Chapter 1: Introduction	1
1.1. Background	1
1.2. The Purposes of The Present Study.....	2
1.3. The Contributions of This Thesis.....	3
Chapter 2: Literature Review	4
2.1. The Characteristics of Electron Beam Welding.....	4
2.1.1. Definition of Electron Beam Welding.....	4
2.1.2. History of Electron-Beam Welding Development.....	5
2.1.3. Features of Heating by an Electron Beam	6
2.1.3.1. Operation of an Electron Beam Welder.....	6
2.1.3.2. Electron Beam Heating Work-piece.....	7
2.1.3.3. The Control of Welding Parameters.....	8
2.1.4. Advantages of Electron-Beam-Welding.....	8
2.1.5. Electron Beam Welding Limitations.....	9
2.2. Formation of Heat-Affected-Zone	10

2.2.1. Temperature Gradient.....	10
2.2.1.1. Fusion Zone	10
2.2.1.2. Heat Affected Zone.....	10
2.2.1.3. Temperature Field around a Weld.....	11
2.2.1.4. Temperature Gradient	16
2.2.2. Temperature Gradient.....	17
2.2.3. Thermal Tensile Stress Formation and Distribution.....	17
2.3. Cracks Formation in HAZ.....	18
2.3.1. Fracture of Metal Structure.....	19
2.3.1.1. Fracture Mechanism.....	19
2.3.1.1.1. Microvoid Coalescence.....	20
2.3.1.1.2. Cleavage.....	21
2.3.1.1.3. Intergranular Fracture.....	22
2.3.1.2. Fatigue Failure.....	22
2.3.1.3. High-temperature Mechanical Properties of Metals.....	23
2.3.2. Stress Concentration.....	24
2.3.2.1. Microcrack.....	24
2.3.2.2. Inclusions.....	24
2.3.2.3. Grain Boundaries.....	26
2.3.3. Strengthening of Superalloys	27
2.3.4. Solidification Cracking of Weld.....	28
2.3.5. HAZ Cracking of Welds.....	29
2.3.6. Segregation	33
2.3.7. Eutectic Structure and Brittle Phases in HAZ of Welds.....	35

2.4. Inconel 718 and AllVac 718Plus Alloy.....	36
2.4.1. The Features and Application of Inconel 718 Alloy	36
2.4.2. The Features of Allvac 718Plus Alloy.....	38
2.4.2.1. The Microstructure of Wrought AllVac 718Plus Alloy.....	38
2.4.2.2. Phase Transformation Temperatures.....	38
2.4.2.3. Solution Treatment	39
2.4.2.4. Characteristics of Grain Boundaries.....	39
Chapter 3: Experimental Procedure.....	40
3.1. Materials.....	40
3.2. Electron Beam Welding Conditions.....	42
3.3. Specimen Preparation.....	42
3.4. Microscopic Examinations	44
Chapter 4: Results and Discussion.....	47
4.1. Microstructure of the Base Metal.....	47
4.2. HAZ Cracking.....	48
4.3. Microstructural Characteristics of HAZ Cracking.....	49
4.3.1. Grain Boundary Liquation.....	50
4.3.2. Delta Phase Dissolution.....	52
4.3.3. Mechanism of Grain Boundary Liquation Cracking.....	53
4.3.4. Effect of Trace Elements on HAZ Cracking.....	56
4.3.5. Effect of Particles on Grain Boundaries on HAZ Cracking.....	58
4.4. Crack Length Measurement.....	59
4.5. Effects of Welding Parameters on Weld Shape and Crack Index	60

4.5.1. Heat Input Rate.....	60
4.5.2. Effect of Electron Beam Oscillations.....	61
4.5.3. Effect of Welding Velocity.....	62
4.5.4. Effect of Electron Beam Current.....	63
4.5.5. Multiple Linear Regression Analysis.....	64
4.6. Evaluation of Temperature Distribution and Temperature Gradient in the HAZ.....	67
Chapter 5: Conclusions.....	109
Chapter 6: Future Work.....	112
References.....	114

Chapter 1

Introduction

1.1. Background

AllVac 718Plus alloy is a new modified 718-type alloy, which was developed recently by the AllVac Company. The main difference between Allvac 718 Plus alloy and Inconel 718 alloy is principal strengthening phase, the former is γ phase (ordered FCC); the latter is γ' phase (BCT). The thermal stability of γ phase is much better than that of γ' phase. Allvac 718Plus possesses a 55⁰C higher temperature capability than Inconel 718 alloy, and the acceptable mechanical properties and thermal stability at elevated temperature because of modification of the ratio of aluminum to titanium and the addition of cobalt up to 9wt% [1]. Therefore, this alloy has great potential in aerospace and industrial applications. The weldability of this alloy is very important to the industrial application.

Generally, superalloys are difficult to weld due to their high amount of alloying elements, low thermal conductivities and rapid temperature change during welding. Cracking usually occurs around welds of superalloys, i.e. the heat-affected-zone (HAZ) cracking and the fusion-zone (FZ) cracking. The HAZ cracking of Inconel 718 alloy has been extensively investigated in different welding manners such as electron beam welding and gas tungsten arc welding (GTAW) [2-12].

Electron beam welding is widely used to join and repair superalloy components in aerospace industry. Regarding the HAZ cracking of welds of superalloys, Richards et al. [4, 13] have found that the electron beam welding speed is the most significant factor in affecting the HAZ cracking of Inconel 718 alloy, and both welding speed and beam current affect the HAZ cracking of wrought Incoloy 903. The effect of electron beam welding parameters on the HAZ cracking of this new alloy is a significant research project.

1.2. The Purposes of The Present Study

In the present study, the wrought plate of Allvac 718Plus alloy was welded using electron beam welding method. Sixty groups of welding parameters in variation of beam current (I), welding speed (V) and oscillation amplitude in longitudinal (A_{mx}) and cross directions (A_{my}) are designed to study the effect of welding parameters on the weldability of AllVac 718Plus alloy.

The objectives were:

- (1) To examine the relationship between intergranular cracking and microstructure evolution in the HAZ of welds
- (2) To understand the HAZ cracking process involved in crack initiation and propagation by means of microstructural examinations.
- (3) To study the effects of electron beam welding parameters on the HAZ cracking of welds, and then to find optimum an electron beam welding condition for this new alloy.

1.3. The Contributions of This Thesis

In this study, 480 sections from 60 welds were observed, and approximately 10 thousands crack lengths in HAZ of welds were measured. The experimental results showed that (1) all the cracks in HAZ were along grain boundaries. The grain boundary liquation was associated with the majority of the HAZ cracking during welding. (2) Dissolution of acicular δ phase around grain boundaries in HAZ caused the reduction of melting temperature of the grain boundaries, enhancing grain boundary liquation cracking. (3) The welding velocity and beam current were the most significant welding parameters affecting the HAZ cracking of this alloy, and cracking index of this alloy decreased rapidly with the heat input rate during welding. (4) The minimum crack index was obtained when the heat input rate was kept at the maximum. (5) On the basis of plane heat source model, the temperature gradients across HAZ at different welding velocities were quantitatively evaluated, and were used to explain the effect of welding velocity on the HAZ cracking of weld in the electron beam welding process.

Chapter 2

Literature Review

2.1. The Characteristics of Electron-Beam-Welding

2.1.1. Definition of Electron Beam Welding

Electron-Beam-Welding (EBW) is a high energy density fusion welding process that is carried out by bombarding the joint with an intense beam of electrons with high velocity of $0.3\sim 0.7C$ (C is the velocity of light). The high kinetic energy of these electrons is converted into heat as they impact the workpiece on which they are impinging, causing the joining interfaces to melt and produce the desired weld-joint

coalescence. Electron-Beam-Welding is employed to weld most metals that can be welded using arc welding [14].

2.1.2. History of Electron-Beam Welding Development

In November of 1957, Dr. Stohr reported his initial research work that resulted in the electron-beam welding technique. At the first stage, electron-beam welding could only be done in vacuum. In the following decade, intensive development works were carried out. In 1958, first commercial equipment was made, and in 1959, welds with a large depth-to-width ratio made by EBW were first reported. As developments continued, two main electron accelerating systems evolved: (1) a low-voltage electron beam system, which uses accelerating voltage in the range of 30 kV to 60 kV, and (2) a high-voltage system with accelerating voltages in the 100 kV range. However, the higher voltage system emits more X-rays than the lower voltage system. Currently, three distinct modes of EBW are employed in industrial applications [15].

- (1) High-Vacuum (EBW-HV), where the workpiece is in a vacuum chamber with pressure ranging from 0.13 to 0.30 mPa.
- (2) Medium-Vacuum (EBW-MV), where the workpiece may be in a partial vacuum ranging from 0.13 to 3300Pa.
- (3) Non-vacuum (EBW-NV), which is also referred to as atmospheric pressure in air or in an inert gas.

2.1.3. Features of Heating by an Electron Beam

2.1.3.1. Operation of an Electron Beam Welder

As shown schematically in Fig.1, the EB system consists of an electron beam gun, a power supply and control system, and work-piece motion system enclosed in a vacuum chamber. In EB welding process, filler metals are often not needed because of the melting of the base metal. The work-piece to be welded is in a vacuum chamber therefore shielding gases are also not required. The electron beam gun has a tungsten filament that is heated by the passage of a current and electrons are produced by thermion. These thermal electrons are accelerated from the gun by a high voltage potential between the cathode and the anode. The flow of electrons then goes through a hole in the anode. Lorentz forces lead the beam from focusing and deflecting coils. This beam is directed out of the gun column and impacts the workpiece. The kinetic energy of the moving electrons is converted to thermal energy upon impact of the workpiece and makes a hole in the material to be welded. The metal around the hole is molten. Then, the molten metal fills in behind the beam, creating a deep finished weld. The flow of electron beam and the work-piece are manipulated within the vacuum welding chamber by a computer controlled system, therefore eliminating oxidation and contamination.

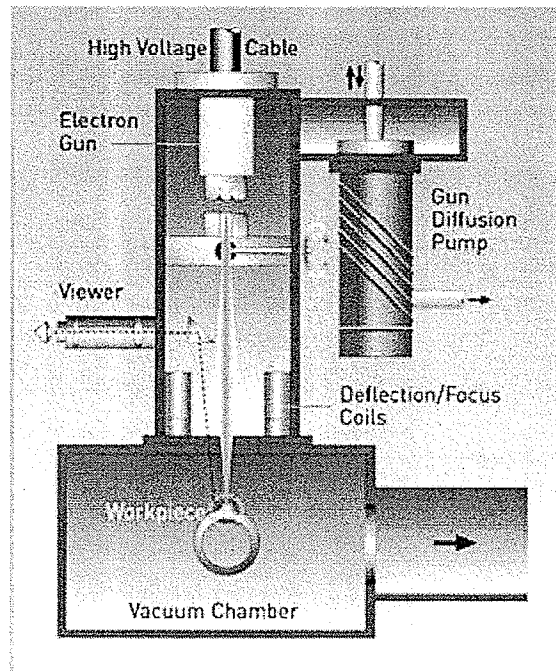


Fig.2-1 Schematic diagram of electron-beam welding process

2.1.3.2. Electron Beam Heating Work-piece

Because the total kinetic energy of the accelerated electrons can be concentrated onto a very small spot on the workpiece, power densities as high as 10^{12} W/m^2 can be obtained. The high power density with extremely small intrinsic penetration of the electrons in the workpiece results in almost instantaneous local melting and vaporizing of the workpiece material, which distinguishes EBW from other welding methods, such as Gas-Tungsten-Arc-Welding (GTAW), in which the rate of melting is limited by thermal conduction. Typically, high-vacuum EBW beams can be focused down to spot diameters in range of 0.25 to 1.3mm, with a power density of 10^{11} W/m^2 . This electron beam with

such a high power density generates temperatures of approximately 14,000 °C, which is sufficient to vaporize almost any material, forming a vapor hole that penetrates deep into the workpiece.

2.1.3.3. The Control of Welding Parameters

The thermal energy input during electron beam welding is controlled by four main variables:

- (1) The beam current, i.e. the number of electrons per second hitting the workpiece.
- (2) The electron velocity, which is dependent of the accelerating potential.
- (3) The size of the beam at or within the workpiece, i.e. the beam spots size.
- (4) The welding speed, i.e. the moving speed of the electron beam relative to the workpiece.

Since the electron beam has deep penetrating characteristics with a lower heat input than the arc welding methods, the heat-affected zone around EB welds is much smaller than that which is produced by any arc welding process. In addition, because of the almost parallel sides of the weld nugget, distortion is greatly minimized, and the cooling rate is much higher.

2.1.4. Advantages of Electron-Beam-Welding

Welds made by means of EBW are usually deeper and narrower than arc welds. The total heat input in EBW is much lower than that required in arc welding. EBW also leads to a high ratio of weld depth to width, and eliminates the need for multiple-pass welding

as is needed in arc welding. The lower heat input results in a narrow heat-affected-zone (HAZ), and noticeably fewer thermal effects on the workpiece.

A high-purity vacuum environment can be used for EB welding, which results in freedom from impurities such as oxides and nitrides. The other advantages are listed below [16]:

- 1) Maximum amount of weld penetration with the least amount of heat input reduces distortion.
- 2) Electron beam welding often reduces the need for secondary operations.
- 3) Repeatability is achieved through electrical control systems.
- 4) A cleaner, stronger and homogeneous weld is produced in a vacuum. The electron beam machine's vacuum environment eliminates atmospheric contaminants in the weld.
- 5) Exotic alloys and dissimilar materials can be welded.
- 6) Extreme precision due to computer control and magnification of the welding site.
- 7) Electron beam welding frequently yields a scrap rate.
- 8) The electron beam process can be used for the repair of used components.

2.1.5. Electron Beam Welding Limitations

One of the limitations of the electron beam process is its high capital cost. The price of the equipment is very high. It is also expensive to operate because of the need for vacuum pumps. In addition, fit-up of the workpiece must be precise and locating the parts

with respect to the beam must be perfect. The necessity to use a vacuum chamber limits the workpiece size.

2.2. Formation of Heat-Affected-Zone

2.2.1. Temperature Gradient

2.2.1.1. Fusion Zone

Electron-Beam-Welding is a fusion welding process. The zone in a workpiece bombarded by electron beam is easily melted due to high-density input power. This zone is referred to as fusion zone. The size of fusion zone depends on the electron beam size, the input power (voltage and current) and the oscillation amplitude. During the welding, the temperature in fusion zone does not vary greatly [17].

2.2.1.2. Heat Affected Zone

The temperature in fusion zone increases to above the melting point in a short time. As a result of this rapid temperature rise, the original microstructure and properties of the metal in region close to the fusion zone are changed. This zone of metal is usually referred to as the Heat-Affected Zone (HAZ). Generally, the HAZ can be conveniently divided into different sub-zones such as grain growth zone, recrystallized zone, partially transformed zone and tempered zone. The formation of these zones will vary from metals to another [17].

2.2.1.3. Temperature Field around a Weld

Fusion welding is a complex process, which involves many dependent variables that control the final microstructure and the mechanical properties of the weld. The thermal cycles produced by the moving heat source lead to physical state changes, metallurgical phase transformation, and transient thermal stress and metal movement. After welding is completed, the weld may contain (1) physical discontinuities due to excessively rapid solidification of the melted metal, (2) averse microstructures that are due to inappropriate cooling, (3) residual stresses and distortion due to the existence of incompatible plastic deformation. These problems are directly related to the welding heat-flow. Therefore, a heat-flow analysis is necessary for a complete understanding of the fusion welding process in order to control and produce defect-free welds [18].

Many investigators have done welding heat-flow modeling and analysis, based on the conduction equation for heat flow [18].

$$\nabla \cdot (\lambda \nabla T) + \rho C_p v \frac{\partial T}{\partial w} + \dot{Q} = \rho C_p v \frac{\partial T}{\partial t} \quad (2-1)$$

The initial condition is:

$$T = T_0, \text{ at } t = 0 \quad (2-2)$$

And the general boundary condition is

$$\lambda \left(\frac{\partial T}{\partial w} l_w + \frac{\partial T}{\partial y} l_y + \frac{\partial T}{\partial z} l_z \right) - \dot{q} + h(T - T_\infty) = 0 \quad (2-3)$$

Where, ∇ is a differential operator; T is the temperature; T_∞ is the environmental temperature; T_0 is the initial temperature; λ is the thermal conductivity; ρ is the density; C_p is the specific heat; h is the surface heat-loss coefficient; l_w , l_y and l_z are the direction

cosines of the boundary surface; \dot{Q} is the volumetric heat source, t is time and v is welding speed.

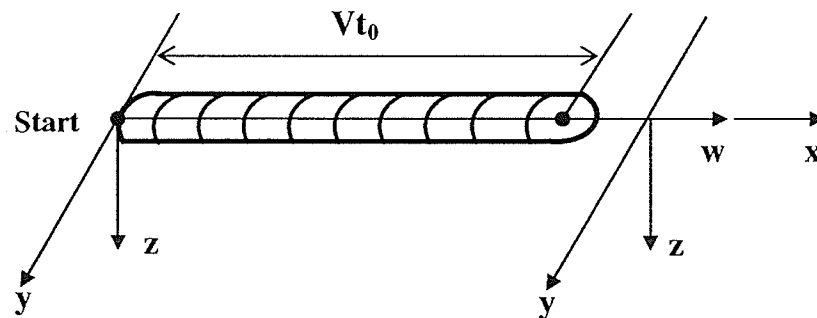


Fig.2-2 Moving coordinate system

For different kinds of welding, heating modes are different and the heat source formulation is also different. Additionally, the general solutions of Equation (2-1) are dependent on the geometrical parameters of the weld piece such as thickness and width. In most cases, the boundary surfaces are assumed to be adiabatic, and the thermal properties are independent on temperature. The various metallurgical zones in the weld are assumed to be homogenous and the thermal model is linear.

Passoja [19] simplified the problem by making the following assumptions:

- (1) An orthogonal, x,y,z coordinate system is placed on the solid such that the electron beam corresponds to the z -axis and moves along the x -axis.
- (2) Heat flow in the z -direction is negligible.
- (3) The solid is semi-infinite; i.e., $y \gg x$.

- (4) An arbitrary reference point, X_r is chosen along the axis.
- (5) No heat enters or leaves the reference point before the beam crosses the reference point.
- (6) The heat source is a stable plane source.

So, the equation (2-1) is simplified to the following

$$\frac{\partial T}{\partial t} = \frac{\lambda}{C_p \rho} \nabla^2 T; \quad \text{i.e.} \quad \frac{\partial T}{\partial t} = \alpha \frac{\partial^2 T}{\partial y^2} \quad (2-4)$$

Where, $\alpha = \lambda / (C_p \rho)$

The boundary conditions are:

$$T = T_B \quad -\frac{H}{2} \leq Y \leq \frac{H}{2} \quad \text{for} \quad t \leq 0 \quad (2-5a)$$

$$T = T_R \quad \frac{H}{2} \leq |Y| \quad \text{for} \quad t \leq 0 \quad (2-5b)$$

$$T = T(y, t) \quad -Y < 0 < Y \quad \text{for} \quad t > 0 \quad (2-5c)$$

Therefore, the solution of the heat flow equation is

$$T(Y, t) - T_R = \frac{(T_B - T_R)H}{2\sqrt{\pi\alpha t}} \exp\left(\frac{-Y^2}{4\alpha t}\right) \quad (2-6)$$

Where, H = the source width in mm, Y = the distance from the source center line in mm, T_B = the beam temperature in °C, T_R = the ambient temperature in °C, α = thermal diffusivity in mm^2/s .

Considering the heat source movement, Cho and Chin [18] employed the condition that the temperature on the liquid-solid interface is the melting temperature T_m . The temperature for thin plate can be expressed as:

$$T - T_R = B_z \exp\left(\frac{-vw}{2\alpha}\right) K_0\left(\frac{vr}{2\alpha}\right) \quad (2-7a)$$

$$B_z = \frac{(T_m - T_R) \exp\left(-\frac{vr_B}{2\alpha}\right) \left[\frac{K_0(vr_B/2\alpha)}{K_1(vr_B/2\alpha)} \right]}{K_0(vr_B/2\alpha)} \quad (2-7b)$$

The bead width is

$$h = 2r_B \left\{ 1 - \left[\frac{K_0(vr_B/2\alpha)}{K_1(vr_B/2\alpha)} \right]^2 \right\}^{0.5} \quad (2-7c)$$

Where, $r = (w^2 + y^2 + z^2)^{1/2}$, K_0 is a modified Bessel function of the second kind of zeroth order and K_1 corresponds to first order.

Recently, Binda et al. [20] proposed a semi-empirical mode of the temperature field in the laser weld of AISI 304 steel. If the heat rate varies along the thickness (z-direction), the temperature field changes with Z, which can be expressed by the following equation,

$$T(w, y, z) - T_R = \frac{1}{2\pi k} \exp\left(\frac{-vw}{2\alpha}\right) \sum_0^N A_n \cos \frac{\pi n z}{g} \times K_0\left(r \sqrt{\left(\frac{v}{2\alpha}\right)^2 + \left(\frac{\pi n}{g}\right)^2}\right) \quad (2-8)$$

Where, k is the thermal conductivity(W/m °C), g is the thickness of the plate. Considering the characteristic of the Bessel function, they obtained an approximate expression for the temperature field:

$$T(w, y, z) - T_R = \frac{1}{2\pi k} \exp\left(\frac{-vw}{2\alpha}\right) \sum_0^N A_n \cos \frac{\pi n z}{g} K_0\left(\frac{rv}{2\alpha}\right) \quad (2-9)$$

From equation (2-9), the temperature field could be calculated if only the A_n coefficients, which describe the heat rate, are known. Binda et al analyzed and measured the thermal

features of laser beam welding. The relationship between A_n ($n = 0, 1, 2, 3$), heating power (P) and welding speed (v) as well as focal height (h_f) was given by:

$$A_n(P, h_f, v) = 1015 + 546 \left(\frac{1-n}{n^2+1} \right) P + 57.6 \left(\frac{1-2n}{n+1} \right) h_f + \frac{125v}{n+1} \quad (2-10)$$

From equations (2-6), (2-7) or (2-9) and (2-10), the temperature fields and the corresponding temperature gradient along a certain direction around the welds can be easily calculated.

On the other hand, the finite difference method and the finite element analysis have been widely used to calculate the temperature fields and residual stresses around the welds [21-33]. For example, Pevelic et al. [21] proposed a finite-difference method to evaluate the temperature distribution in a 2-D plate using a line heat source. The shape of the melt pool was correlated with the welding variables, and the isotherm was used as a boundary condition. The analytical peak temperature was consistent with the experimental value. Friedman and Gilickstein [22] developed a FEM analysis for transient heat conduction to investigate the effect of a number of welding parameters, such as the magnitude of heat input from the arc, the distribution of the heat input over the surface of the weld, and the duration of the heat input on the thermal response characteristics of the weld shape and the depth of penetration. They verified the potential for calculating the optimum combination of welding parameters for a given weld joint. Feng et al. [23] developed a finite element model to quantitatively evaluate the local thermomechanical conditions for weld metal solidification cracking. They constructed a diagram consisting of the stress, temperature and location to reveal the local stress development behind the traveling pool. Their investigation was concerned with the

solidification cracking in the fusion zone. Choi and Mazumder [24] analyzed the Gas Metal Arc Welding (GMAW) process by means of combination of a finite thermomechanical model for temperature and stress with the solidification model. Their temperature and stress fields were obtained analytically and experimentally. Generally, the temperature gradient was in the range of 10^4 - 10^5 K/m when the welding power was 6kW, and the welding speed was 3.39 to 7.62mm/s. Yang et al. [25] established an FEM model for calculating the temperature and residual stress fields in medium-high carbon steels. It was verified that the calculated temperature and residual stress fields fit the measured values very well. Ferro et al. [26] also developed an FEM model to simulate the fusion shape for electron-beam welding. The results showed that thermal and residual stresses were influenced by the shape of the fusion zone, and the highest thermal tensile stress arose under the head part of the nail shaped fusion zone, as produced by EB welding.

2.2.1.4. Temperature Gradient

In a fusion welding process, the temperature in the fusion zone can be raised highly above the melting point of the metal in a very short time. However, the base metal around the fusion zone is kept at an ambient temperature. This process results in a temperature gradient around the weld. From the temperature fields, $T(X, Y, Z)$, the temperature gradient vector (∇T) can be obtained by the following,

$$\nabla T = \frac{\partial T}{\partial X} \vec{i} + \frac{\partial T}{\partial Y} \vec{j} + \frac{\partial T}{\partial Z} \vec{k} \quad (2-11)$$

2.2.2. Temperature Gradient

From section 2.2.1.3, it is known that the temperature fields around a weld or in HAZ depend on the characteristic of the heating source and the thermal conductivity of the base metals. Passoja's analysis [19] showed that the wider the bead width (h), the steeper the temperature gradient. According to the expression of temperature fields obtained by Binda et al. [20], the temperature gradient increases with heating power during welding, but the temperature gradient is a complex function of welding velocity.

2.2.3. Thermal Tensile Stress Formation and Distribution

Thermal stresses exist whenever the temperature gradients are present in materials. Different temperatures produce different expansions and subject materials to interior stresses. After the determination of the temperature fields around the weld, the thermal stresses can be obtained via thermo-mechanical analysis. Zhu and Chao [27] carried out a three-dimensional non-linear thermal and thermo-mechanical numerical simulation of the friction stir welding of 304 stainless steel. The plastic deformation of the materials was assumed to obey the von Mises yield criterion and the associated flow rule, and the relationship of the strain rate ($\dot{\epsilon}_{ij}$) with thermal stress rate ($\dot{\sigma}_{ij}$) and temperature rate (\dot{T}) was expressed as:

$$\dot{\epsilon}_{ij} = \frac{1-\nu}{E} \dot{\sigma}_{ij} - \frac{\nu}{E} \dot{\sigma}_{kk} \delta_{ij} + \chi s_{ij} + \left[\xi + \frac{\partial \xi}{\partial T} (T - T_0) \right] \dot{T} \quad (2-12)$$

Where, E is the Young's modulus, ν is the Poisson's ratio, ξ is the thermal expansion coefficient, $s_{ij} = \sigma_{ij} - 1/3 \sigma_{kk} \delta_{ij}$ are the components of deviatoric stress and χ is the

plastic flow factor, $\chi = 0$ for elastic deformation, and $\chi > 0$ for plastic deformation. This equation (2-12) can be solved by FEM.

However, residual stresses are due to the manufacturing processes. Welding leaves residual stresses in the welded joints. Many investigations on the residual stresses in welds have been carried out. Feng et al. [28] analyzed the residual stress distribution in a GTA spot welded HSLA-100 steel using FEM and neutron diffraction technique. The computations included temperature-dependent thermophysical and mechanical properties of the base metal. The predictions from the FE models were in very good agreement with the neutron diffraction measurement results in the far heat-affected zone (HAZ) and in the base metal. Yanjing et al. [29] calculated the distribution of residual stresses in the weld of high strength steel by means of FEM. The instantaneous stress on the weld surface was about 900MPa. Ferro et al's analysis [26] showed that EBW is typically a high cooling and heating rate and a high thermal gradient welding technology.

2.3. Cracks Formation in HAZ

The response of materials in HAZ to thermal stresses caused by the welding thermal cycles is very important in determining the micro-structure and mechanical properties of welds. The melting, recrystallization, transformation, grain growth, dissolution of precipitates and segregation etc. may occur in HAZ. The change in microstructure in HAZ can result in a local decrease of strength and ductility, and cracks may form in HAZ, which leads further to degradation of the mechanical properties and performances of a welded component in service.

2.3.1. Fracture of Metal Structure

The failure of structural components is of critical importance. There have been many serious accidents due to structural failures for over 100 years. In most structural failures, the final fracture is usually abrupt after some sort of material or design flaw, such as material defects, is aggravated by a crack growth process, which causes a crack to reach a critical size for final fracture. Therefore, cracks play key roles in the fracture of structures in service. Actually, the cracking process is a crack initiating and propagating process. There are various crack nucleation and growth mechanisms related to the service conditions of a structure, for instance applied load modes and environments.

2.3.1.1. Fracture Mechanism

Generally, final fracture mechanisms are termed 'ductile' and 'brittle'. Sometimes, brittle fracture is referred to as a cleavage fracture, and dimple rupture is considered as a ductile fracture. Compared to ductile fracture, brittle fractures are much more dangerous because they almost invariably initiate at defects and discontinuities, and often result in catastrophic failure [30].

From fracture mechanics, crack-growth-criterion for brittle fracture is,

$$K_c = \sqrt{EG_c} = \sigma \sqrt{\pi a} \quad (2-13)$$

Where, K_c is the critical value of the stress intensity factor, G_c is the critical strain energy release rate, σ is the applied stress on a crack, a is the crack length.

From equation (2-13), it is known that if σ is constant, the fracture can occur when a crack length reaches a critical value a_c , or vice versa. Then, the fracture is a complete separation of a material that occurs when a crack reaches a critical size and impairs the strength to a load below the service load. The external applied loads (stress) can be divided into monotonic and cyclic or fatigue load. Thus, there are monotonic fracture and fatigue fracture with respect to the service loads.

2.3.1.1.1. Microvoid Coalescence

Microvoid coalescence is the only 'low-temperature' ductile micromechanism of a monotonic fracture, which is often referred to as dimple rupture. Sometimes, the dimple fracture surfaces can be observed when voids form at grain boundaries during high-temperature deformation. The fracture processes include void initiation, void growth, and finally coalescence.

- Void initiation [31]

Void initiation happens by particles-matrix decohesion or particle cracking. Usually, the interfacial segregation of detrimental trace elements enhances the particle-matrix decohesion. Also, particle size and location in the matrix dominate the void nucleation. The void initiation is also affected by the stress state. The critical strain or stress corresponds to the void nucleation.

- Void growth

Void growth depends on the microstructure of the matrix. It can occur by plastic deformation of the matrix or by linkup of smaller voids surrounding a

large initial void. Of course, any microstructural feature, which blocks or interferes with void growth, will enhance the fracture resistance.

- Void coalescence

This can occur by several mechanisms. The two important mechanisms are the tensile void coalescence and the shear coalescence [32]. Many experimental observations showed that the tensile coalescence mode brings about a flat dimpled fracture morphology in a variety of ductile materials under a wide range of stress states. Shear coalescence is favored by low stress triaxiality, low strain biaxiality and low strain hardening because shear rupture is thought to absorb less energy. Void coalescence occurs by the linkage of smaller voids formed at smaller particles along shear bands between larger voids. This mode of coalescence is similar to shear banding at the scale of the voids.

2.3.1.1.2. Cleavage

Cleavage fracture is a brittle fracture. It occurs primarily by separation of atomic bonds on a low-index atomic plane. Fracture surface possesses crystallographic characteristic because fracture happens along well-defined crystallographic planes within each grain. Ideal cleavage fracture occurs in materials that exhibit little or no capacity for plastic deformation as well as materials in which the plastic deformation zone in front of a crack tip is very small.

2.3.1.1.3. Intergranular Fracture

It occurs by crack propagation along grain boundaries of the matrix. Intergranular fracture is always associated with low toughness and low ductility, and is therefore an undesirable fracture mode. The causes for the intergranular fracture are:

- (1) Intrinsic weakness of the grain boundaries,
- (2) Precipitation of a brittle phase or segregation of detrimental elements on grain boundaries,
- (3) Embitterment of grain boundaries by hydrogen or other aggressive environments,
- (4) Intergranular corrosion,
- (5) Intergranular melting.

2.3.1.2. Fatigue Failure

A fatigue failure is one in which a metal fractures because it is subjected to a high number of cycles at a stress below the metal's yield strength. Fatigue occurs because microcracks develop in the metals when it is cyclically stressed. In commercial metals and alloys, fatigue crack initiation occurs at any feature that concentrates the local stresses and plastic strains. Some of these features are voids, inclusions, twin boundaries, grain boundaries, stronger second phases, and discontinuous sites. Fatigue cracks prefer to form at the welds because at these locations a mechanical property discontinuity exists, especially at the microcracks in HAZ.

2.3.1.3. High-temperature Mechanical Properties of Metals

The high-temperature mechanical and physical properties, specifically strength, fracture toughness, cyclic fatigue-crack growth and creep behavior, of a metal are much different from the corresponding values at ambient temperature. Generally, the mechanical strength decreases with an increase in temperature. However, in Ni-base superalloys, the ductility of the base metal and weld metal drop considerably in the liquidus and solidus temperature range. As the temperature decreases further from solidus temperature, the ductility decreases again in a temperature range. The former temperature range is termed 'solidification brittleness temperature range (BTR)' and the latter is termed 'ductility dip temperature range (DTR)'. Fig.2-3 illustrates the change in ductility with increase of temperature [20].

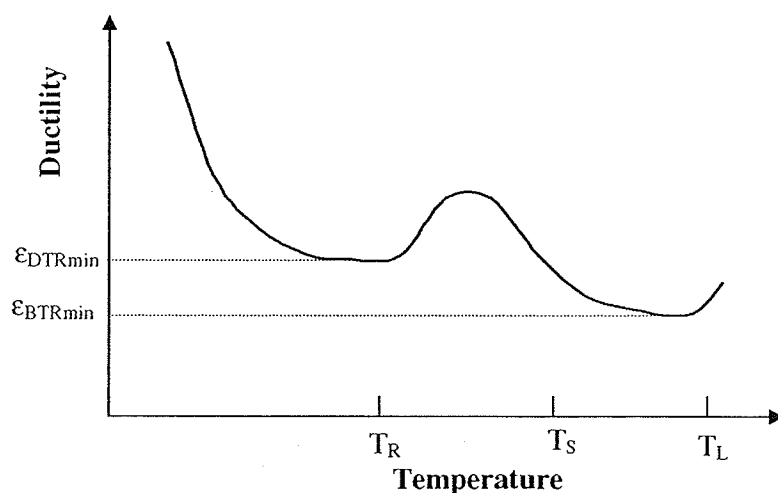


Fig.2-3 Schematic diagram of ductility change with temperature [33]

2.3.2. Stress Concentration

From fracture mechanics, especially, micro fracture-mechanics, the flaws such as microcracks cause the stress surrounding the flaws to be amplified where the magnification is dependent upon the orientation and geometry of the flaw. For example, the stress in front of elliptically shaped crack is much larger than the nominal applied stress, and the corresponding values decrease with increasing distance away from the crack tip. The stress raisers may be cracks, second phase particles and grain boundaries. Actually, the cracking process depends on the stress concentration.

2.3.2.1. Microcrack

The stress concentration in front of a crack can be expressed as:

$$\sigma_m = \sigma_a 2 \sqrt{\frac{a}{r}} \quad (2-14)$$

where σ_a is the nominal applied tensile stress; r is the radius of curvature of the crack tip; and a represents the half length of an internal crack. Generally, the crack length is much larger than the radius of curvature of the crack tip. i.e. $a \gg r$.

2.3.2.2. Inclusions

Based on the theory of elasticity and dislocation models, Argon and Safoglu analyzed the interfacial stresses (σ_{IT}) around the second phase [34]. They concluded that it is given by:

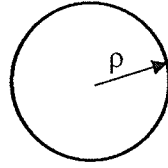


Fig.2-4 Cylindrical particle

$$\sigma_{rr} = \tau \left[4 \left(\frac{\rho}{r} \right)^2 - 3 \left(\frac{\rho}{r} \right)^4 + 1 \right] \cos 2\theta \quad (2-15)$$

Where, τ is the boundary shear traction and ρ the radius of the cylinder (see Fig.2-4). For very small spherical inclusions ($\rho < 10\text{nm}$), the interfacial tensile stress at $x = \lambda/2$ ($\lambda = \rho(\sqrt{2\pi/3f} - \sqrt{8/3})$, (f is the volume fraction of inclusions)) is given by:

$$\sigma_{rr} = \tau_0 \left(1 + \sqrt{\frac{6\sqrt{6}}{m} \frac{\gamma}{\gamma_y}} \right) \quad (2-16)$$

Where, τ_0 is the yield shear stress, m is Taylor factor, γ is shear strain and γ_y is the yield shear strain. For a large spherical inclusion ($\rho \gg 10\text{nm}$), the interfacial tensile stress at $x = \lambda/2$ is expressed as:

$$\sigma_{rr} = \tau_0 \left[\left(\frac{\gamma}{\gamma_y} \right)^{\frac{1}{n}} + \sqrt{3} \left(\frac{\sqrt{6}(n+1)}{m} \frac{\gamma}{\gamma_y} \right)^{\frac{1}{n+1}} \right] \quad (2-17)$$

Where, n is the hardening exponent ($= 2 \sim 8$). Using numerical and experimental methods, Hancock and Thomson [35] analyzed further the stress and strain concentrations in ductile fracture, and an expression of stress concentration was given:

$$\sigma_{rr \max} = C \bar{\sigma}_{\infty} + \sigma_{m\infty} \quad (2-18)$$

Where, $\bar{\sigma}_{\infty}$ is effective remote stress, $\sigma_{m\infty}$ is mean remote stress, and C is interfacial radial stress concentration factor. The value of C is in the range from 1.6 to 2.4 if the stress-strain law is taken as a power form. Actually, the stress and strain concentrations due to inclusions (or second phase particles) result in the formation of voids and crack growth.

2.3.2.3. Grain Boundaries

Grain boundaries play a very important part in the deformation and failure of metals. In accordance with the Hall-Petch relationship, grain boundaries play a key role in the strengthening of metals. Benson et al. [36] summarized the effects of grain size on yield strength of metals. The following four principal factors contribute to grain-boundary strengthening.

- (a) The grain boundaries act as barriers to plastic deformation.
- (b) The grain boundaries act as dislocation sources.
- (c) Elastic anisotropy causes additional stresses in the material surrounding a grain boundary.
- (d) Multislip is activated in the grain-boundary regions, whereas grain interiors are initially dominated by single slip, if properly oriented. As a result, the regions adjoining grain boundaries harden at a rate much higher than the grain interiors.

On the other hand, inclusions, such as carbides, nitrides and oxides prefer locating on the grain boundaries in wrought metals, and detrimental trace elements tend to segregate at the grain boundaries. The combination of these factors makes the role of grain boundaries in the failure of materials very complex. There are many research papers

devoted to this issue. The characteristics of grain boundary determine also the weldability of metals and alloys [37]. In a few of the following sections, detailed discussions on the effect of grain boundaries will be presented.

2.3.3. Strengthening of Superalloys

The strength of a material depends on its microstructure, the in-service conditions and environments. Superalloy is a special kind of alloys, which was developed to improve heat resistance properties of materials so that they could be used at the conditions of high temperatures and in a severe corrosive environment with high complex stresses. In order to improve the high temperature strength of these alloys, strengthening by solid solution strengthening, carbide-precipitation strengthening and γ/γ' phase-precipitation strengthening are employed [33]. At times as many as twelve alloying elements are added to superalloys to improve properties. Some of them dissolve into the parent phase (γ) and strengthen the base metal, some of them prefer to form second phase particles and induce precipitation hardening effects. The second phase particles are roughly divided into carbides and intermetallic compounds. The distribution, the quantity and the geometry of these phases depend on the processing history of the superalloys. Regarding carbides, five main types of carbides are found in superalloys, M_3C_2 , M_7C_3 , $M_{23}C_6$, M_6C and MC . Seven kinds of intermetallic compounds are γ' , γ'' , η , δ , Laves and μ [33].

The functions of minor elements in superalloys are different in different superalloys and the microstructure of the base metal. In nickel-based superalloys strengthened by the

presence of a large volume fraction of coherent $\text{Ni}_3(\text{Ti, Al})$ precipitates (γ), the creep rupture properties can be improved by small additions of for example, B, Zr, and P, because the segregation of B and P increases grain boundary cohesion, thereby increasing the creep properties [38]. But, addition of B and P in nickel base superalloys decreases the weldability of Ni-based superalloys [39, 40].

2.3.4. Solidification Cracking of Weld

Welding and joining processes are essential for the development of virtually every manufactured product. Tungsten-inert gas (TIG) welding and electron-beam welding are main fusion welding processes that are widely employed in joining superalloy components because these are unlikely to cause oxidation of the weld. The parent phase of Ni-base superalloys is a FCC- γ phase; and fusion during welding can cause hot cracking, for example, solidification cracking. Solidification cracking occurs in a weld during cooling of the fusion zone. The crack originates at the solute segregation within the residual molten metal, i.e. between the growing columnar microstructures. At the terminal stage of solidification, the concentration of tensile stress/strain, which is generated by the restrained contraction of molten material during solidification, acts upon the low melting point liquid formed by the columnar microstructures which results in cracking.

Many factors can affect the solidification cracking [33, 41]. The susceptibility of weld metal to solidification cracking seems to depend on the following three factors:

- The coarseness of the primary solidification microstructures (or dendrites).
- The amount/distribution and species of micro-segregation.

- The degree of restraint of the joint.

Nickel base superalloys such as Inconel 718 and Incoloy 903 are Nb bearing superalloys, and are widely used in aircraft industry. Nb is an element, which forms easily NbC, γ' phase and Laves phase. From the phase diagram [42, 43], it is known that eutectics of γ /NbC and γ /Laves are prone to solidify at a lower melting point, and make the weld fusion zone susceptible to solidification cracking.

2.3.5. HAZ Cracking of Welds

Heat-affected zone cracking occurs due to liquation of precipitates on grain boundaries or by the segregation of detrimental elements on grain boundaries. Heat-affected zone cracking has been also called liquation cracking, microfissuring, and hot cracking [41]. It has been an important subject of study of the weldability of metals since 1960's. Various factors affect the HAZ cracking. For instance, the thermal-mechanical properties of the welded metal depend on its chemical composition and the microstructure (such as, phases of matrix, grain size and structure), and the welding method as well as welding conditions. The combination of these factors makes the HAZ cracking a complex process.

Superalloys are important industrial material, but they are difficult to weld because they are susceptible to HAZ cracking and solidification cracking, especially, the alloys strengthened by γ' precipitation. Therefore, extensive investigations of HAZ cracking susceptibility of different superalloys have been carried out in the past decades.

Nb bearing nickel base superalloys use Nb as its strengthening element; these alloys include Inconel 718 and Incoloy 903. However, the addition of Nb results in HAZ

liquation cracking and degradation of ductility at elevated temperature. Regarding liquation cracking in Nb bearing superalloys, the research attention has been focused on below factors:

- Liquation of carbides and Laves phase particles within grain boundaries in HAZ [44-47].
- Effect of pre-weld heat treatment microstructure of base metal on liquation cracking [2, 3, 48].
- Effect of segregation of minor elements (C, S, B, P) on grain boundaries on HAZ cracking [5-12, 39, 45, 49-51].
- Formation of low melting point interfaces or liquid films within grain boundaries [52-55].

Thompson et al. [44, 47] studied the relationship between microstructure and HAZ cracking of Inconel 718, and found that the constitutional liquation of NbC particles on grain boundaries resulted in a decreased ductility of the alloy, which depended on the pre-weld heat treatment. Vincent [46] analyzed symmetrically the precipitation such as carbides and Laves phase associated with hot cracking and grain boundaries in HAZ of electron beam welds of Inconel 718 by means of analytical SEM and TEM. The pre-weld heat treatment of the base metal of Inconel 718 determines its microstructure and the chemical distribution of alloying elements. The HAZ cracking susceptibility depended on the chemical composition around the grain boundaries. The microfissuring susceptibility of Inconel 718 also increased with grain size [2, 3]. Chaturvedi and Richards [48] investigated the characteristics of microstructures and HAZ cracking of electron beam welds of Incoloy 903 through optical microscope, SEM and TEM with EDX. They found

that microfissuring preferred to originate and propagate along the warm worked long grain boundaries, where the carbides are located, and the microfissuring was accompanied with constitutional liquation of carbides and phosphides, however, no cracks on boundaries of fine grained material were observed. The appearance of liquid film migration (LFM) was observed, and LFM was suggested to prevent HAZ cracking. The segregation of trace elements within grain boundaries substantially affected HAZ cracking. Thompson et al.[49] examined effect of carbon on intergranular liquation cracking in the weld heat-affected zone of cast alloy 718. The experimental results showed that the volume fraction of carbides depended on carbon content in cast 718 alloy, but there was no direct relation between the amount of liquation phases, NbC and Laves, and the susceptibility to HAZ cracking. Chaturvedi and his research group [2-12,50,51] studied systematically the effects of minor elements, for instance, boron, phosphorous, sulfur and carbon, on heat affected zone microfissuring in welds of nickel base superalloys. It was indicated that segregation of boron at grain boundaries promoted the liquation cracking of welds, and the alloys with higher boron content were much more susceptible to HAZ cracking [5]. The boron concentration at grain boundaries in Inconel 718 occurred by both equilibrium segregation during solution heat treatment and by non-equilibrium segregation during cooling. Huang [50] et al. observed by secondary ion mass spectroscopy that boron segregated at grain boundaries during the pre-weld solution heat treatment of cast alloy 718, which substantially decreased the weldability of the cast alloy 718. It was concluded that the HAZ cracking was due to the pre-weld solution heat treatment and cooling mode (i.e. cooling rate). Boron concentration at grain boundaries resulted in lowering melting temperature of the grain boundaries. They also

found that in wrought Inconel 718 the character of grain boundaries also affected the boron segregation. Observations verified that boron atoms preferred to segregate at random grain boundaries rather than at coincident site lattice (CSL) grain boundaries [7, 11, 50, and 51].

Regarding the effect of sulfur on HAZ cracking susceptibility of superalloy weld, Thompson [3] concluded that sulfur content increased microfissuring. Guo et al. [9] reported that sulfur decreased the weldability of wrought Inconel alloy 718 through reducing the solidus temperature; however the effect of sulfur on microfissuring was significantly smaller than that of boron. Phosphorus, like boron also adversely affects HAZ liquation cracking. Richards and Chaturvedi [10] reviewed the effect of minor elements on liquation cracking of weld in nickel base superalloys. They concluded that all of minor elements B, C, S and P are detrimental to HAZ cracking susceptibility; the B is the most detrimental element of them. Since the pre-weld heat treatment determines the solute segregation at grain boundaries, the HAZ cracking is sensitive to the heating history and the cooling rate from high temperature during the pre-weld heat treatment.

Ernst et al. [52] examined the weldability of Incolloys 903, 907 and 909 using Varestraint test. Their observation demonstrated that liquation microfissuring originated at the interfaces with low melting point, such as Laves/ γ , Nb rich carbides/ γ . The concentration of Nb and Si at grain boundaries promotes the grain boundary liquated.

The mechanisms for liquation microfissuring in HAZ of weld can be attributed to the following factors [53]:

- (1) Constitutional liquation.

- (2) Melting due to segregation of melting point suppressant elements on grain boundaries.
- (3) Mushy zone type intergranular melting.

The amount of micro constituent with low melting point such as Nb-rich Laves/ γ eutectic phase; the local chemical composition at grain boundary determine the liquid phase distribution. The combination of liquid film formed at grain boundaries and tensile stress generated by temperature gradient leads to HAZ cracking of the welds. Therefore, the features of grain boundary liquid film are important to understand intergranular cracking in HAZ. Radhakrishnan and Thompson [54] observed grain boundary liquid film migration in Gleeble cycled wrought alloy 718. Nakkalil et al. [55] reported their observations of grain boundary liquid film in actual electron beam welds of Incoloy 903. Chaturvedi and Richards's [56] investigation revealed that grain boundary liquid film migration (LFM) could prevent HAZ cracking in weld of Incoloy 903. However, Ojo et al. [57] found that the LFM effect was negated by the effect high volume fraction of constitutionally liquated γ phases in the weld HAZ of Inconel 738LC superalloy.

2.3.6. Segregation

From the view of microfracture mechanics of solids, the decreasing strength or failure of metals may be due to many metallurgical imperfections such as inclusions, microstructural segregation of elements, and residual stress etc. Segregation is an intrinsic features of alloys (especially alloys with high content of multiple alloying elements), and can have a dramatic effects on the properties of an alloy. Segregation

usually occurs during heating of alloys because it is mainly controlled by diffusion process. So, impurities in alloys, such as C, B, P, whose atom size is much smaller than the main elements, are prone to concentrate at the grain boundaries and phase interface, because the free energy of the interface is reduced by these atoms' concentration. In general, segregation can be divided into two types; one is equilibrium segregation, which usually occurs during the solution heat treatment of alloys, the other one is non-equilibrium segregation, which occurs during cooling. The equilibrium segregation is due to the diffusion of the smaller solute atoms to the interfaces (GB) where the atom density is less than in the grain interiors. However, the non-equilibrium segregation requires the formation of solute-vacancy complexes and its concentration gradient from grain interiors to the boundaries. He et al.'s [58] results revealed that strain could reduce segregation on original boundaries. McLean and Strang [59] investigated the segregation mechanisms of trace elements and its effects on mechanical properties of superalloys. They concluded that the segregation of trace elements at grain boundaries could lead to embrittlement of superalloys. As it is known, the fusion welding process involves thermal and mechanical action in HAZ, so that the effect of segregation occurring at grain boundary has been widely examined. Some typical investigations upon the segregation of minor elements have been reviewed in the previous section.

2.3.7. Eutectic Structure and Brittle Phases in HAZ of Welds

A eutectic is a mixture of two or more crystalline substances, which has a lower melting point than that of any of its constituents. Eutectic point is the point at which the

liquid phase borders directly on the solid composed of two or more phases, representing the minimum melting temperature of any possible alloys with multiple phases. A eutectic solid is strong but has little ductility because the interface between different crystalline substances can bear hardly any strain, for example, γ /Laves and γ /NbC eutectic structure in commercial superalloy 718. The eutectic formation, distribution and volume fraction of eutectic are dependent on chemical composition of the alloy and the solidification rate. From solidification theory, the content of solute in liquid in front of solidified crystalline increases with solidification time due to segregation. Once the composition reaches the eutectic value, the eutectic structure is formed, and the volume fraction (f_e) is determined by the initial composition (C_0) and the eutectic composition (C_e), which is given by [60]:

$$f_e = \left(\frac{C_e}{C_0} \right)^{\frac{1}{k-1}} \quad (2-19)$$

Where, k is the equilibrium distribution coefficient. If the C_0 and C_e are known, the value of k can be calculated. The volume fraction of eutectic solid will increase with a decrease in k .

In a fusion welding process, the metals in the fusion zone are melted. When the temperature is at or above solidus during heating, the metal starts to melt. The temperature on the fusion line is kept at solidus, and the grain (phase) boundaries in HAZ are partially melted due to the low melting point. Especially, the grain boundaries in HAZ can be liquated, in which the chemical composition is around eutectic composition (C_e) because of segregation. The liquation of the grain boundary leads to a reduction in the metal strength. Williams and Singer [61] developed an expression to evaluate the strength reduction when the temperature is above the solidus temperature:

$$\sigma = \left(\frac{8\mu\gamma}{\pi(1-\nu)A\sqrt{V}} \right)^{1/2} \quad (2-20)$$

where σ is the critical stress to propagate a crack, μ is the shear modulus, γ is the effective fracture surface energy, ν is Poisson ratio, A is a constant dependent on the grain size and dihedral angle, and V is the volume of liquid. Therefore, segregation occurring at grain boundaries can directly result in HAZ liquation cracking.

2.4. Inconel 718 and AllVac 718Plus Alloy

2.4.1. The Features and Application of Inconel 718 Alloy

Nickel base Inconel 718 alloy is the most widely used superalloy in the aerospace industry. It obtains its strength from precipitation hardening and maintains high strength up to 650 °C. Until 14 of June 2005, 3133 papers involving alloy 718 were cited in the metal indexes. This means that the investigation has already been carried out extensively. The understanding of the various features of Inconel 718 alloy is reasonably good.

Generally, the microstructure and the corresponding mechanical properties of base metals are dependent on heat treatment, manufacturing process and the thermal history. The Inconel 718 is currently used in cast, wrought and powder forms. The nominal chemical composition is listed in Table2-1. The normal phases found in the cast and wrought alloy Inconel 718 are the carbides (MC, M₆C), nitrides (TiN), γ , γ' , δ , α Cr, σ and Laves [62]. γ and γ' are the main strengthening phases in alloy 718, and their precipitation depends on the content of Nb and the heat treatment. δ phase precipitates around random grain boundaries, which is employed to control the grain size in wrought

metals and to increase the ductility. Additionally, the eutectic structure of γ/Nb and γ/Laves adversely affect the features of alloy 718 [42, 43, 63].

As is well known, superalloys are difficult to be welded because fusion-welding process makes metals experience thermal and mechanical stresses. However, the weldability of the alloy 718 is basically acceptable, since it appears to have reasonably good resistance to solidification cracking and HAZ microfissuring. Actually, the non-equilibrium solidification process and microstructure evolution affect the weldability of alloy 718. Vincent examined the precipitation around welds in alloy 718 [45] and found there were boride (M_3B_2), phosphide (MNP) and (Nb, Ti) carbosulphide, besides the common precipitates in HAZ of alloy 718 weld.

Table 2-1 Chemical compositions of Inconel 718 and Allvac 718Plus alloys (wt%)

Alloys	C	Cr	Mo	W	Co	Fe	Ni	Nb	Ti	Al	P	B
718	0.03	18.00	3.00	-	-	18.00	Bas	5.40	1.00	0.45	0.007	0.004
718Plus™	0.02	18.00	2.80	1.00	9.00	10.00	Bas	5.45	0.70	1.45	0.007	0.004

2.4.2. The Features of Allvac 718Plus Alloy

On the basis of alloy 718, Allvac Inc. developed Allvac 718Plus alloy recently to improve the relevant features of alloy 718. The modified chemical composition is listed in Table2-1. Cao and Kennedy [1] analyzed the elements' effects on the features (such as microstructure, mechanical properties and workability) of the new alloy. Compared with alloy 718, Co was added up to 9wt.%, Fe content was reduced from 18.0 wt.% to 10.0 wt.%, the contents of C, Ti, Al and Nb were slightly adjusted. The precipitation γ' phase on

the alloy strength was significantly increased, and γ'' has not been observed in the heat treatment alloy. The composition modification improved the rupture stress and thermal stability of the alloy. As a result, the service temperature is 55 °C higher than that of alloy 718's, and the mechanical properties and thermal stability is equal to or better than Waspaloy [1]. This new alloy appears to have extensive applications in aerospace. However, its weldability needs evaluating further before industrial application.

2.4.2.1. The Microstructure of Wrought Allvac 718Plus Alloy

According to the report of Allvac Company and Cao et al.'s paper [1], the matrix of Allvac 718Plus is γ phase. After standard heat treatment, the amount of γ'' , δ , η , Laves, and MC were observed in the alloy.

2.4.2.2. Phase Transformation Temperatures

The critical phase transformation temperatures of Allvac 718 Plus alloy are listed in Table2-2.

2.4.2.3. Solution Treatment

Standard heat treatment: 954 °C × 1hr. + 788 °C × 2hrs, furnace cooling at rate of 55 °C /h to 650 °C + 650 °C × 8hrs, air cooling.

2.4.2.4. Characteristics of Grain Boundaries

The grain size is ASTM7, the grain boundaries are mainly twin and random boundary. The carbides frequently distribute on grain boundaries

Table 2-2 Critical Phase Transformation Temperature of Allvac 718Plus Alloy

Phase Transformation	DTA				Thermal Calculation	
	Heating		Cooling			
	°F	°C	°F	°C	°F	°C
Liquidus	2457	1353	2458	1348	2455	1346
MC Eutectic	2358	1292	2280	1249	2300	1260
Solidus	2310	1265	-	-	2194	1201
Laves Eutectic	-	-	2126	1163	-	-
δ Solvus	-	-	-	-	1950	1065
γ' Solvus	1766	963	-	-	1823	995
γ'' Solvus	-		-	-	1774	968

Chapter 3

Experimental Procedure

3.1. Materials

The material used in this study was 718Plus alloy wrought plate with a thickness of 15.50mm, provided by Allvac Inc. The chemical composition is listed in Table3-1. The critical phase transformation temperatures of this alloy provided by Allvac Inc, are given in Table 3-2 [Company report]. Allvac Inc. developed this new alloy, which has a 55°C higher temperature capability than Inconel 718 alloy. In comparison with traditional Inconel 718 alloy, this alloy contains, twice the amount of boron and phosphorous, the ratio of aluminum to titanium was modified to improve the mechanical properties and thermal stabilities of the alloy. Actually, modifying the ratio of aluminium to titanium in Allvac 718Plus alloy changed the strengthening phase. The predominantly strengthening phase in Inconel 718 alloy is the coherent γ'

phase (Ni_3Nb), whereas the predominantly strengthening phase in Allvac 718Plus alloy is γ phase ($\text{Ni}_3(\text{Al,Ti})$).

Table 3-1 Chemical compositions of Allvac 718 Plus alloy (wt.%)

Alloy	C	Cr	Mo	W	Co	Fe	Ni	Nb	Ti	Al	P	B
718 Plus	0.025	18.00	2.80	1.0	9.0	10.00	Bas.	5.4	0.7	1.45	0.014	0.008
718	0.025	18.10	2.90	-	-	18.00	Bas.	5.4	1.0	0.45	0.007	0.004

Table 3-2 Critical Phase Transformation Temperature of Allvac 718Plus Alloy

Phase Transformation	DTA				Thermal Calculation	
	Heating		Cooling		°F	°C
	°F	°C	°F	°C		
Liquidus	2457	1353	2458	1348	2455	1346
MC Eutectic	2358	1292	2280	1249	2300	1260
Solidus	2310	1265	-	-	2194	1201
Laves Eutectic	-	-	2126	1163	-	-
δ Solvus	-	-	-	-	1950	1065
γ Solvus	1766	963	-	-	1823	995
γ' Solvus	-	-	-	-	1774	968

In this study, the specimens were solution heated at 950°C for 1 hour in argon gas, and then water quenched. To minimize oxidation of the plates during heating, they were wrapped in stainless steel sheets. Before welding, the oxidized surface was removed by milling. After the solution heat treatment, grain size of base metal was measured using an optical microscope with the image analysis system. The average grain size was measured to be 57 ± 4 (μm). Vickers hardness of the solution treated base metal, measured on pyramid hardness testing machine, was 277 ± 4 (Hv, load = 10kg).

3.2. Electron Beam Welding Conditions

The bead-on-plate electron beam welding was carried out by Bristol Aerospace Ltd. The accelerating voltage was kept constant at 44kV. 60 different welding conditions were designed to study the influence of electron beam welding parameters on the HAZ cracking of this new alloy. In general, the electron beam current (I) varied among 50.0, 67.5, 85.0, 102.0 and 120.0mA, the welding velocity (V) from 10.0, 22.5, 35.0, 47.5 and 60.0 in/min, the oscillation score factors along the cross (A_{my}) and the longitudinal (A_{mx}) directions changed individually in 0, 25, 50, 75 and 100, which are proportional to the electron beam oscillation amplitudes. The electron beam was sharply focused on the surface of samples during welding. The actual welding parameters used are listed in Table 3-3.

The four factor statistical design of the welding experiments was carried out by Professor Mount of the Department of Statistics at the University of Manitoba. The central composite design was based on 16 replicated (32) tests, 8 replicated (16) axial points and 12 centre points, for a total of 60 tests. Stepwise multiple regressions were used to evaluate the significant dependent variables against a cracking index.

3.3. Specimen Preparation

Each weld was cut into eight 2 mm thick cross sections on an electric discharge machine. These sections were mounted with Bakelite black powder at a pressure of

about 30MPa and a temperature of 110°C. The mounted samples were polished by the standard metallographic methods, and then were etched slightly by modified Kalling's reagent, which consisted of 40 ml-distilled water, 480 ml hydrochloric acid (HCl) and 48 g cupric chloride ($\text{CuCl}_2 \cdot 2\text{H}_2\text{O}$). Etched samples were examined using an optical microscope and an analytical SEM.

Thin foils for TEM observation were prepared by the following procedures: (1) cutting a rod with a 3mm diameter and then cutting the rod into discs with a thickness of 0.50mm; (2) grinding these discs on 600 grade SiC paper until the thickness was about 100 μm ; (3) The discs were electropolished to perforation using a dual jet eletropolisher (Struers Tenupol III). A polishing solution of 10% perchloric and 90% ethanol was used at -30°C with an applied DC voltage of 20 V and a current of approximately 50 mA. To prepare thin foils from the HAZ of a weld, the weld with the widest HAZ was selected, and the rod was cut at the neck of the nail-head weld.

Extraction replication is a powerful method for analysis of second phases in metals and alloys using TEM, because a particle can be extracted from its surrounding matrix and analyzed alone without interference from the electrons scattering into the matrix. The carbon replica was used to extract particles in the HAZ of a weld. The weld with the widest HAZ was selected to prepare a replica. The preparation procedures were as follows:

- (1) The polished sample was etched for 4 minutes in modified Kalling's reagent.
- (2) The fusion zone was covered with plastic tape.
- (3) The sample was put into the chamber with a high vacuum on a sputter coating machine.

- (4) The carbon electrodes were heated by the passage of current when the vacuum in the chamber reached 5.5×10^{-5} MB, causing carbon to evaporate and deposit as a film on the sample.
- (5) The carbon film on the HAZ was stripped by first scoring it into ~3mm squares in the HAZ with a sharp knife, then electro-polishing the sample at a voltage of 9V for 10 seconds.
- (6) The sample was cleaned carefully in methanol.
- (7) The sample was inserted into distilled water at a shallow angle to make use of the surface tension to peel and float the carbon film.
- (8) The small piece of film was then picked up out of the water on a 3mm specimen support grid.

3.4. Microscopic Examinations

Axiovert 25 optical microscope with an image analysis system was used to observe and measure the grain size of the base metal, crack lengths in the HAZ, and the HAZ areas of welds. A JEOL JSM-5900LV Scanning Electron Microscope (SEM) was used to examine the microstructures of the base metal and welds, in particular, particles and morphologies of cracks in the HAZ of welds. The microstructures such as second phases in the base metal and around the HAZ of welds were also observed by JEOL JEM-2000FX and JEM 2100F Transmission Electron Microscopes (TEM). Thin foils and carbon replicas were used for TEM observations. The SEM and the 2100F TEM were equipped with an ultra-thin window Oxford energy dispersive spectrometer (EDS), and the 2000FX TEM was equipped with an ultra-thin window Genesis energy dispersive spectrometer (EDS).

Table3-3 The EBW parameters

Std	Block	Run	V, in/min	I, mA	A _{my}	A _{mx}	Q*, J/mm
22	1	1	35.00	85.00	100.0	50.0	261.7
30	1	2	35.00	85.00	50.0	50.0	261.7
5	1	3	22.50	67.50	75.0	25.0	323.3
8	1	4	47.50	102.50	75.0	25.0	232.5
19	1	5	35.00	50.00	50.0	50.0	153.9
25	1	6	35.00	85.00	50.0	50.0	261.7
9	1	7	22.50	67.50	25.0	75.0	323.3
27	1	8	35.00	85.00	50.0	50.0	261.7
18	1	9	60.00	85.00	50.0	50.0	152.7
11	1	10	22.50	102.50	25.0	75.0	490.9
6	1	11	47.50	67.50	75.0	25.0	153.1
21	1	12	35.00	85.00	0.0	50.0	261.7
28	1	13	35.00	85.00	50.0	50.0	261.7
26	1	14	35.00	85.00	50.0	50.0	261.7
12	1	15	47.50	102.50	25.0	75.0	232.5
17	1	16	10.00	85.00	50.0	50.0	915.9
3	1	17	22.50	102.50	25.0	25.0	490.9
14	1	18	47.50	67.50	75.0	75.0	153.1
29	1	19	35.00	85.00	50.0	50.0	261.7
10	1	20	47.50	67.50	25.0	75.0	153.1
1	1	21	22.50	67.50	25.0	25.0	323.3
20	1	22	35.00	120.00	50.0	50.0	369.4
23	1	23	35.00	85.00	50.0	0.0	261.7
24	1	24	35.00	85.00	50.0	100.0	261.7
15	1	25	22.50	102.50	75.0	75.0	490.9
13	1	26	22.50	67.50	75.0	75.0	323.3
4	1	27	47.50	102.50	25.0	25.0	232.5
7	1	28	22.50	102.50	75.0	25.0	490.9
2	1	29	47.50	67.50	25.0	25.0	153.1
16	1	30	47.50	102.50	75.0	75.0	232.5

Table3-2 The EBW parameters. Cont.-

Std	Block	Run	V, in/min	I, mA	A _{mx}	A _{my}	Q*, J/mm
14	2	31	47.50	67.50	75.0	75.0	153.1
2	2	32	47.50	67.50	25.0	25.0	153.1
13	2	33	22.50	67.50	75.0	75.0	323.3
9	2	34	22.50	67.50	25.0	75.0	323.3
11	2	35	22.50	102.50	25.0	75.0	490.9
26	2	36	35.00	85.00	50.0	50.0	261.7
23	2	37	35.00	85.00	50.0	0.0	261.7
8	2	38	47.50	102.50	75.0	25.0	232.5
10	2	39	47.50	67.50	25.0	75.0	153.1
5	2	40	22.50	67.50	75.0	25.0	323.3
1	2	41	22.50	67.50	25.0	25.0	323.3
19	2	42	35.00	50.00	50.0	50.0	153.9
6	2	43	47.50	67.50	75.0	25.0	153.1
24	2	44	35.00	75.00	50.0	100.0	261.7
16	2	45	47.50	102.50	75.0	75.0	232.5
15	2	46	22.50	102.50	75.0	75.0	490.9
25	2	47	35.00	85.00	50.0	50.0	261.7
20	2	48	35.00	120.00	50.0	50.0	369.4
12	2	49	47.50	102.50	25.0	75.0	232.5
22	2	50	35.00	85.00	100.0	50.0	261.7
4	2	51	47.50	102.50	25.0	25.0	232.5
20	2	52	35.00	85.00	50.0	50.0	261.7
30	2	53	35.00	85.00	50.0	50.0	261.7
21	2	54	35.00	85.00	0.0	50.0	261.7
17	2	55	10.00	85.00	50.0	50.0	915.9
28	2	56	35.00	85.00	50.0	50.0	261.7
7	2	57	22.50	102.50	75.0	25.0	490.9
18	2	58	60.00	85.00	50.0	50.0	152.7
3	2	59	22.50	102.50	25.0	25.0	490.9
27	2	60	35.00	85.00	50.0	50.0	261.7

* Q= UI/V (U=44kV)

Chapter 4

Results and Discussion

4.1. Microstructure of the Base Metal

Microscopic examination demonstrated that the microstructure of the solution heat-treatment specimen consisted of γ phase, precipitates, grain boundaries, and several second phases such as carbides. Fig.4-1 is a low magnification SEM micrograph of the base metal, showing many twin and random boundaries in it. A high magnification SEM micrograph (see Fig.4-2a) shows the presence of small acicular precipitate plates mostly at or close to grain boundaries. The TEM micrograph and EDS analysis (as seen in Fig.4-2b and c) suggests that the small acicular precipitate plates on grain boundaries are delta phase. On the basis of analysis of diffraction pattern from the precipitate plates shown in the insert of Fig.4-2b), it was confirmed that these precipitates are delta phase

with lattice parameters $a = 0.514\text{nm}$, $b = 0.425\text{nm}$ and $c = 0.453\text{ nm}$. Fig.4-2c reveals that delta phase is rich in Nb with a concentration of about 26 at.%. The presence of delta phase on grain boundaries prevents grain growth at elevated temperatures. Another important precipitates in the base metal were small γ' phase particles with a diameter of 1-2 nm as seen in Fig.4-3 which is the TEM dark field image of γ' phase, taken with (110) super lattice reflection. This TEM micrograph shows that the small γ' phase particles were distributed homogenously in the matrix.

Typical carbides/borides were observed by SEM analysis within grains (see Fig 4-4a) and on grain boundaries (see Fig.4-4b). In particular, carbides/borides on grain boundaries can greatly affect liquation cracking in HAZ.

4.2. HAZ Cracking

HAZ cracking usually occurs during welding of superalloys. Extensive investigations suggest that the HAZ cracking is a very complex process because it involves high temperature and thermal stress/strain during welding. From a schematic diagram shown in Fig.4-5, it can be seen that many factors affect the HAZ cracking. From the fracture mechanics point of view, cracking occurs if the exerted stress/strain (σ) is greater than a critical value (σ_c). The critical value is dependent on characteristics of the base metal such as composition, microstructure, and the temperature. The local compositions, microstructure and temperature in the HAZ of a weld vary significantly due to varying temperature. At the same time, the stress/strain is generated due to the establishment of a temperature gradient in the HAZ. The temperature gradient and the

change in thermal/mechanical properties of the base metal determine the stress/strain in the HAZ. During welding, the temperature and its gradients can be controlled by varying the welding parameters. The interaction among these factors makes the HAZ cracking extremely complex.

4.3. Microstructural Characteristics of HAZ Cracking

Researchers have been attempting to understand the HAZ cracking process on the basis of microstructural examination in the HAZ, since it is difficult to do an in-situ observation of the HAZ cracking.

Fig.4-6 shows a typical nail-head shape of an EB weld and the geometrical parameters, W_p , W_m and W_s are the top, the middle and the neck width, respectively, of the nail-head shape, D is the penetration depth of welds. Generally, all the welds were narrow and deep. By an optical examination at magnification of 500, cracks were observed in the HAZ. Approximately ten thousand cracks in the HAZ within 480 cross sections were examined and their lengths were measured by means of a optical microscope equipped with an image analysis system. Many typical cracks were further examined and analyzed in detail using SEM. All cracks were intergranular and perpendicular to the fusion line, i.e. paralleling to the heat conduction direction. Cracks often formed along random grain boundaries rather than twin boundaries. Most of the cracks and the longest crack were located at in the neck region of the nail-head welds, as shown in Fig.4-7. Few cracks were also observed to extend into the fusion zone. In general, two kinds of cracks were observed. The first was accompanied with re-solidified

products that were rich in Nb, according to the EDS analysis, as shown in Fig.4-8. The second type of cracks were without any re-solidified products in them, see Fig.4-9.

4.3.1. Grain Boundary Liquation

A large volume of re-solidified products accompanied the cracks along random grain boundaries in the HAZ. The morphology of re-solidified products was the same as that of the liquated Laves/ γ eutectic structure observed in Inconel 718 alloy [43, 64]. However, the resolidified products without cracks were also observed at grain boundaries in the HAZ, as shown in Fig.4-10. The EDS analysis indicated that the re-solidified product was rich in Nb, the other elements were almost the same as those present in the matrix. The morphology and the composition of the re-solidified products suggest it to be Laves phase or carbides rich in Nb. On the basis of the work principle of the EDS equipped on the SEM, the composition obtained by EDS quantitative analysis is an average of the local volume in the matrix excited by the electrons, which is generally scattered micron deep and in diameter, depending upon operation parameters of the SEM. Therefore, the composition of a small particle obtained by the EDS analysis on the SEM could also include contents of the matrix. In order to eliminate the interference of the matrix, and to further identify the phase structure of the re-solidified products, carbon replication method was employed. Re-solidified products were extracted on carbon replicas, and were analyzed using TEM. Fig. 4-11 shows the morphology of re-solidified products extracted on a carbon replica and the analysis results obtained using TEM. Fig.4-11a shows parts of re-solidified product present on a GB. Fig.4-11b and Fig.4-11c

indicate the diffraction patterns from two different zone axes. These diffraction patterns needed indexing to identify a crystal structure of the re-solidified product. First, the distances of diffraction spots from the center incident spot (R_i) were measured on the negatives. Second, the corresponding inter-atomic planer distances (d_i) were calculated from the following equation

$$R_i d_i = L \lambda \quad (4-1)$$

Where L is camera length, λ is the electron beam wavelength. Vincent [45] reported the lattice parameters of Laves phase (hcp structure) in Inconel 718 alloy, i.e. $a = 0.474\text{nm}$, $c = 0.772\text{nm}$. Using equation (4-2), the inter-planer distance of a plane of indexes h , k , l can be calculated:

$$\frac{1}{d_s^2} = \frac{4}{3} \frac{h^2 + hk + k^2}{a^2} + \frac{l^2}{c^2} \quad (4-2)$$

Table 4-1 Measured and calculated distance of (h k l) plane of Laves phase

Negative	R (mm)	d (nm)	h	k	l	d_s (nm)
b	5.95	0.383	1	0	1	0.363
	10.15	0.225	-1	1	3	0.218
	10.9	0.209	-2	1	2	0.202
c	10.3	0.221	-1	1	3	0.218
	10.8	0.211	-1	-1	-2	0.202
	11.2	0.204	-2	0	1	0.198

From Table 4-1, it is seen that the measured inter-planer plane distances of Laves phase is in agreement with the calculated values. This means that the re-solidified product shown in Fig.4-11a is Laves phase. The two diffraction patterns shown in Fig.4-11b and c are of Laves phase with zone axes of $[\bar{1}\bar{4}1]$ and $[\bar{5}12]$ respectively. The EDS quantitative

analysis (Fig.4-11d) indicated the Laves phase to contain 36.6wt% Nb. However, since there was no Laves phase in the base metal, this Laves phase on the grain boundary might have resulted from the liquation of a Nb containing particles on the grain boundary during the welding process.

Another re-solidified product was also observed on a carbon replica using TEM, which is shown in Fig.4-12. The analysis of the diffraction patterns and EDS composition demonstrated that it was MC type of carbide. The morphology of carbides or borides in the solution-treated base metal was round/square shape particles, and sheet shape MC carbide and borides were not observed in the pre-weld metal. Therefore, the MC carbide sheet shown in Fig.4-12 could have resulted from the liquation of (NbC) precipitates present on the grain boundaries.

4.3.2. Delta Phase Dissolution

Delta phase is another important precipitate in 718 type superalloys. Delta phase usually exists on random grain boundaries in the base metal after solution heat treatment of Allvac 718Plus alloy (see Fig.4-2), which plays a role in limiting grain growth during solution treatment. Although the delta phase is thermodynamically more stable than the γ' phase, the solvus of the delta phase is only 1065°C in this new alloy. During welding thermal cycle, the temperature in fusion zone is certainly above the melting point-liquidus (1353°C), and there is a relative wide region in the HAZ close to the FZ where the temperature is surely over the solvus of the delta phase, which may cause dissolution of the delta phase in the HAZ. In the present study, the SEM observations of

microstructure in the HAZ of welds suggested that δ phase dissolution indeed occurred in the regions close to the fusion line in the HAZ, as shown in Fig.4-13, the δ -phase around grain boundaries close to the fusion line could not be detected using SEM, but it was still observed in regions far from the fusion line.

The microstructure of HAZ was also examined by TEM. Fig.4-14 reveals the microstructure near a triple grain boundary, and the relative angle of rotation between these two TEM micrographs is 15° (Fig.4-14a and Fig.4-14b). These micrographs clearly show that there are no δ phase plates on grain boundaries in the HAZ close to the FZ. Thus, the TEM observations further verified that the δ phase around GB in the HAZ was dissolved during welding.

4.3.3. Mechanism of Grain Boundary Liquation Cracking

On the basis of the microstructural observations in the HAZ, one HAZ cracking mechanism can be suggested. The delta phase has a composition of Ni_3Nb and an orthorhombic crystal structure [45]. It normally precipitates via nucleation at grain boundaries followed by the growth of thin plates extending into the grains, see Fig.4-2. The delta phase around grain boundaries was first dissolved during the welding thermal cycle. The dissolution of δ phase resulted in the Nb atoms concentration on the local grain boundaries to increase because it consists of about 36.6wt% Nb (see Fig.4-2c). The compositions at the local grain boundary deviated far from the average compositions of the alloy, which led to a decrease in grain boundary melting point. From the solidification phase diagram for Inconel 718 alloy given by Knorovsky et al.[43] and shown in Fig. 4-

15, an increase in the Nb content locally shifted composition of the alloy from a single phase (γ phase with 5.4 wt%) to a two phases (γ +L) region (the temperature is in the range from the liquidus-1353°C to eutectic temperature- T_E). Consequently, the melting point of the local GB materials decreased linearly with an increase in the Nb content. Once the concentration of Nb element approached to that of eutectic point of γ /Laves (Nb content is 19.1wt% for Inconel 718 alloy), the melting temperature was at the lowest point of T_E . Although the solidification phase diagram for Allvac718Plus alloy has not been completely established, the basic effect of Nb element on the liquidus of Allvac718Plus alloy should be the same as in Inconel 718 alloy. As listed in Table 3-2, the eutectic temperature of Allvac718Plus alloy is only 1163°C. Moreover, there would be a relative wide region in the HAZ where the temperature would be sufficiently higher than 1163°C. The grain boundaries, therefore would melt, i.e. the grain boundary liquation would occur. Thus, it is suggested that the observed Laves phase on grain boundaries in the HAZ might be the result of grain boundary liquation, which can also interpreted as rapidly frozen liquid phase.

The liquated grain boundaries caused the strength of the alloy to decrease [61]. When the tensile stress/strain generated from temperature gradient during welding was above the reduced critical value, the visible crack formed along the liquated grain boundary. As a result, the cracks with re-solidified products were observed in the HAZ, see Figs.4-8.

On the other hand, the constitutional liquation of MC in wrought Inconel 718 alloy has been recognized as one of the important causes of intergranular liquation cracking in the welding process of superalloys. Radhakrishnan and Thompson [64] used γ -NbC-

Laves pseudo-ternary to explain the liquation cracking in alloy 718. For Allvac 718Plus alloy, although the liquidus is 1353°C, the melting temperature on some random grain boundaries could be substantially less than 1353°C due to the acute segregation of alloying elements on them. For instance, there existed a γ -NbC eutectic microstructure around the NbC particles on grain boundaries. The eutectic temperature of γ -NbC is only 1249°C, thus, the grain boundaries with NbC particles would be liquated during the welding thermal cycle, as the temperature reached above the eutectic temperature of γ -NbC eutectic. The liquated grain boundaries re-solidified during cooling after welding; the NbC sheets, therefore, may have formed at some grain boundaries.

Generally speaking, the strength of the alloy is reduced with the grain boundary liquation. The liquated grain boundaries cannot bear the tensile stress/strain, and has a great potential to crack. However, many factors affect the crack formation on grain boundaries. Regarding the grain boundary liquation cracking, the local stress/strain state and the amount of liquated GB are the major factors affecting it. Williams and Singer [61] have suggested an expression to evaluate the critical stress (σ_c) when the temperature is above the solidus temperature:

$$\sigma_c = \left(\frac{8\mu\eta}{\pi(1-\nu)A\sqrt{V}} \right)^{1/2} \quad (4-3)$$

where, μ is the shear modulus, η is the effective fracture surface energy, ν is Poisson ratio, A is a constant depended on the grain size and dihedral angle, and V is the volume of liquid. From equation (4-3), it can be seen that the strength reduction is small if the volume of the liquated grain boundaries is not sufficiently large. The problem can be explained on the basis of fracture mechanics. The cracking process consists of crack

formation and propagation. A microcrack can form at a hard particle, a deformed grain boundary, and at the intersection of two slip bands. If the critical condition for propagation is not satisfied, cracking cannot occur. Similarly, the HAZ cracking would not occur either if only a small amount of grain boundary was liquated. Thus, the thin sheets of re-solidified products without any crack were observed along grain boundaries in the HAZ, see Fig.4-10.

4.3.4. Effect of Trace Elements on HAZ Cracking

The segregation of trace elements (B, P, S, and C) on grain boundaries significantly affects the HAZ cracking, which has been extensively investigated [5-11, 49]. The detrimental effect of individual elements on HAZ cracking was reviewed in Chapter 2. The total concentration of B and P in the Allvac 718Plus alloy is twice as large as that of Inconel 718 alloy. Naturally, the effects of B and P on the HAZ grain boundary liquation cracking in Allvac718Plus alloy would be greater than in Inconel 718 alloy. Chaturvedi et al. [5-12, 50, 51] studied systematically the effects of boron on the grain boundary liquation cracking in the HAZ of welds in nickel base superalloys. Their observations indicate that boron atoms preferred to segregate at random grain boundaries rather than at coincident site lattice (CSL) grain boundaries [7,11,50,51], and the segregation of boron at grain boundaries promoted liquidation cracking in HAZ because of the segregation of boron lowers the grain boundary melting temperature. The segregation of phosphorous also promoted HAZ cracking susceptibility of superalloys. The segregation of boron and phosphorous atoms to grain boundaries could take place during the pre-weld heat treatment via equilibrium and non-equilibrium processes. The segregation of other

impurities could also take place during welding [65, 66], the non-equilibrium segregation of B made a major contribution, since the heating and cooling rates were rapid, Once the temperature in the HAZ increased above the local grain boundary melting temperature, the grain boundary liquation occurred. Huang et al. [50], Chen et al. [6] and Benhadad et al. [12] used Secondary Ion Mass Spectrometry (SIMS) analysis to detect the segregation of boron on the grain boundaries. In the current study, the particles rich in boron and niobium were observed along the edges of cracks in the HAZ, an example which is shown in Fig.4-16. On the basis of this observation, it is possible to deduce that there are more boron atoms on the grain boundaries, which make them cracking susceptible.

The effect of phosphorus on HAZ cracking susceptibility of superalloy weld has also been investigated. Phosphorous like sulfur affects on HAZ liquation cracking, in a manner similar to boron. Richards and Chaturvedi [10] reviewed the effects of minor elements on liquation cracking of welds in nickel base superalloys. It was concluded that all of minor elements B, S and P are detrimental due to increasing the HAZ cracking susceptibility; B being the most detrimental element of them. The segregation of these elements on boundaries causes not only a lowering of the grain boundary melting temperature, but also reduces the ductility of the alloy when temperature is close to liquidus/solidus. Brittle cracking would occur along these kinds of grain boundaries. The observed cracks without resolidified products (see Fig.4-7) might form due to the concentration of detrimental elements on grain boundaries. Regarding this subject, more work needs to be done in the future.

4.3.5. Effect of Particles on Grain Boundaries on HAZ

Cracking

According to fracture mechanics, cracking occurs if an exerted stress/strain is above the critical value of stress/strain for cracking. Considering the HAZ cracking during welding, investigators have been attempting to know the change of stress/strain caused by microstructural change with elevated temperatures during welding. For example, as mentioned above, the HAZ cracking occurs along liquidated grain boundaries, as the liquidated grain boundary greatly decrease the local grain boundary strength. On the other hand, some factors may enhance the exerted stress/strain on the weakened grain boundary, and cracking could occur. In the present study electron beam welding was used which is a fusion process. The thermal cycle produced by the moving electron beam lead to steep temperature gradient in the HAZ of welds and a transient thermal stress/strain is generated in the HAZ. In the micro-fracture mechanics view, the stress/strain is not homogenous in the HAZ because there are different flaws such as second phases (particles), grains, grain boundaries in the HAZ. These flaws can magnify the stress in front of them. Cracks connecting two particles along grain boundaries in HAZ of welds were observed in the present study, an example of which is shown in Fig.4-17. The EDS analysis shows that one of the particles is rich in Nb and the other rich in Ti. Both of them have sharp corners and are located within a grain boundary. The stress concentration in front of these two particles could promote grain boundary cracking. Moreover, elastic anisotropy is able to cause additional stresses in grain-boundary surroundings. Inclusions, such as carbides, nitrides and oxides prefer to locate on the grain boundaries of wrought alloys. Detrimental trace elements in the alloy also segregate

within grain boundaries. The combination of these factors can cause HAZ cracking to occur more easily along the grain boundaries.

4.4. Crack Length Measurement

The present study was undertaken to investigate the effects of welding parameters on the HAZ cracking during electron beam welding of Allvac 718 Plus alloy through a variation in welding parameters. To evaluate the HAZ cracking tendency under different electron beam welding conditions, total crack length in each cross section in the HAZ of a weld was measured. For each weld, the measurement of average total crack length in 8 sections was carried out with an optical microscope at a magnification of 500. The cracks on 480 sections were observed and their lengths were measured. The areas of the HAZ and the FZ were also measured using a digital optical microscope equipped with an image analysis system. The cracking index (CI) was designated to be the total crack length per unit area of HAZ in a cross section of the weld [4, 13], and given by

$$CI = \frac{\sum_{i=1}^n L_i}{A_{HAZ}} \quad (4-4)$$

Where, L_i is the length of crack, n is the number of cracks in HAZ, and A_{HAZ} is area of the HAZ on cross section. Approximately 10,000 cracks on 480 sections were measured. The experimental results are listed in Table 4-2. The total crack length on each section was different in 8 different sections of a weld. Thus, the total crack length scatter range is given by a standard deviation error (σ) in table 4-2.

4.5. Effects of Welding Parameters on Weld Shape and Crack Index

In the electron beam welding process, welding controlling parameters include accelerating voltage, beam current, welding velocity, beam spot size, and beam oscillation. In the present study, the accelerating voltage was kept at a constant value of 44kV, only four welding parameters were varied, i.e. welding velocity (V), beam current (I), oscillation in the cross (A_{my}) and the longitudinal (A_{mx}) directions. These welding parameters determined the weld shape and the HAZ cracking.

4.5.1. Heat Input Rate

Electron beam welding is a fusion process in which a high power density moving heat source is applied to a work-piece. The heat input to the weld determines the temperature in the fusion zone and the temperature gradients in the HAZ. The weld width and penetration depth, microstructure changes, and hot cracking in the HAZ also depend on the heat input. Usually, heat input depends upon the heat input rate in a welding process. The heat input rate $-Q$ (J/mm) is defined as the heat input into a unit weld length, which can be calculated for electron beam welding by [67]:

$$Q = \frac{UI}{V} \quad (4-5)$$

Where, U is the accelerating voltage (kV), I is the beam current (mA) and V is the welding velocity (mm/s). The heat input rate is a major factor affecting the weld shape and the HAZ cracking. Fig.4-18 indicates that the top weld width increases linearly with

the heat input rate. For those welds that did not penetrate through the thickness of the plate specimen, there was a linear relationship between the weld depth (D) multiplied the top width (W_p) and the heat input rate, which is shown in Fig.4-19. This suggests the more energy that is input into the weld, the wider is the weld, and the larger volume of materials is melted. The cracking index generally decreases with the heat input rate in EB welding process, as shown in Fig.4-20. Fig. 4-21 shows that when the oscillation along two directions is kept constant, the CI decreases rapidly with an increase in heat input rate, two direction oscillations were kept constant at $A_{mx}=A_{my}=50$ and $A_{mx}=A_{my}=25$, and results are shown in Fig.4-21a and Fig.4-21b respectively.

4.5.2. Effect of Electron Beam Oscillations

The electron beam was made to oscillate along the cross and longitudinal directions relative to a weld during welding in order to decrease the excessive evaporation of metal in the fusion zone. The effect of electron beam oscillations on the weld shape and the HAZ cracking is a possible problem to be concerned about. Figs.4-22 reveal the relation between the CI and the oscillations when the heat input rate was 261.7J/mm (i.e. $V = 35\text{in}/\text{min}$ and $I = 85\text{mA}$). Fig.4-22a shows the variation in the CI with the longitudinal direction oscillation when $A_{my} = 50$, while, Fig.4-22b shows the variation of the CI with the cross direction oscillation when $A_{mx} = 50$. On the basis of the data present in these figures, it can be concluded that, in the range of experimental error (the average error of CI is 0.22), CI did not change significantly with an increase in oscillation factor (oscillation amplitude) when the heat input rate was kept at a constant value of 261.7

J/mm. From table 3-3 and table 4-2, it would be seen that within the experimental error the effects of oscillations on the CI can be ignored for $Q=153, 323$ and 490 J/mm. Similarly, the oscillation amplitudes did not significantly affect the top width of welds, which as revealed in Figs.4-23. Fig. 4-23a indicates that the top width of weld did not change with a variation in oscillation score factor (A_{mx}) along the longitudinal direction, when the heat input (Q) was 261.7J/mm and the A_{my} was 50 , while, Fig.4-23b shows that the top width of weld did not change either with the variation in oscillation score factor (A_{my}) along the cross direction when $Q = 261.7\text{J/mm}$ and $A_{mx} = 50$. On the basis of the experimental data given in Table 3-3 and Table 4-2, the same conclusion, can be reached at the other heat input rates. Thus, the effect of oscillations on the CI within the present experimental condition was not desired to be significant.

4.5.3. Effect of Welding Velocity

Welding velocity is the moving speed of electron beam relative to the workpiece, which influences the heat input rate during welding. From equation (4-5), the heat input rate is inversely proportional to the welding velocity, i.e. the higher is the welding velocity, and the less is the heat input rate. From Fig.4-19, the smaller heat input rate leads to an increased value of CI. Figs.4-24 show the effect of welding velocity on the value of CI. It is seemed that CI increases rapidly with an increase in the welding velocity when the beam current and the oscillations are constant, even though the values of the CI scatter has a relatively large range. This could be explained if a relationship between the welding velocity and the temperature gradients in the HAZ has known. From thermal conduction views, the fast welding velocity causes steep temperature gradient and the

high level of thermal stress/strain in HAZ. As a result, many cracks could form in HAZ of the weld obtained at fast welding velocity. This will be discussed in detail in section 4.6 after calculation of the temperature gradient in HAZ.

4.5.4. Effect of Electron Beam Current

In the electron beam welding process, beam current represents the number of accelerating electrons striking the workpiece. These electrons can be accelerated to velocity of $0.3-0.7c$ (c is velocity of light). When they bombard a workpiece, the high kinetic energy of these electrons is converted into heat, that can cause the workpiece to be melted, and the welding to take place. The temperature in FZ and the temperature gradients across the HAZ are also dependent on the electron beam current, and affect the microstructural changes and cracking in a weld. Five beam currents were selected to investigate the effect of beam current on the HAZ cracking of Allvac 718Plus alloy. Figs 4-25 show that the CI decreases with an increase in electron beam current when the welding velocity is constant. The influence of electron beam current on the value of CI can be explained on the basis of the effect on the temperature gradient across the HAZ.

4.5.5. Multiple Linear Regression Analysis

Multiple linear regression analysis is extensively used to determine the relationship between a phenomenon and variables it depends upon. In the present study, the primary variables were the welding parameters, i.e. welding velocity (V), beam

current (I), oscillation along the cross (A_{my}), and the longitudinal direction (A_{mx}), the dependent on these is the value of CI. In the previous sections, the effect of the individual welding parameter on the CI was analyzed. In this section, the dependence of the value of CI on all the variables used in this study will be analyzed using multiple linear regression analysis method.

It is assumed that there is a linear relationship between the CI and the welding parameters, i.e.

$$CI = a_0 + a_1V + a_2I + a_3A_{mx} + a_4A_{my} \quad (4-6)$$

Where, a_0 is a constant and a_1, a_2, a_3, a_4 are numerical values, a computer executes a multiple regression analysis program. The output is listed in Table 4-3. From the values given in Table 4-3, Eq.(4-6) can be rewritten as:

$$CI = 0.643 + 0.0243V - 0.007I - 0.002A_{mx} - 0.0001A_{my} \quad (4-7a)$$

From Table 4-3, it can be seen that the probabilities for the two oscillation amplitudes are so large that these two variables should be ignored in the regression analysis. On the other hand, the average error of the measured CI is 0.22, and the change in the CI value due to variation in A_{mx} and A_{my} are 0.202 and 0.001 respectively, which are less than the average errors in crack length measurement. Thus, the effect of oscillation amplitudes along the two directions on the CI value is not significant.

Table 4-3. Multiple regression analysis results-A

Parameter	a _i Value	Error	t-Value	Prob> t
CI-Intercept	0.64302	0.27022	2.37964	0.02082
V	0.02427	0.00341	7.12015	<0.0001
I	-0.00702	0.00243	-2.88523	0.00558
A _{mx}	-0.00202	0.0017	-1.18343	0.24173
A _{my}	1.00E-04	0.0017	0.05868	0.95342
R-Square (COD)	Adj. R-Square		Root-MSE (SD)	
0.5235	0.48885		0.29516	
Item	Degrees of Freedom	Sum of Squares	Mean Square	F Statistic
Model	4	5.26405	1.31601	15.10627
Error	55	4.79143	0.08712	
Total	59	10.05549		
Prob>F	<0.0001			

Richards et al.[13] determined the effect of shape of the weld, defined by the depth/width ratio. In the current regression analysis, the ratio of the depth to the middle width (D/W_m) is taken as a variable in the multiple regression analysis. The analyzed results are listed in Table4-4. From the estimated coefficients given in Table4-4, the predicted CI can be expressed as:

$$CI = 0.805 + 0.0285 V - 0.0043 I - 0.058 \frac{D}{W_m} \quad (4-7b)$$

This empirical equation (4-7b) shows that the CI increases with an increase in the welding velocity; the increasing beam current results in a decrease of the CI. It also shows that the cracking is minimum when the ratio of depth to width of welds is maximum.

Table. 4-4 Multiple regression analysis results-B

Parameter	a_i Value	Error	t-Value	Prob> t
CI-Intercept	0.80493	0.24451	3.29196	0.00173
V	0.02858	0.00354	8.06927	<0.0001
I	-0.00427	0.00248	-1.71913	0.09111
D/Wm	-0.05772	0.02036	-2.83539	0.00636
R-Square (COD)	Adj. R-Square		Root-MSE (SD)	
0.57268	0.54979		0.277	
Item	Degrees of Freedom	Sum of Squares	Mean Square	F Statistic
Model	3	5.75861	1.91954	25.01677
Error	56	4.29688	0.07673	
Total	59	10.05549		
Prob>F	<0.0001			

Regarding the interaction of welding parameters affecting the HAZ cracking, the following regression analysis equation is obtained and the analyzed results are listed in Table 4-5.

$$CI = 1.77 + 0.07V - 0.057I + 0.0004I^2 - 0.0005VI \quad (4-8)$$

From the statistical analysis, Eq.(4-8) is better than Eq.(4-6) because the R^2 (COD) is larger, and the residuals, shown in Fig.4-26, are acceptable.

On the basis of Eq. (4-8), the partial difference of CI with respect to V is given by

$$\frac{\partial CI}{\partial V} = 0.07 - 0.0005I \quad (4-8a)$$

Let $\frac{\partial CI}{\partial V} = 0$, the critical value, $I_c = 140\text{mA}$. It means the CI value increases with the welding velocity in the present study because all of the beam currents are less than 140mA . However, the partial difference of CI with respect to I is given by

$$\frac{\partial CI}{\partial I} = -0.057 + 0.0008 I - 0.0005 V \quad (4-8b)$$

The change of CI with an increase in beam current is complex, which is dependent on the values of I and V .

Table4-5 Multiple linear regression analysis results-c

Parameter	a_i Value	Error	t-Value	Prob> t
CI-Intercept	1.76868	1.00634	1.75754	0.08439
V	0.06968	0.01782	3.90993	2.56E-04
I	-0.05679	0.02017	-2.8147	0.00676
I^2	4.03E-04	1.10E-04	3.65842	5.70E-04
$V*I$	-5.34E-04	2.07E-04	-2.58403	0.01245
R-Square (COD)	Adj. R-Square		Root-MSE (SD)	
0.64194	0.6159		0.25586	
Item	Degrees of Freedom	Sum of Squares	Mean Square	F Statistic
Model	4	6.45501	1.61375	24.65134
Error	55	3.60047	0.06546	
Total	59	10.05549		
Prob>F	<0.0001			

4.6. Evaluation of Temperature Distribution and Temperature Gradient in the HAZ

It is well known that the high temperature and the steep temperature gradient in the HAZ of a weld lead to the HAZ cracking. It would be extremely useful to predict the distribution of the temperature and its gradient in the HAZ in order to completely understand the microstructure change and the hot cracking in the HAZ. In the electron

beam welding process, the temperature and its gradient are dependent on the welding parameters and the thermal properties of the base metal. Experimentally, it is difficult to measure directly the temperature distribution around an electron beam weld. So, the theoretical evaluation of temperature and its gradient in the HAZ is very important to understand the occurrence of the HAZ cracking, although it usually requires a number of simplifying assumptions, e.g. heat source and thermal properties of base metal. Generally, to describe the temperature gradient across HAZ is a complex process, therefore several models have been developed for the calculation of the temperature distribution that occur during different welding methods [19-25]. Regarding the EB welding, Passoja [19] developed an analytical expression based on the plane heat source approximation to describe the temperature distribution in the HAZ.

$$T(Y, t) - T_R = \frac{(T_B - T_R)H}{2\sqrt{\pi\alpha t}} \exp\left(\frac{-Y^2}{4\alpha t}\right) \quad (4-9)$$

$$\frac{dT}{dY} = -\frac{Y}{2\alpha t} \frac{(T_B - T_R)H}{2\sqrt{\pi\alpha t}} \exp\left(\frac{-Y^2}{4\alpha t}\right) \quad (4-10)$$

Where, H is the heat source width in mm, Y is the distance from the heat source center line in mm, T_B is the beam temperature in °C, T_R is the ambient temperature in °C, α is the thermal diffusivity in mm^2/s . The temperature distribution around an EB weld given by expression (4-9) is dependent on electron beam width, electron beam residence time on the weld, and thermal diffusivity of the base metal.

In the current experiment, the electron beam was sharply focused on the surface of weld specimens during welding. The electron beam spot diameter was about 0.3mm. While the electron beam was set up to oscillate along the cross direction (Y direction). According to Richards et al's experimental report [68], the oscillation amplitude increases linearly with the score factor, which is shown in Fig.4-27. The oscillation amplitudes along two directions (A_{mx} and A_{my}) given in Table 3-3 are the score factors. From Fig.4-27, it is easy to obtain the real amplitude along the cross direction. The electron beam width (H), therefore, is determined by adding the electron beam spot diameter to the oscillation amplitude along the cross direction. However, the fusion zone width varies with weld depth, which can be seen from Fig.4-4. To estimate the temperature distribution in the HAZ and to compare the effects of welding parameters on the temperature distribution, it is assumed that the temperature field near the neck of a nail-head of electron beam weld can be described by expression (4-9). In other words, it is considered that the ideal plane heat source is used to heat the weld at the neck of a nail-head weld. Then, it is reasonable to assume that the fusion line temperature of a weld remain constant, that is liquidus/solidus of the Allvac 718Plus alloy given in Table 3-2 remain unchanged. For convenience, the temperature at the fusion line is taken as 1300°C, because from the microstructural observation, it is impossible to ensure whether the temperature on fusion line is liquidus (1353°C) or solidus (1265°C).

The electron beam heating time is a major factor in determining the temperature distribution, which is directly related to the welding velocity. To compare the effect of welding velocity on the temperature distribution, the characteristic time (t_0) is taken as the time when the electron beam passes through a unit length (1mm) of a weld, i.e.

$$t_0 = \frac{1}{V} \quad (4-11)$$

Where, V is the welding velocity mm/s Thus, only five welding velocities (10, 22.5, 35, 47.5 and 60 in/min) were used in the present study. The corresponding characteristic time is 0.245, 0.109, 0.071, 0.052 and 0.041 second respectively.

The thermal diffusivity of this alloy is a function of temperature. The present study stresses on the high temperature range and grain boundary liquation in the HAZ, so that the thermal diffusivity of $\alpha=5.3 \text{ mm}^2/\text{s}$ at temperature 1200°C is used in the relevant calculations.

Using equation (4-9) to compute the temperature and its gradient in the HAZ, the beam temperature (T_B) has to be known. It is assumed that the temperature on the fusion line is fixed at 1300°C . The fusion line position i.e. the value of Y_F (the interesting position) can be measured on the cross section of welds. Then, substituting them into equation (4-9), the value of T_B can be computed.

So far, the computations of equations (4-9) and (4-10) can be easily done on the basis of the assumptions mentioned above. The calculated results are illustrated in Figs. 4-28. Fig.4-28a indicates that the temperature decreases with distance from the fusion line, the lower the welding velocity, the wider is the weld. Whereas Fig.4-27b shows that the temperature gradients vary with distance from the fusion line to matrix for different welding velocities. It is very significant that the high welding velocity results in a short electron beam heating time and the steeper temperature gradient in HAZ. The calculated results indicate that the maximum temperature gradient for welding velocity of 47.5in/min is twice as high as that for welding velocity of 10in/min. This result is

consistent with the basic knowledge, that the fast welding velocity causes steeper temperature gradients. The induced thermal stress in HAZ by a rapid change in temperature is proportional to the temperature gradient, so, high stresses are generated when the welding velocity is high. It means that the HAZ will suffer high stress action in a high velocity welding process, and more cracks will easily form and the value of total crack length will be greater. Additionally, from Fig.4-28a, it can be seen that the width of the HAZ of weld made at a high welding velocity is also narrower than that of weld made at a lower welding velocity. In other words, the area of the HAZ of a weld made at higher welding velocity is smaller than that of weld made at a lower welding velocity. This would explain the experimental observation of an increase in the value of CI increasing with welding velocity, shown in Fig.4-24.

In reality, all the physical change around a weld such as temperature and microstructure is implemented through the heat flow and heat conduction from the heat source to the metal. The heat flow or conduction process is a dynamic process during welding. Controlling welding process is actually controlling the heat input to the weld. The heat input rate is inversely proportional to the welding velocity. The higher the welding velocity, the less the input heat rate to the workpiece. This is why the cracking index decreases with heat input rate (see Fig.4-20). Based on this discussion, it is easy to understand why a higher beam current and a higher heat input rate, causes a reduced cracking.

Table 4-2 Measured results on 480 cross sections of 60 EB welds

Run	μm	Sections								Sum Max	Lc (μm)	σ (μm)	D (mm)	W _p (mm)	W _s (mm)	W _m (mm)	A _{FZ} (cm^2)	A _{HAZ} (cm^2)	CI (cm^{-1})	ΔCI (cm^{-1})
		1	2	3	4	5	6	7	8											
1	L	911	939	262	168	507	655	643	1031	5116	640	296	14.381	3.961	1.470	1.080	0.154	0.1349	0.474	0.219
	Max	134	352	84	64	187	98	120	180	352	152									
2	L	630	998	657	311	415	654	315	743	4723	590	219	13.509	4.019	1.483	1.138	0.152	0.1350	0.437	0.162
	Max	132	303	188	151	140	97	49	148	303	151									
3	L	540	665	407	228	642	653	636	774	4545	568	163	14.494	4.166	1.843	1.426	0.174	0.1502	0.378	0.108
	Max	130	150	171	228	100	140	145	142	228	151									
4	L	995	729	859	751	946	1505	483	852	7120	890	275	14.755	3.487	1.281	0.965	0.164	0.1449	0.614	0.190
	Max	235	102	106	99	184	184	63	152	235	141									
5	L	669	1177	1387	830	704	1029	1253	1190	8239	1030	250	7.745	3.544	1.567	1.210	0.093	0.0617	1.670	0.406
	Max	287	148	429	135	104	269	240	205	429	227									
6	L	1000	1567	2281	1406	1850	1639	2218	1197	13158	1645	426	13.882	4.033	1.570	1.022	0.160	0.1210	1.359	0.352
	Max	265	148	367	127	237	120	185	136	367	198									
7	L	1006	967	641	1031	879	413	1211	531	6679	835	259	14.700	4.163	1.714	1.210	0.173	0.1288	0.648	0.201
	Max	195	87	156	216	88	159	126	71	216	137									
8	L	626	1231	774	531	873	711	928	502	6176	772	224	13.869	3.891	1.483	0.951	0.153	0.1227	0.629	0.183
	Max	85	184	254	140	131	114	246	90	254	156									
9	L	974	1157	929	521	732	1011	1095	769	7188	899	197	10.691	2.741	1.214	0.934	0.095	0.0583	1.542	0.339
	Max	208	200	168	163	176	108	118	63	208	151									
10	L	1254	1118	1380	1535	1658	1771	1312	869	10897	1362	274	PT	5.144	1.786	1.483	0.262	0.1936	0.704	0.142
	Max	185	121	128	154	283	304	183	148	304	188									
11	L	824	1612	821	763	1550	1168	1122	1245	9105	1138	306	9.644	3.299	1.340	0.965	0.094	0.0650	1.750	0.470
	Max	272	153	223	277	202	133	143	148	277	194									
12	L	1450	1506	1453	2413	2622	2645	1491	816	14396	1800	628	12.971	3.933	1.456	1.094	0.155	0.1217	1.479	0.516
	Max	163	256	253	221	206	274	126	240	274	217									
13	L	920	893	1170	571	833	1392	627	1632	8038	1005	345	14.009	4.178	1.413	0.937	0.154	0.1110	0.905	0.311
	Max	155	135	323	86	176	134	124	211	323	168									
14	L	1002	1148	1033	936	976	719	939	1024	7777	972	114	14.285	4.149	1.815	1.065	0.173	0.1325	0.734	0.086

15	Max	371	347	156	219	355	153	147	107	371	232										
	L	1670	1547	2118	855	1249	1124	1140	834	10537	1317	409	13.509	3.630	1.426	1.037	0.108	0.1192	1.105	0.343	
16	Max	220	206	152	214	159	100	182	132	220	171		PT	8.127	2.625	2.261	0.458	0.4581	0.113	0.039	
	L	712	792	476	693	366	418	251	428	4136	517	179									
17	Max	77	59	50	130	62	59	54	65	130	70		PT	5.259	1.830	1.397	0.439	0.2511	0.329	0.121	
	L	991	1003	1435	487	821	469	568	831	6605	826	304									
18	Max	36	172	246	64	149	143	72	194	246	135		9.341	3.155	1.210	1.023	0.088	0.0768	1.486	0.397	
	L	1043	1448	1408	523	1455	874	1112	1272	9135	1142	305									
19	Max	184	334	270	166	158	115	265	155	334	206		13.910	4.004	1.412	1.124	0.160	0.1211	0.700	0.305	
	L	1415	970	1327	329	720	782	364	875	6782	848	369									
20	Max	264	176	510	79	96	81	108	101	510	177		9.200	3.169	1.483	0.979	0.097	0.0716	1.155	0.313	
	L	866	909	1031	648	412	725	822	1196	6609	826	224									
21	Max	36	174	127	241	92	141	141	226	241	147		14.285	4.365	1.757	1.224	0.184	0.1571	0.478	0.068	
	L	933	750	838	624	618	787	643	814	6007	751	107									
22	Max	197	80	107	117	75	57	74	251	251	120		PT	4.336	1.527	1.513	0.230	0.1762	0.783	0.164	
	L	1158	1994	1166	1374	994	1506	1303	1537	11032	1379	289									
23	Max	110	516	141	282	208	156	114	250	516	222		13.329	3.933	1.549	1.267	0.154	0.1480	0.535	0.162	
	L	610	998	1283	562	932	715	664	570	6334	792	240									
24	Max	161	191	283	116	149	156	264	240	283	195		14.284	3.947	1.354	1.066	0.161	0.1308	0.758	0.151	
	L	664	1165	929	1221	752	1042	933	1229	7935	992	198									
25	Max	91	275	138	102	141	114	140	229	275	154		15.574	5.041	1.829	1.656	0.257	0.2429	0.565	0.128	
	L	1616	1738	955	1331	1142	1396	1819	991	10988	1374	310									
26	Max	174	161	106	254	102	149	217	112	254	159		14.620	4.510	1.584	1.267	0.180	0.1703	0.347	0.130	
	L	825	1046	432	526	373	622	549	360	4733	592	222									
27	Max	178	101	71	51	98	133	257	96	257	123		14.092	3.457	1.440	1.080	0.145	0.1025	1.309	0.535	
	L	1398	1350	1185	751	2654	900	1034	1464	10736	1342	548									
28	Max	224	192	129	120	228	107	224	219	228	180		PT	4.739	1.801	1.412	0.257	0.2077	0.770	0.211	
	L	2143	1735	1829	2254	1014	1085	1494	1238	12792	1599	439									
29	Max	144	302	186	217	118	150	143	167	302	178		9.446	3.299	1.240	1.065	0.099	0.0723	1.384	0.223	
	L	783	1138	1161	876	881	1162	827	1174	8002	1000	161									
	Max	176	212	185	102	173	113	121	274	274	170										

30	L	837	1308	1406	1289	1245	964	1555	958	9562	1195	233	13.842	3.501	1.397	0.994	0.142	0.1066	1.121	0.219
	Max	116	162	145	238	187	219	131	168	238	171									
31	L	976	1191	917	539	455	909	961	1923	7871	984	420	12.644	5.318	1.998	1.366	0.198	0.1863	0.528	0.226
	Max	172	220	188	115	89	251	142	202	251	172									
32	L	1146	1128	1404	1173	791	994	694	1349	8679	1085	232	9.946	3.466	1.528	1.069	0.097	0.0896	1.239	0.266
	Max	191	147	144	127	156	148	141	209	209	158									
33	L	1190	831	1291	776	552	904	1158	730	7432	929	242	9.961	3.423	1.483	0.955	0.101	0.0679	1.368	0.356
	Max	127	124	167	118	88	206	194	210	210	154									
34	L	560	268	662	664	600	658	246	797	4455	557	185	13.999	4.979	1.953	1.410	0.138	0.1961	0.284	0.094
	Max	82	109	83	103	129	173	67	143	173	111									
35	L	2079	1837	1205	899	1108	1712	682	663	10185	1273	507	PT	5.436	2.364	1.586	0.234	0.3074	0.414	0.165
	Max	206	192	109	250	130	244	103	122	250	170									
36	L	1183	1344	1108	1161	1174	1233	264	827	8294	1037	323	13.858	4.275	1.733	1.292	0.130	0.1783	0.582	0.181
	Max	208	160	265	195	127	331	70	186	331	193									
37	L	1451	658	1115	1411	1094	1060	1311	1111	9211	1151	235	13.321	4.142	1.601	1.146	0.159	0.1186	0.970	0.198
	Max	153	79	156	234	209	129	292	124	292	172									
38	L	1153	919	1268	1070	1075	616	1295	1427	8823	1103	236	13.322	3.878	1.478	1.116	0.164	0.0991	1.113	0.238
	Max	165	102	110	164	150	99	140	146	165	135									
39	L	1511	920	680	950	873	1692	1379	1265	9270	1159	332	9.461	3.540	1.278	0.998	0.110	0.0695	1.668	0.477
	Max	443	145	174	161	157	346	331	145	443	238									
40	L	768	845	973	802	848	1056	289	887	6468	809	215	12.519	5.096	1.792	1.381	0.196	0.1478	0.541	0.145
	Max	231	120	162	104	110	273	51	102	273	144									
41	L	935	1139	613	554	791	860	358	534	5784	723	237	14.297	5.243	1.630	1.439	0.209	0.1398	0.517	0.170
	Max	117	186	136	113	85	123	45	92	186	112									
42	L	1004	904	805	1642	972	1400	1105	477	8309	1039	334	7.784	4.054	1.439	1.130	0.110	0.0710	1.462	0.470
	Max	248	242	126	150	190	532	183	156	532	228									
43	L	859	820	926	947	498	709	959	530	6248	781	172	9.565	3.804	1.395	1.013	0.064	0.1056	0.740	0.163
	Max	351	137	128	215	175	161	276	85	351	191									
44	L	1088	356	878	971	583	1069	883	1334	7162	895	286	13.109	4.436	1.690	1.190	0.129	0.1816	0.493	0.157
	Max	92	97	149	275	288	230	137	267	288	192									
45	L	1472	607	513	1395	728	960	1496	778	7949	994	378	14.070	3.951	1.468	1.263	0.145	0.1769	0.562	0.213

	Max	196	109	109	144	220	164	178	100	220	153									
46	L	1414	1064	889	1230	1268	1214	1377	1007	9463	1183	171	PT	5.986	1.869	1.661	0.313	0.1896	0.624	0.090
	Max	297	253	134	127	116	189	284	243	297	205									
47	L	846	573	863	895	720	1497	1520	513	7427	928	358	PT	4.633	1.644	1.145	0.176	0.1414	0.656	0.253
	Max	36	99	184	106	111	415	215	67	415	154									
48	L	1305	2478	1343	2109	1874	2385	1576	1968	15038	1880	416	8.786	4.672	1.733	1.395	0.262	0.2044	0.920	0.204
	Max	229	190	198	222	435	258	269	139	435	243									
49	L	824	320	912	623	1133	682	1417	748	6659	832	311	13.252	3.863	1.718	1.087	0.156	0.1138	0.731	0.273
	Max	134	55	160	113	182	171	200	126	200	143									
50	L	599	730	860	709	452	724	1049	387	5510	689	199	12.969	4.597	1.513	1.174	0.178	0.1475	0.467	0.135
	Max	145	159	93	167	90	114	182	121	182	134									
51	L	443	893	1377	1307	1650	1071	982	598	8321	1040	377	13.251	3.922	1.527	1.044	0.155	0.1146	0.908	0.329
	Max	80	119	166	166	298	123	196	75	298	153									
52	L	454	974	605	843	1163	471	662	998	6170	771	245	13.396	4.436	1.543	1.058	0.167	0.1180	0.653	0.208
	Max	127	157	227	186	212	122	153	165	227	169									
53	L	719	1426	260	976	542	1287	1063	1096	7369	921	365	14.042	4.744	1.615	1.176	0.183	0.1183	0.778	0.308
	Max	100	254	61	142	145	166	257	123	257	156									
54	L	1159	895	523	875	946	743	1294	1205	7640	955	240	13.843	4.524	1.525	1.058	0.186	0.1462	0.653	0.164
	Max	208	179	146	121	171	82	197	178	208	160									
55	L	579	1320	1476	1340	1647	1379	613	977	9331	1166	373	PT	9.688	4.887	2.345	0.451	0.4295	0.272	0.087
	Max	66	115	229	97	178	114	86	163	229	131									
56	L	513	818	576	1080	804	1227	772	766	6556	820	222	9.607	4.538	1.528	1.087	0.163	0.1417	0.578	0.156
	Max	153	155	128	178	285	215	127	122	285	170									
57	L	1149	1184	882	1246	1928	697	2639	825	10550	1319	611	PT	6.332	2.321	1.483	0.290	0.2648	0.498	0.231
	Max	106	227	99	113	218	147	197	166	227	159									
58	L	775	731	441	630	727	891	624	695	5514	689	123	PT	3.368	1.276	0.919	0.097	0.0855	0.806	0.144
	Max	113	192	245	158	223	176	231	125	245	183									
59	L	529	805	685	443	942	1047	656	715	5822	728	188	PT	5.802	2.056	1.718	0.394	0.3478	0.209	0.054
	Max	170	124	320	175	198	156	100	247	320	186									
60	L	351	568	733	637	692	910	692	735	5318	665	150	13.266	4.671	1.821	1.101	0.178	0.1676	0.397	0.089
	Max	84	210	155	63	172	130	98	132	210	131									

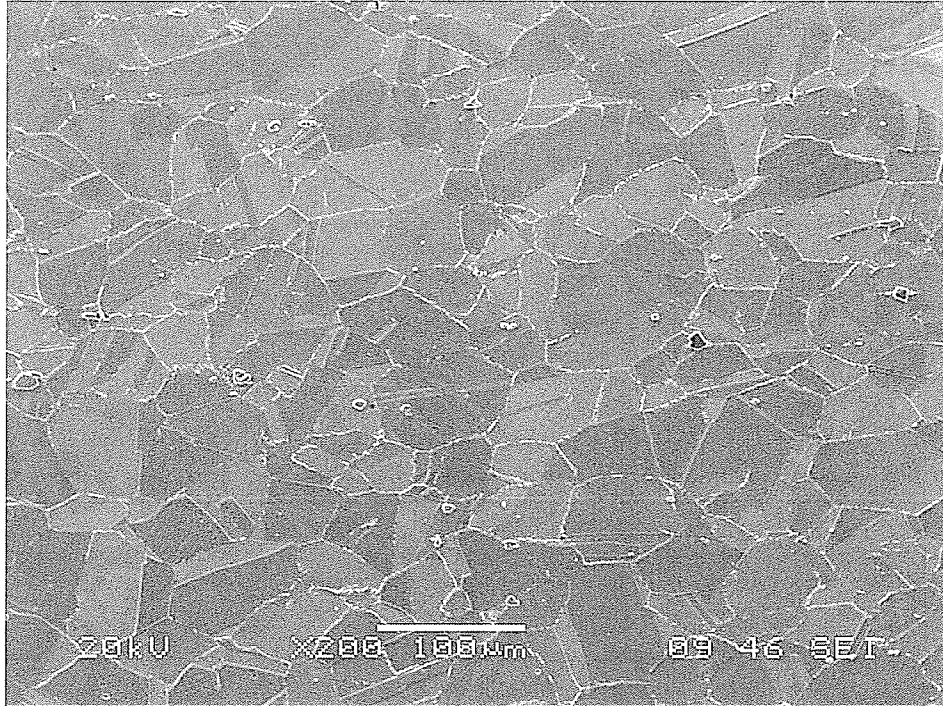


Fig.4-1 SEM micrograph showing the microstructure of the base metal of Allvac 718Plus alloy after solution-heat treatment

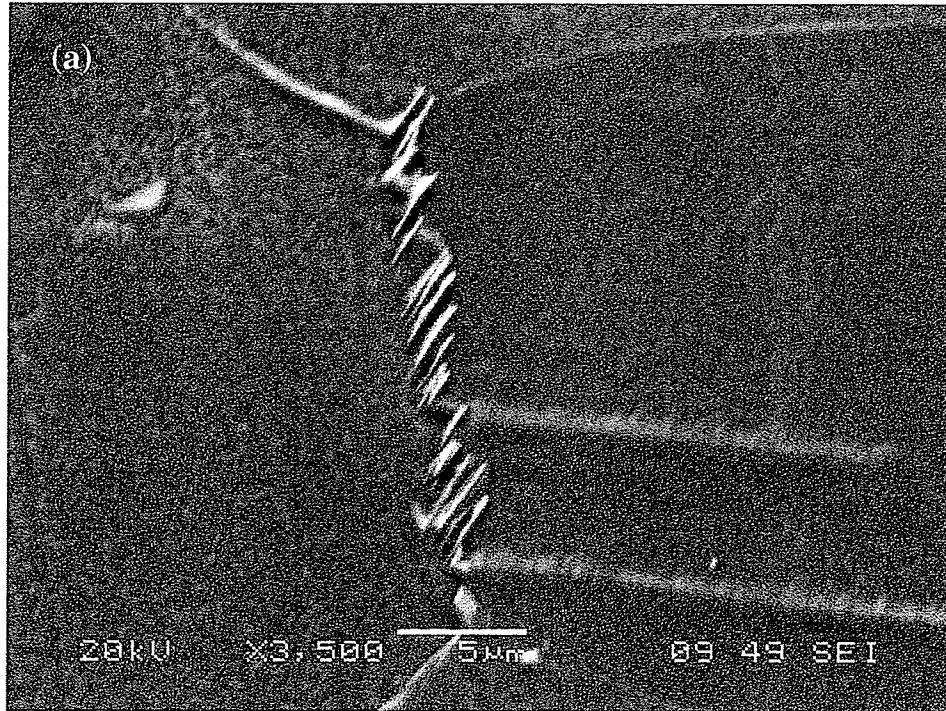


Fig.4-2. Delta phase morphology around grain boundary in the base metal of Allvac 718Plus alloy after solution-heat treatment. a) SEM micrograph b) TEM micrograph (BF) with diffraction pattern, and c) EDS and the compositions of delta phase by TEM

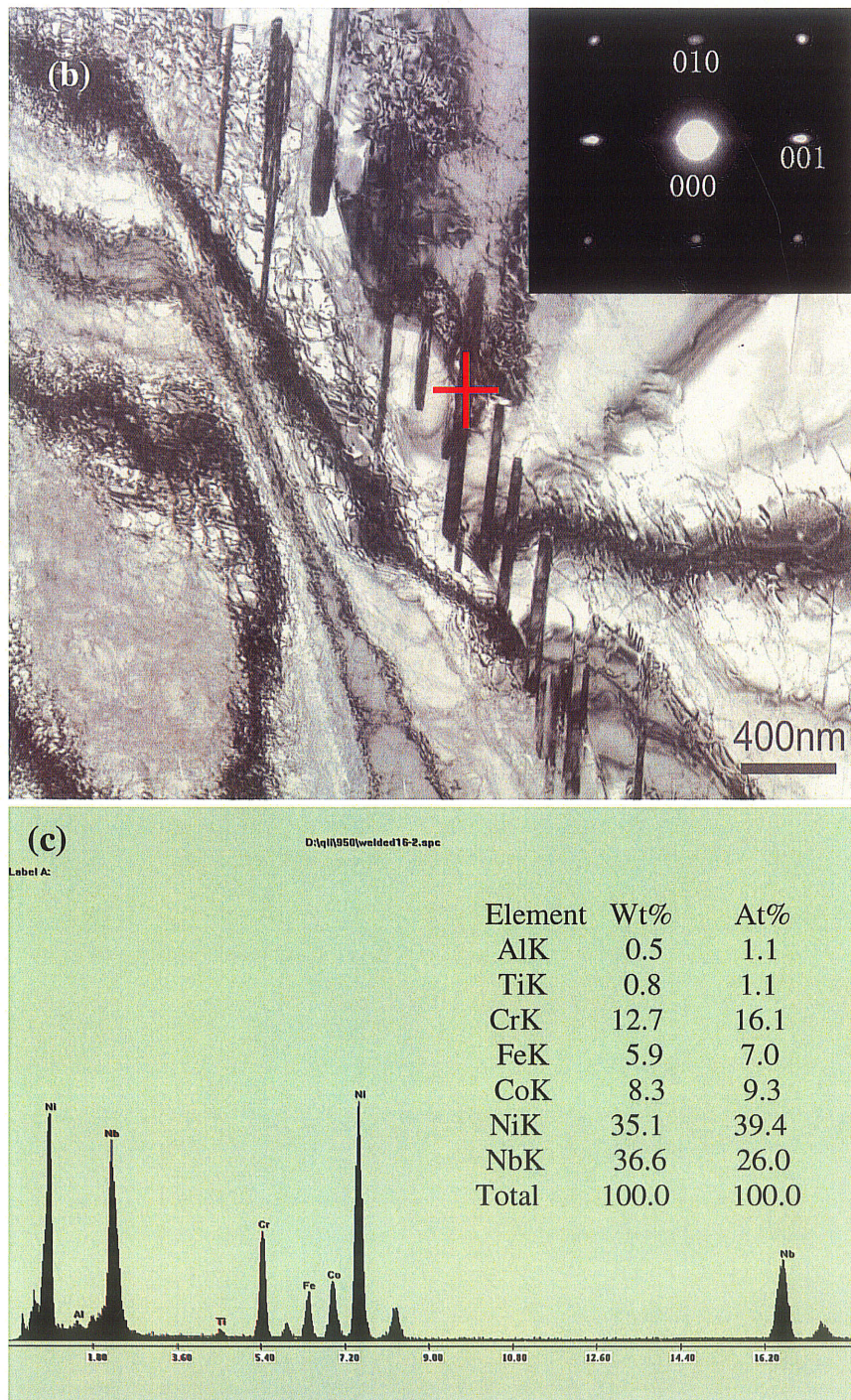


Fig.4-2. Delta phase morphology around grain boundary in the base metal of Allvac 718Plus alloy after solution-heat treatment. a) SEM micrograph b) TEM micrograph (BF) with diffraction pattern, and c) EDS and the compositions of delta phase by TEM

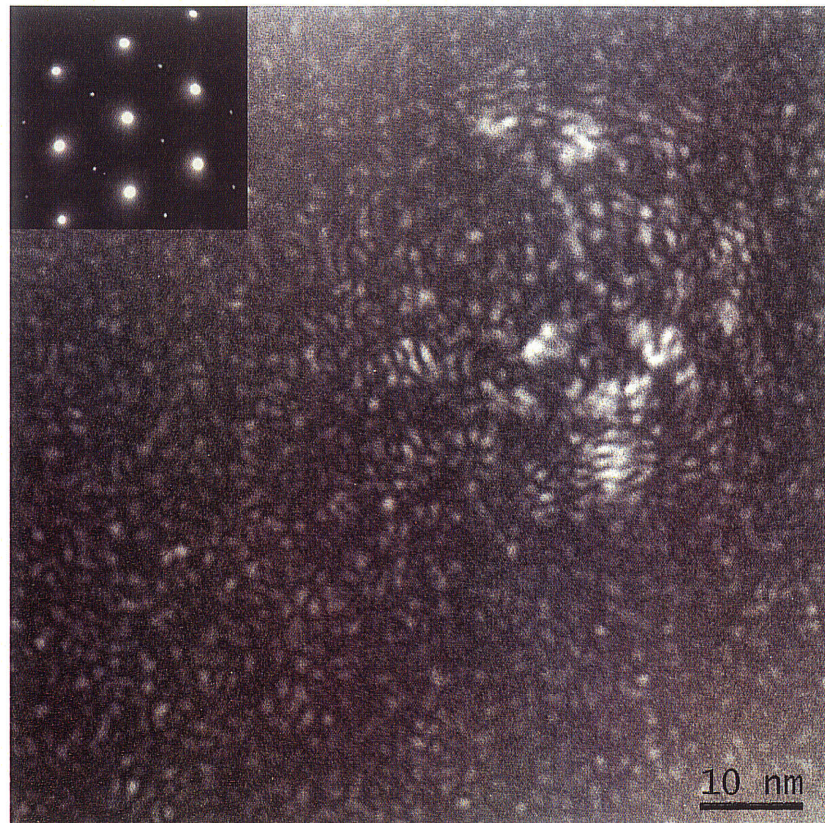


Fig.4-3. DF image of small γ' phase in the base metal taken with FEG TEM

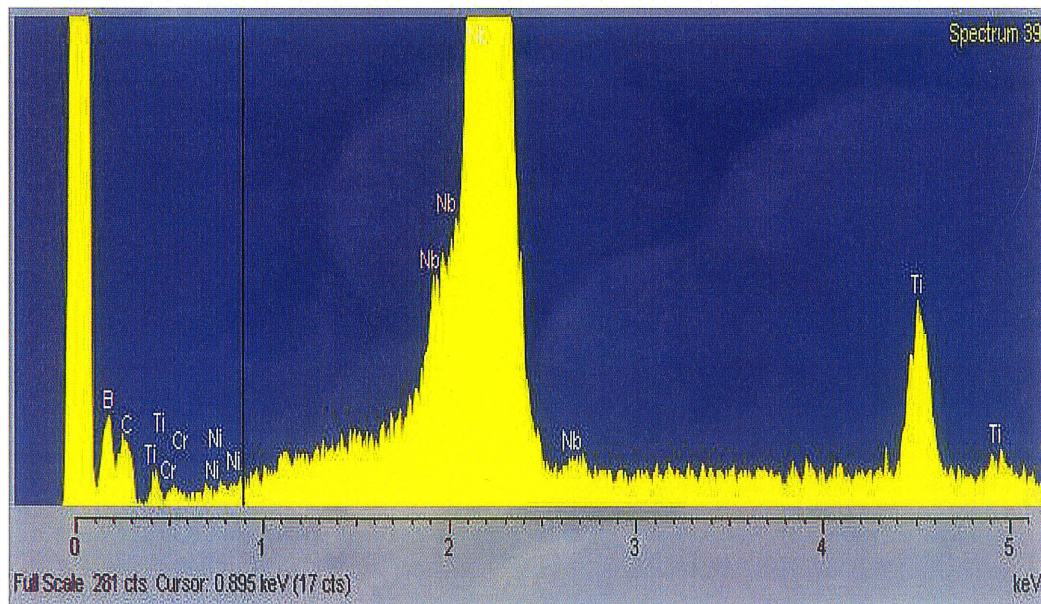
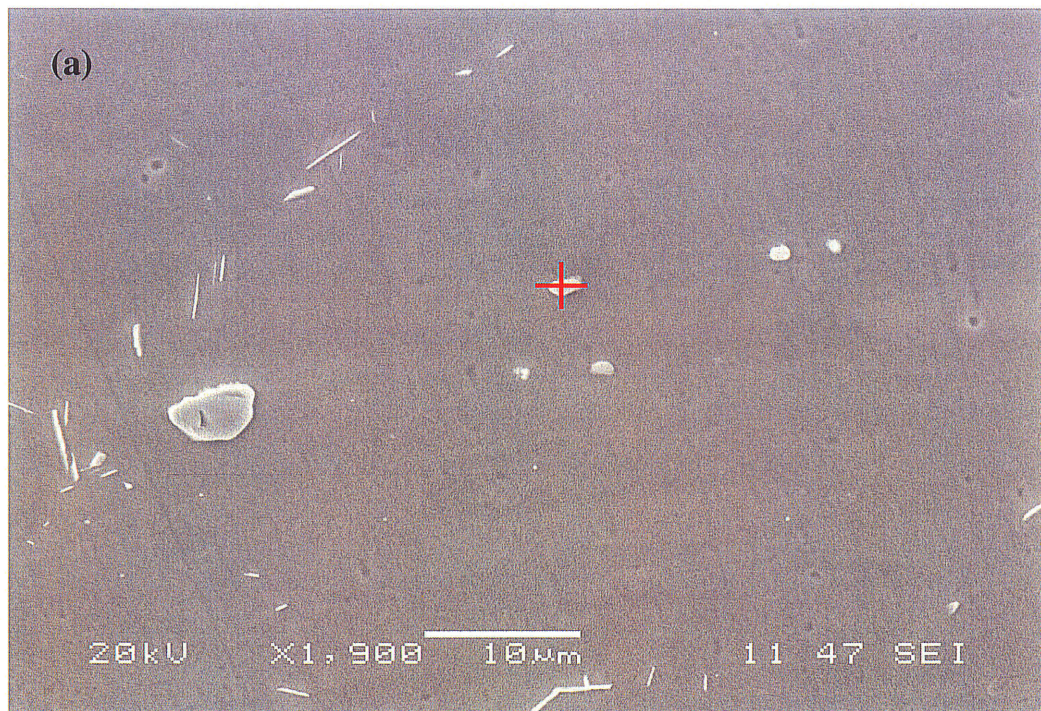


Fig.4-4. Second phase $[NbX(B,C)]$ being in a grain (a) and on a grain boundary (b)

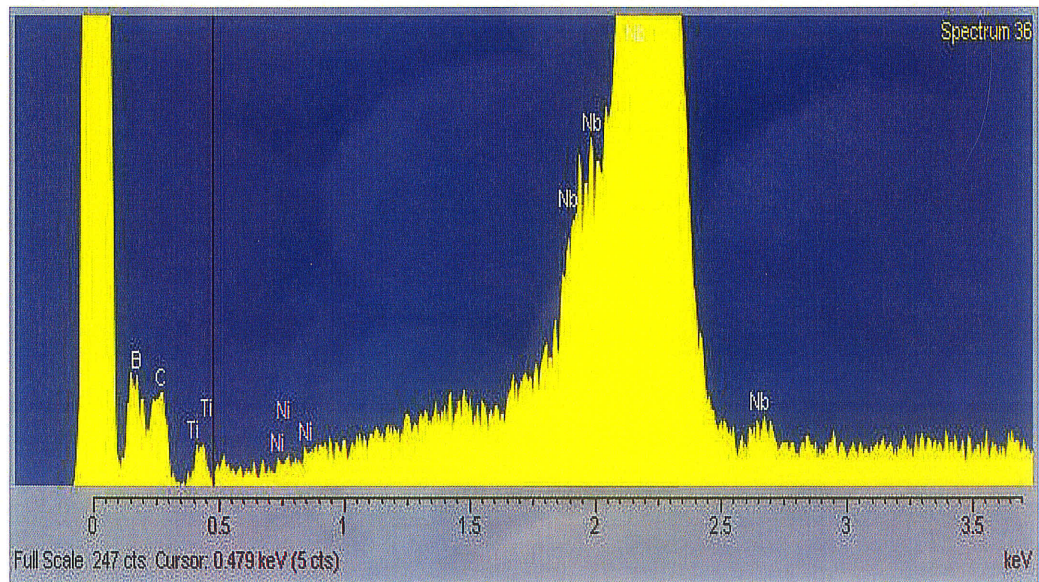
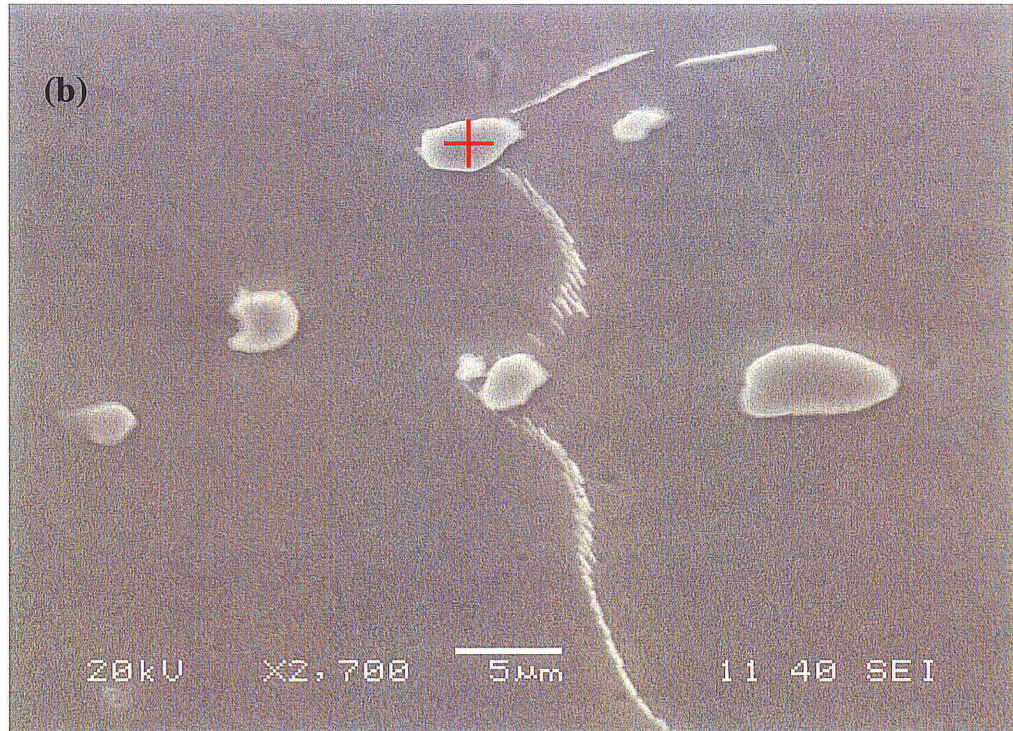


Fig.4-4. Second phase [NbX(B,C)] being in a grain (a) and on a grain boundary (b)

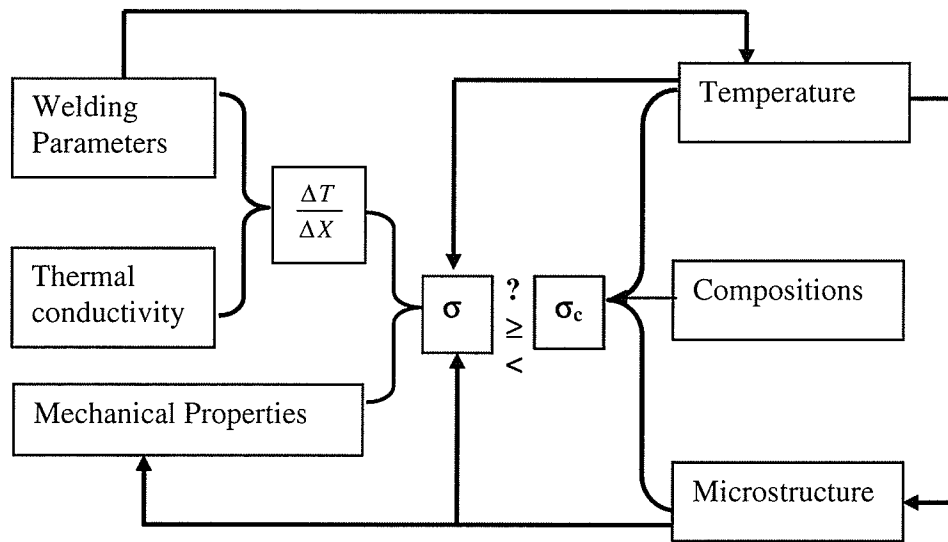


Fig.4-5 Schematic diagram showing factors affecting the HAZ cracking in welding

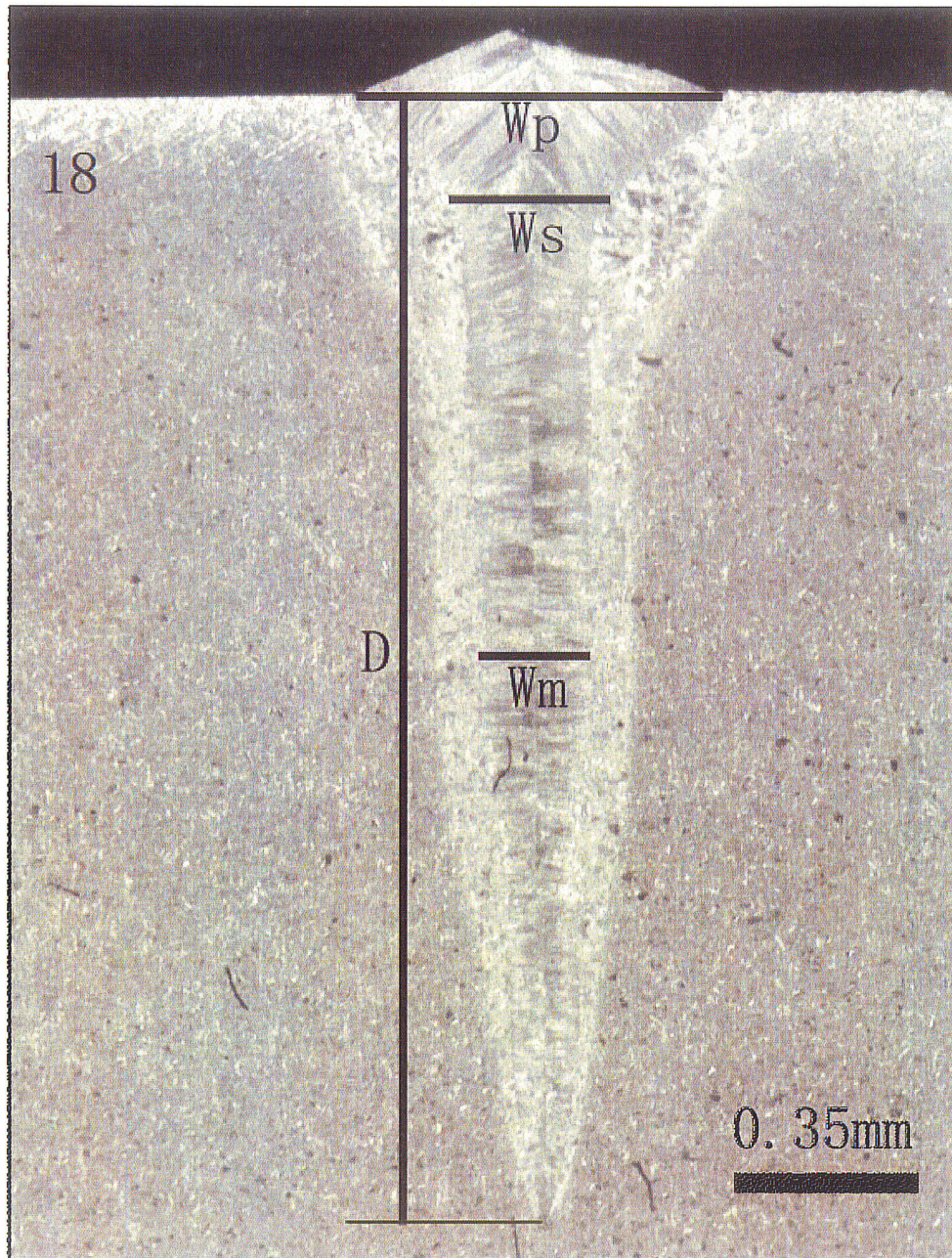


Fig.4-6. A typical nail-head shape of weld obtained with EB welding and its geometrical parameters.

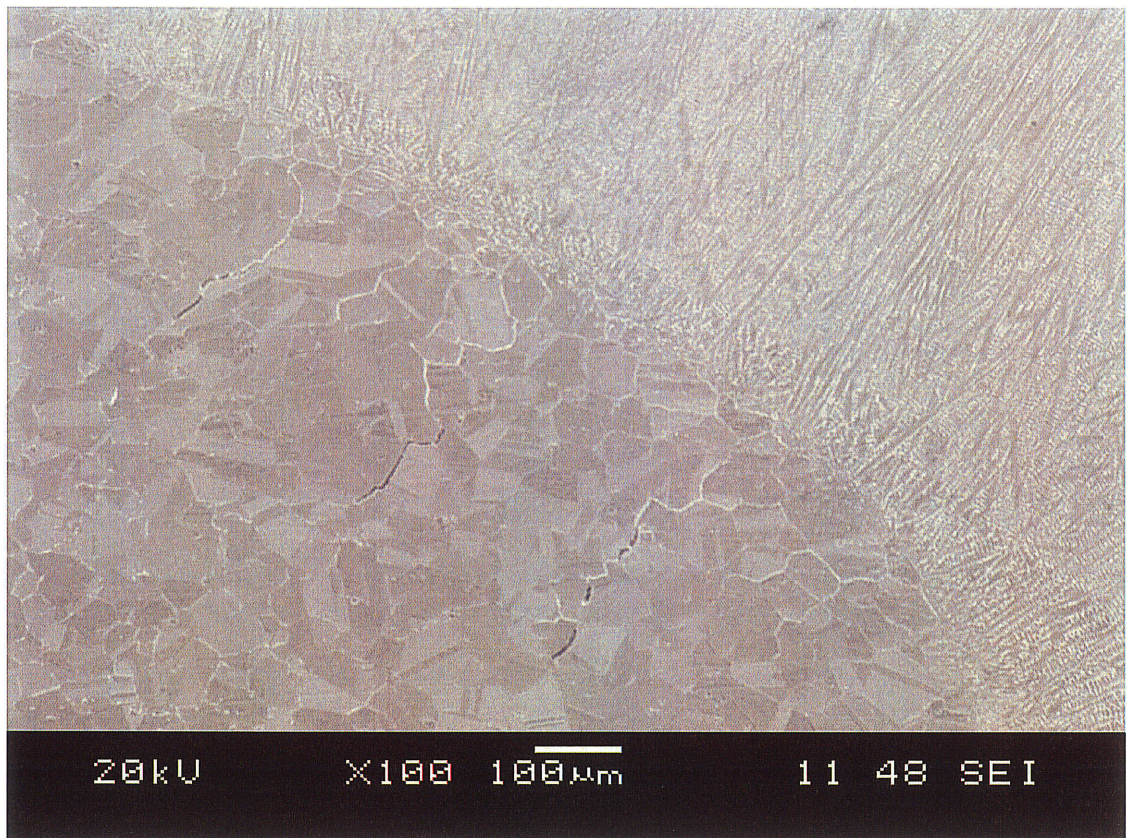


Fig.4-7. SEM micrograph illustrating cracks distribution in HAZ of an EB weld.

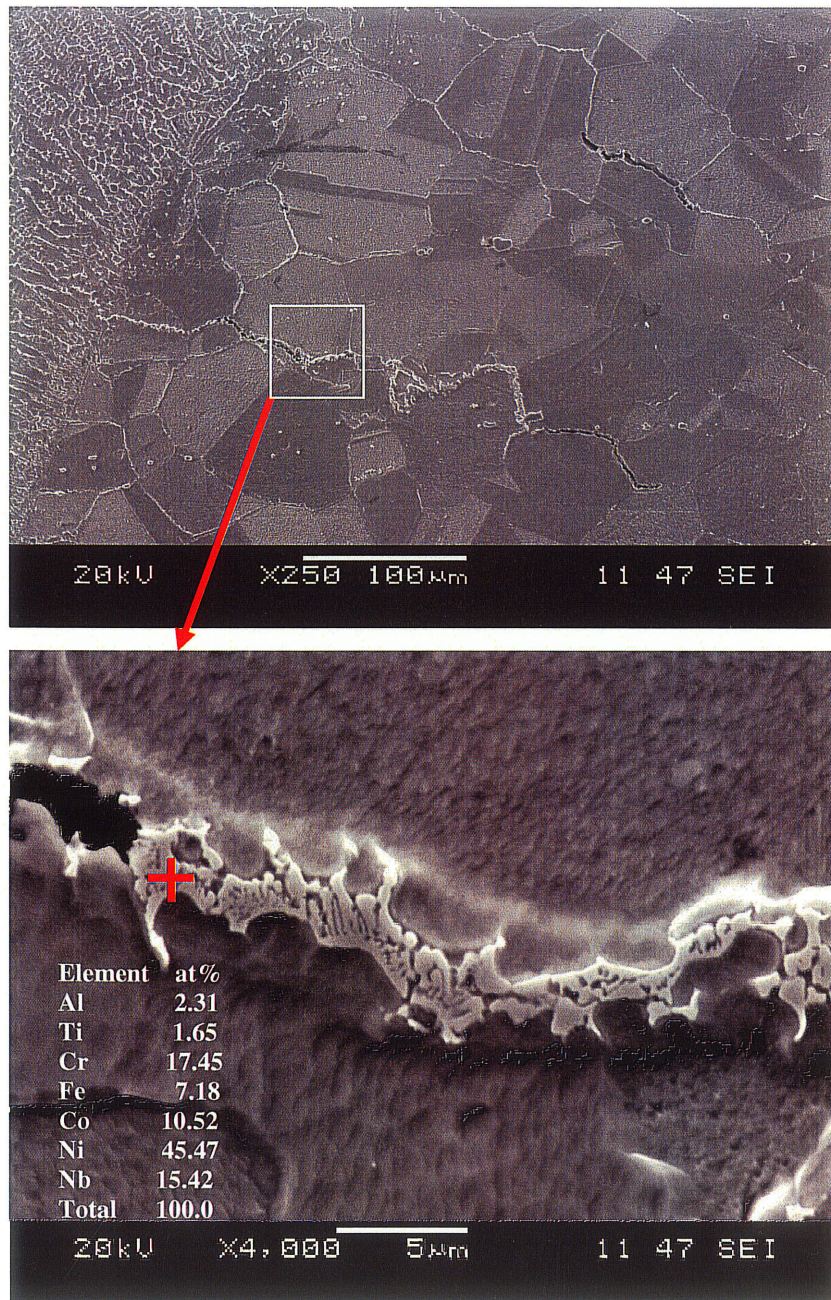


Fig.4-8. SEM micrographs illustrating cracks with the resolidified-products and the compositions of the resolidified-products from EDS.

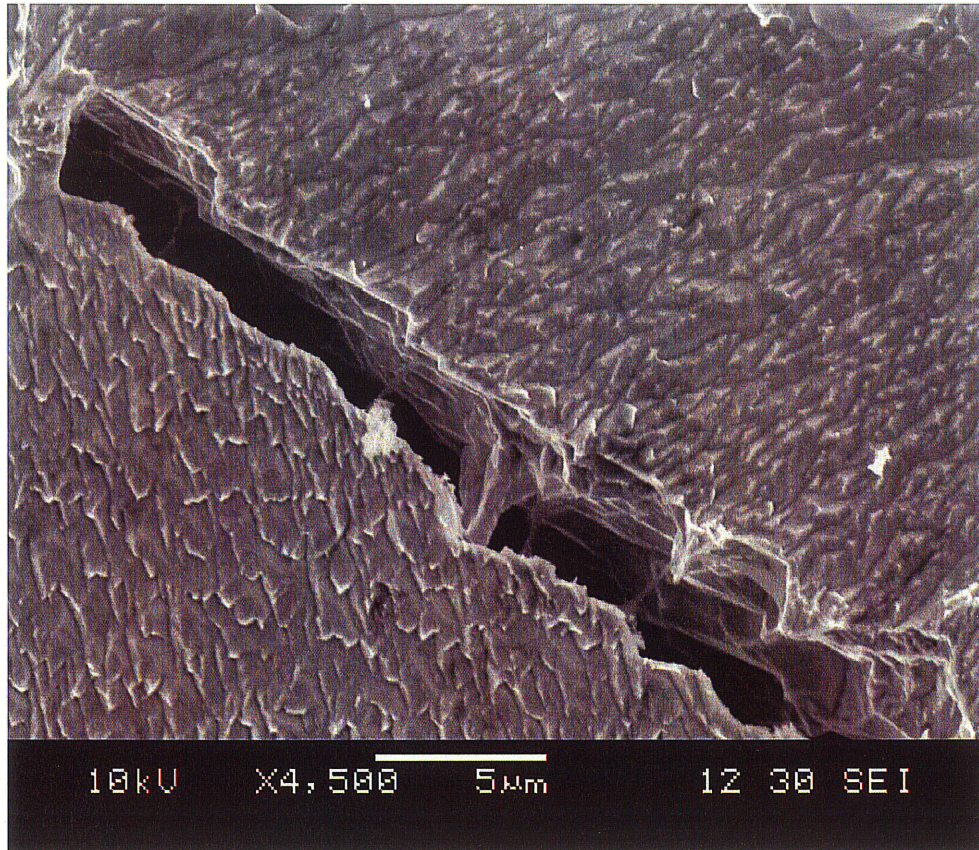


Fig.4-9. SEM micrograph showing a crack without the resolidified-products.

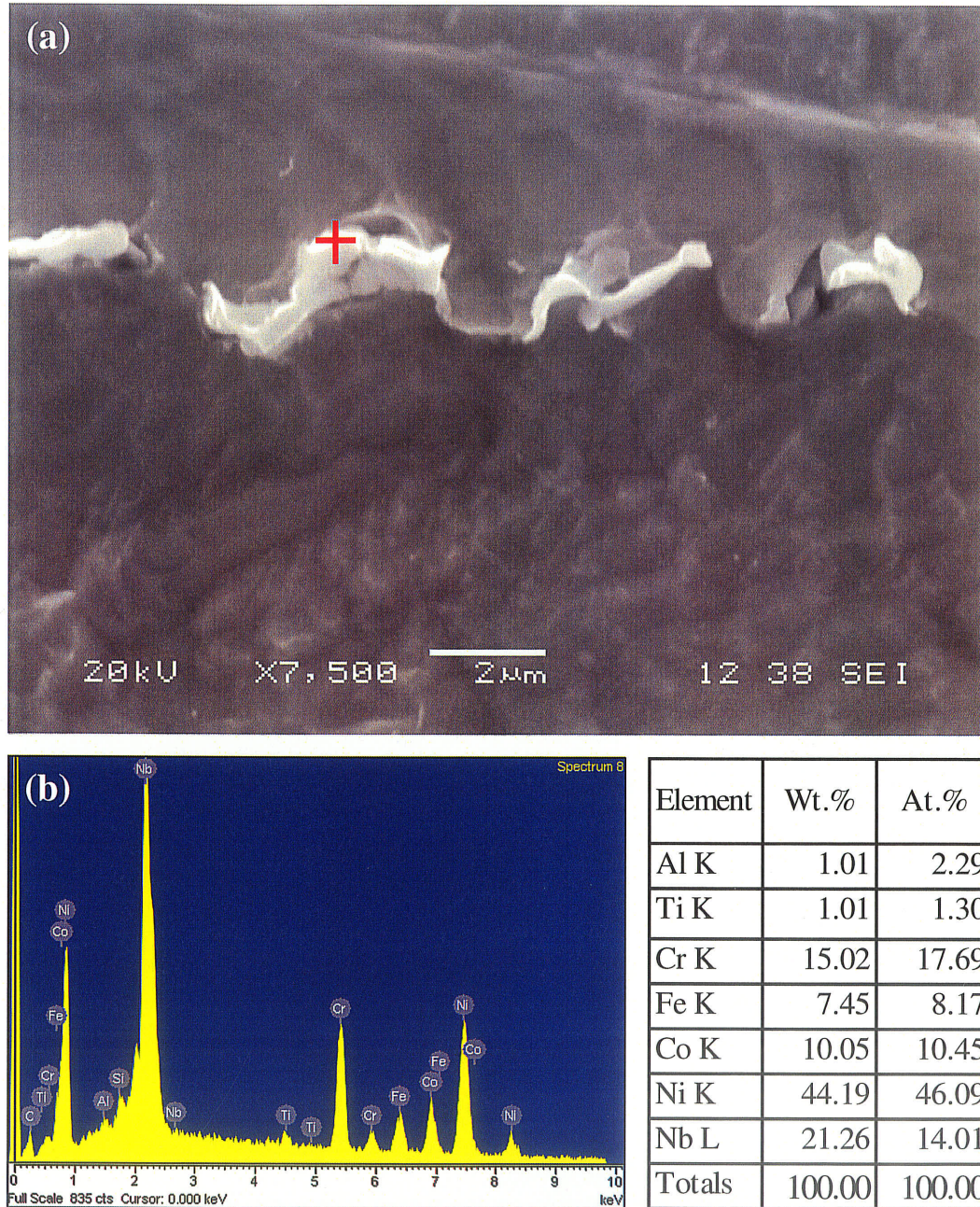
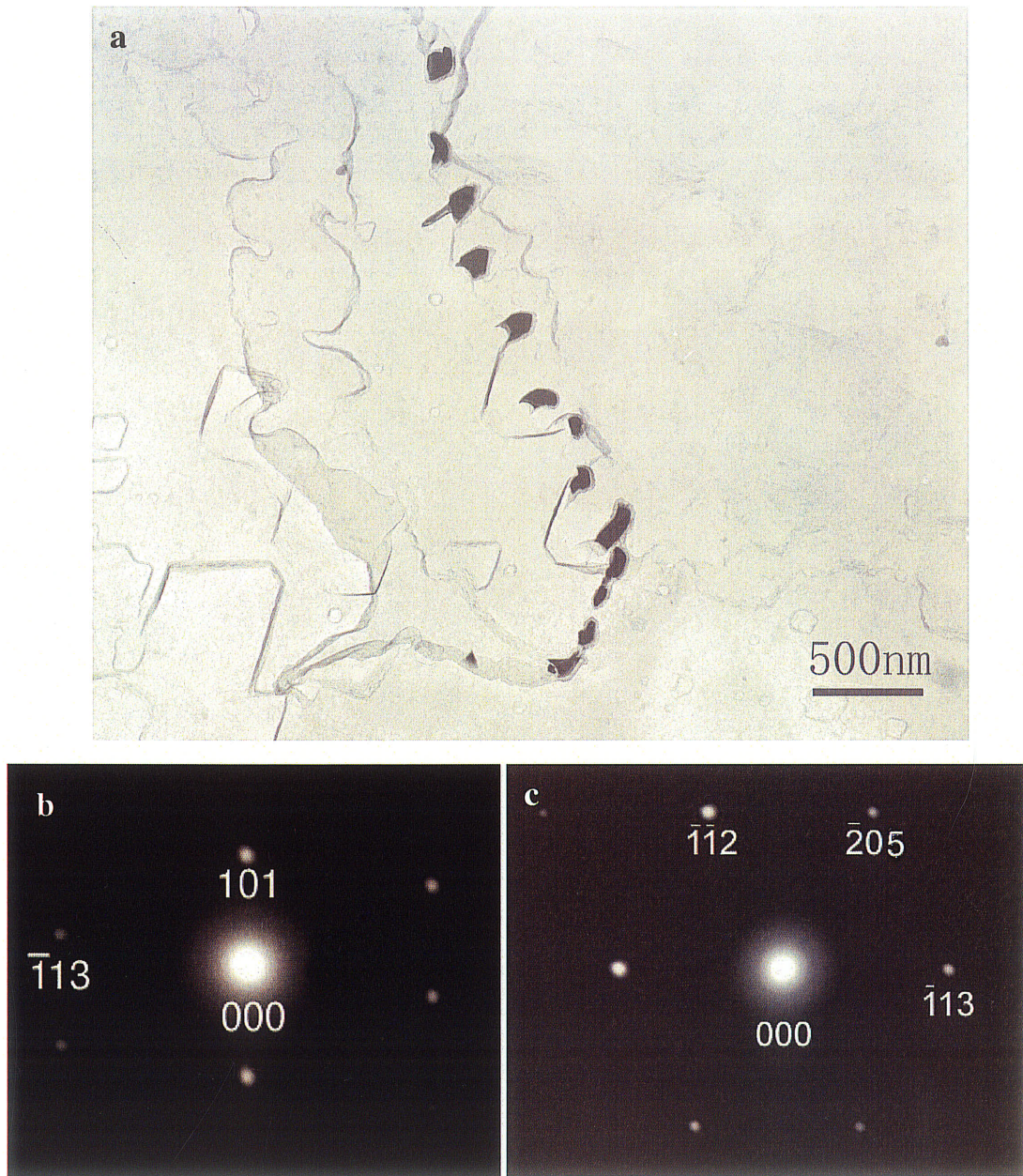
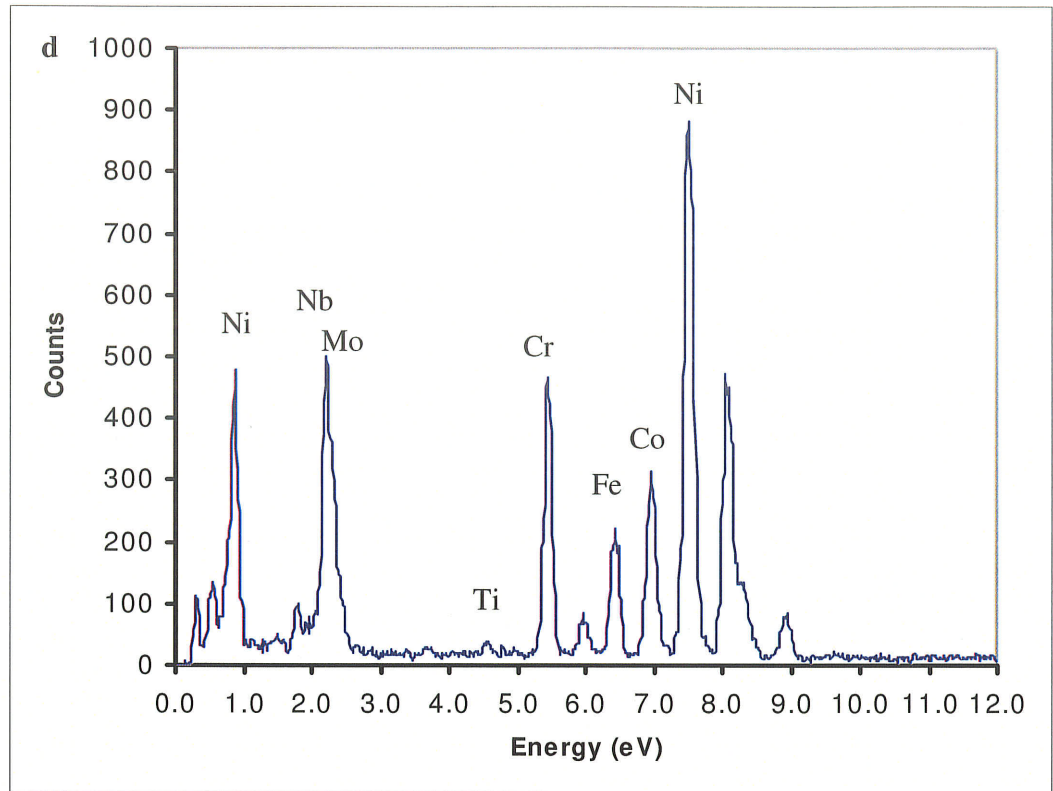


Fig.4-10. SEM micrograph (a) showing the resolidified products on a grain boundary in HAZ, EDS analysis (b) demonstrated the resolidified products rich in Nb.



Figs.4-11. TEM micrograph showing Laves phase in HAZ extracted on carbon replica (a) morphology along GB, (b) and (c) diffraction patterns from zone axes of $[14\bar{1}]$ and $[\bar{5}1\bar{2}]$ respectively, (d) EDS



Element	Wt %	At %
Ti K	0.50	0.70
Cr K	11.60	15.50
Fe K	6.40	7.90
Co K	8.80	10.40
Ni K	25.70	30.50
Nb K	35.80	26.90
Mo K	11.30	8.20
Total	100.00	100.00

Figs.4-11. TEM micrograph showing Laves phase in HAZ extracted on carbon replica (a) morphology along GB, (b) and (c) diffraction patterns from zone axes of $[14\bar{1}]$ and $[\bar{5}1\bar{2}]$ respectively, (d) EDS

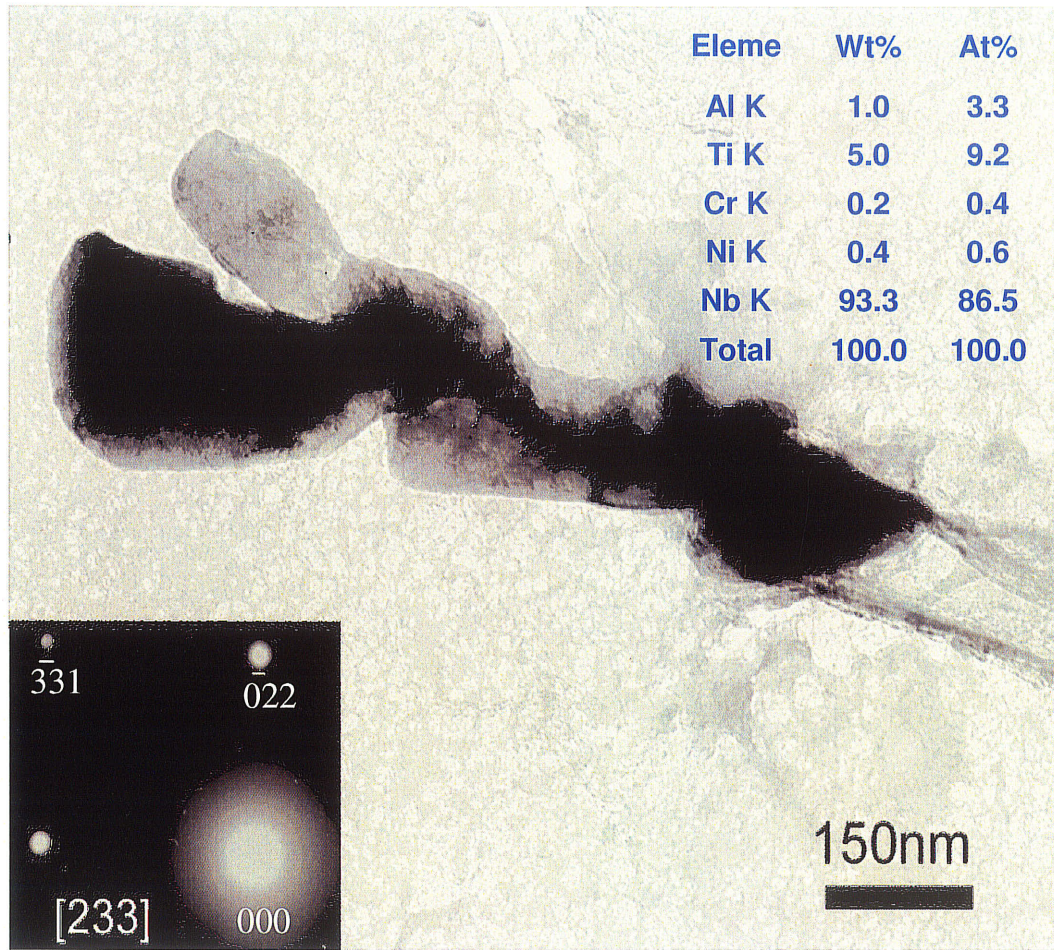


Fig.4-12. TEM micrograph showing the morphology of carbides in HAZ extracted on carbon replica with indexed diffraction pattern and compositions from EDS.

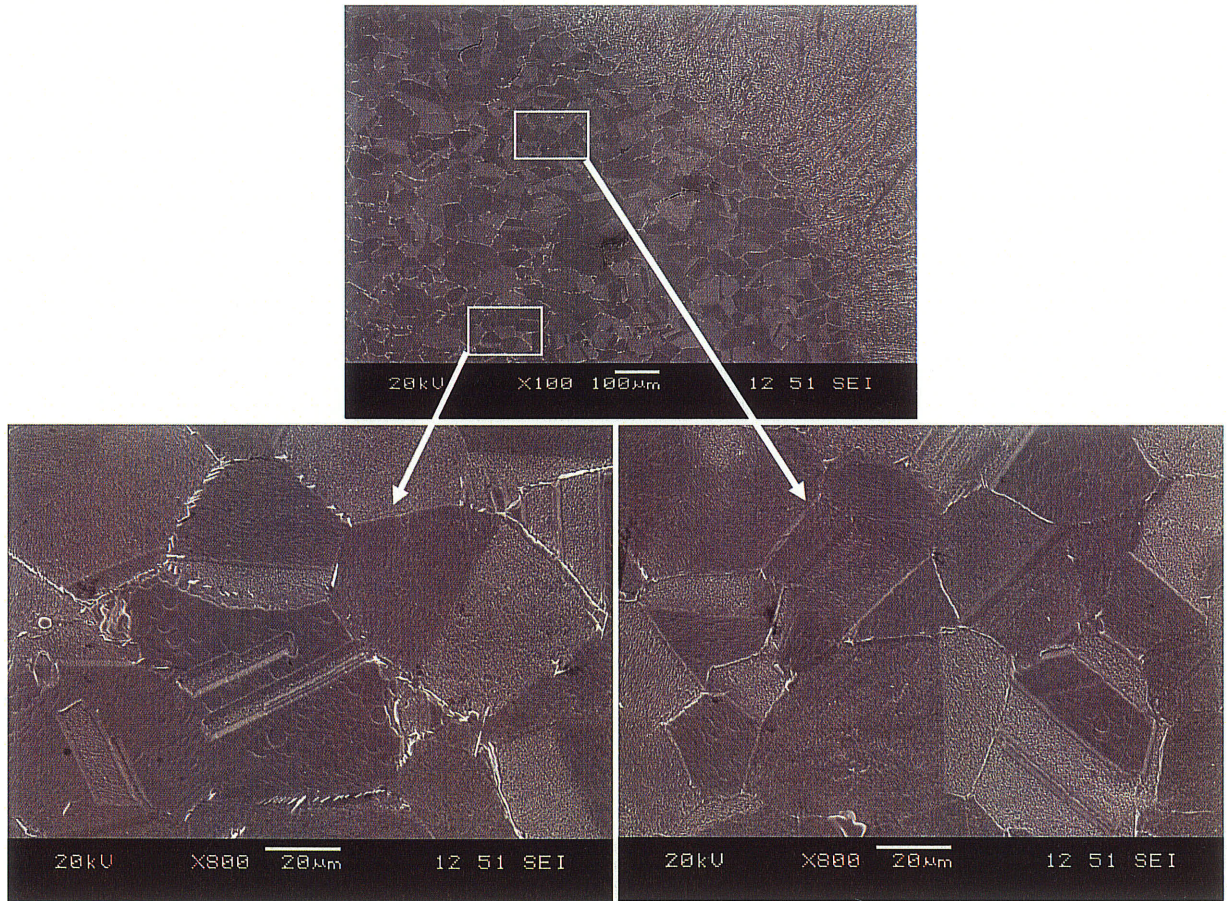
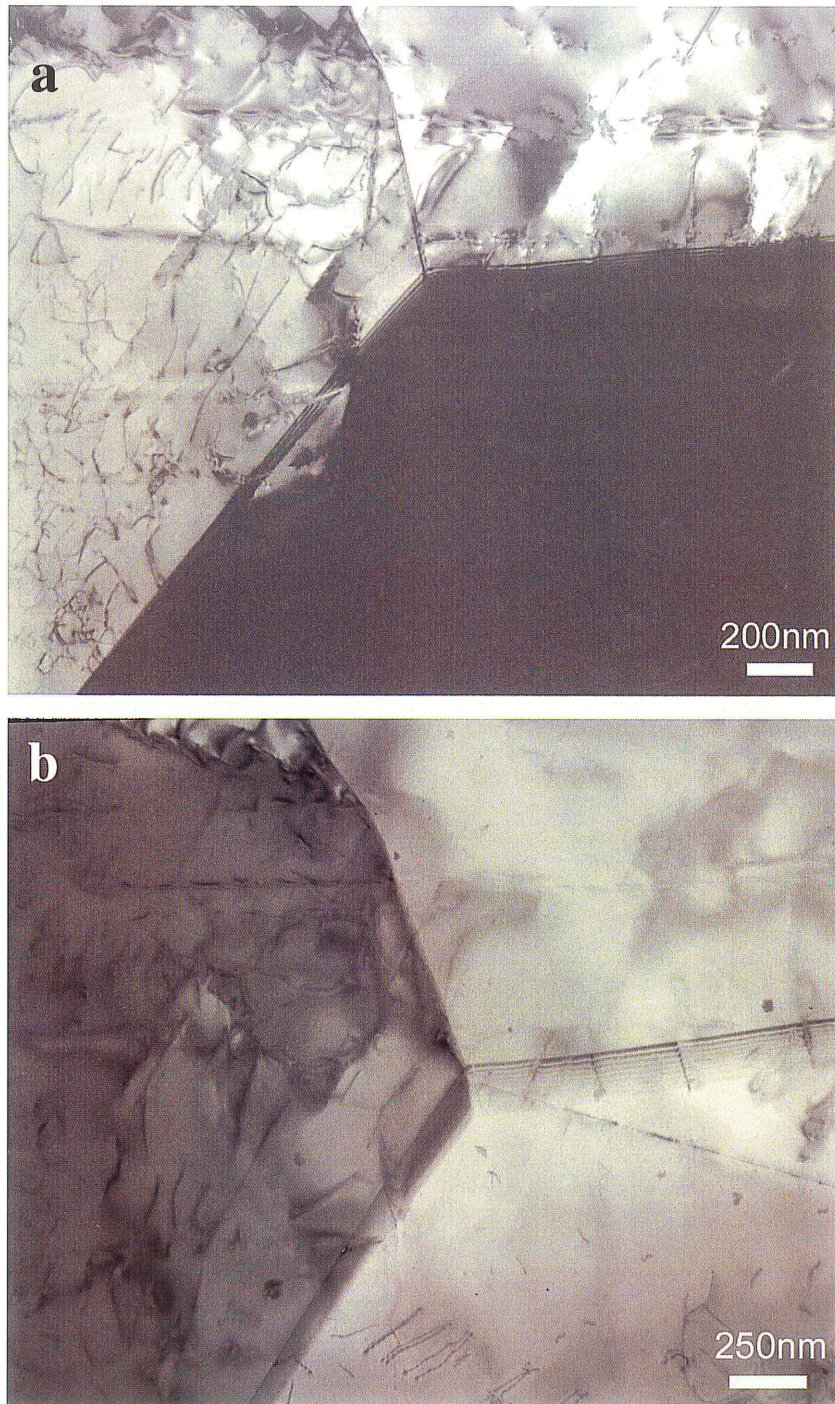


Fig.4-13. SEM micrographs showing the delta phase dissolution in the region close to fusion line in HAZ.



Figs.4-14. TEM micrographs showing the triple GB without delta phase in HAZ (a) and (b) taken in different directions and the relative rotation angle between (a) and (b) is about 15° .

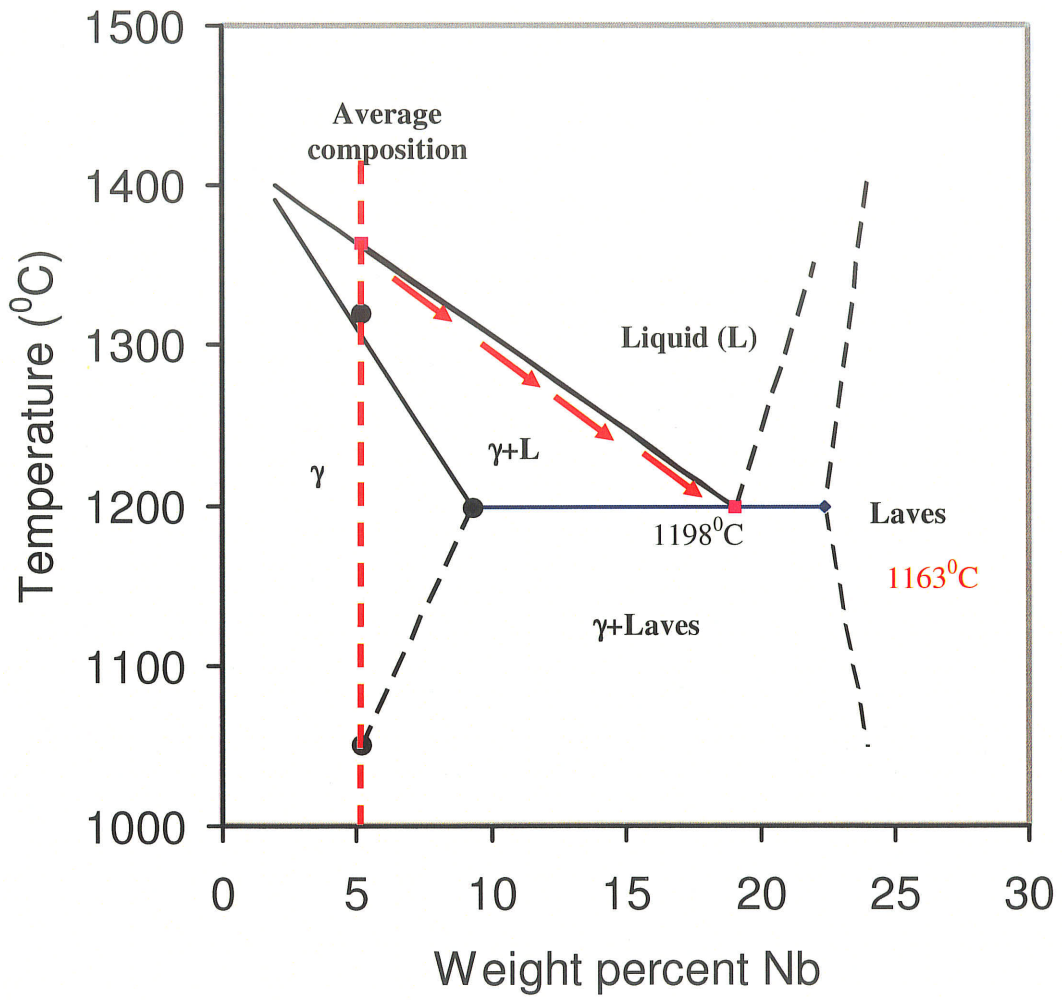


Fig.4-15. Solidification constitution diagram for Inconel 718 from ref.[43].

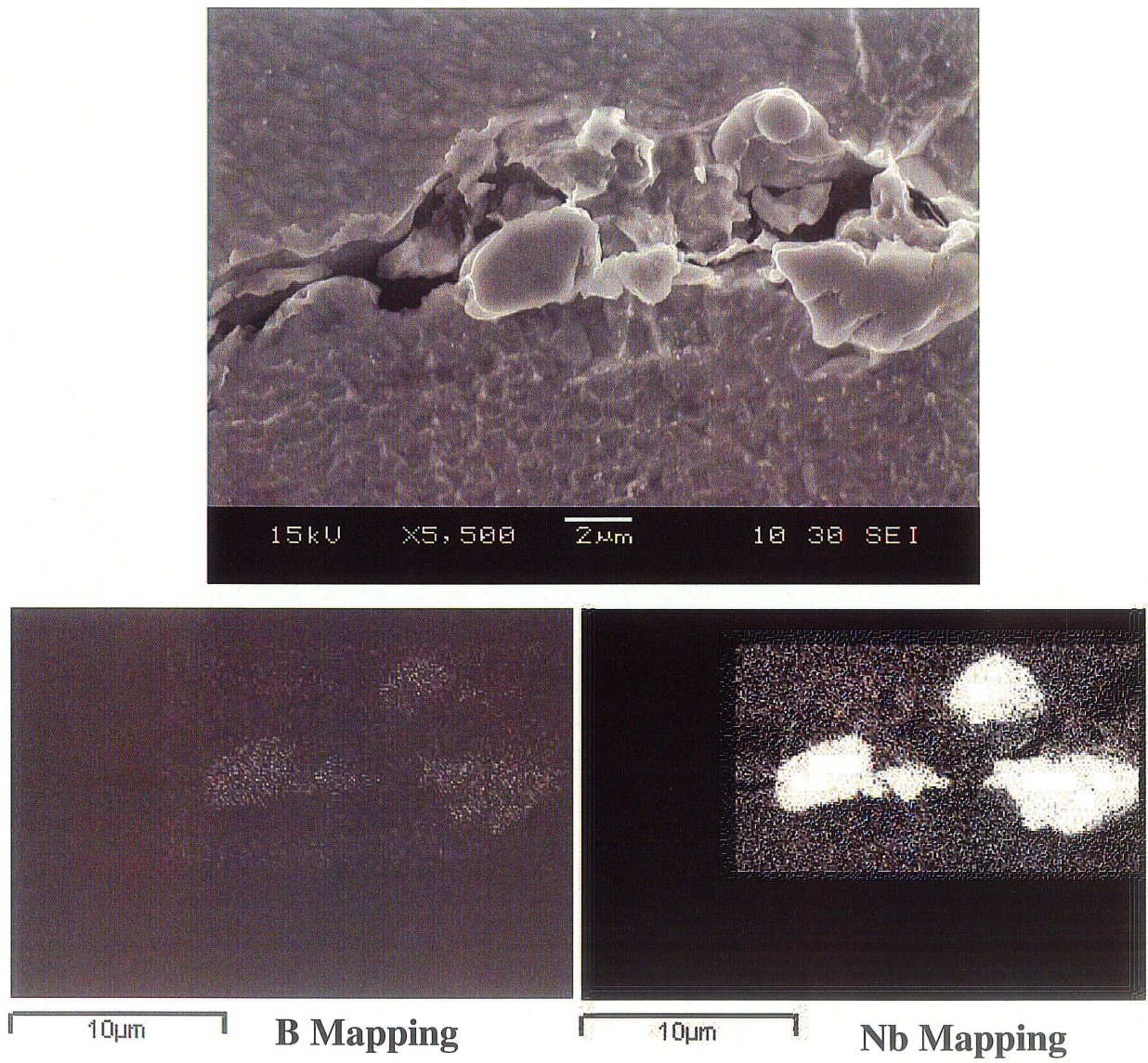
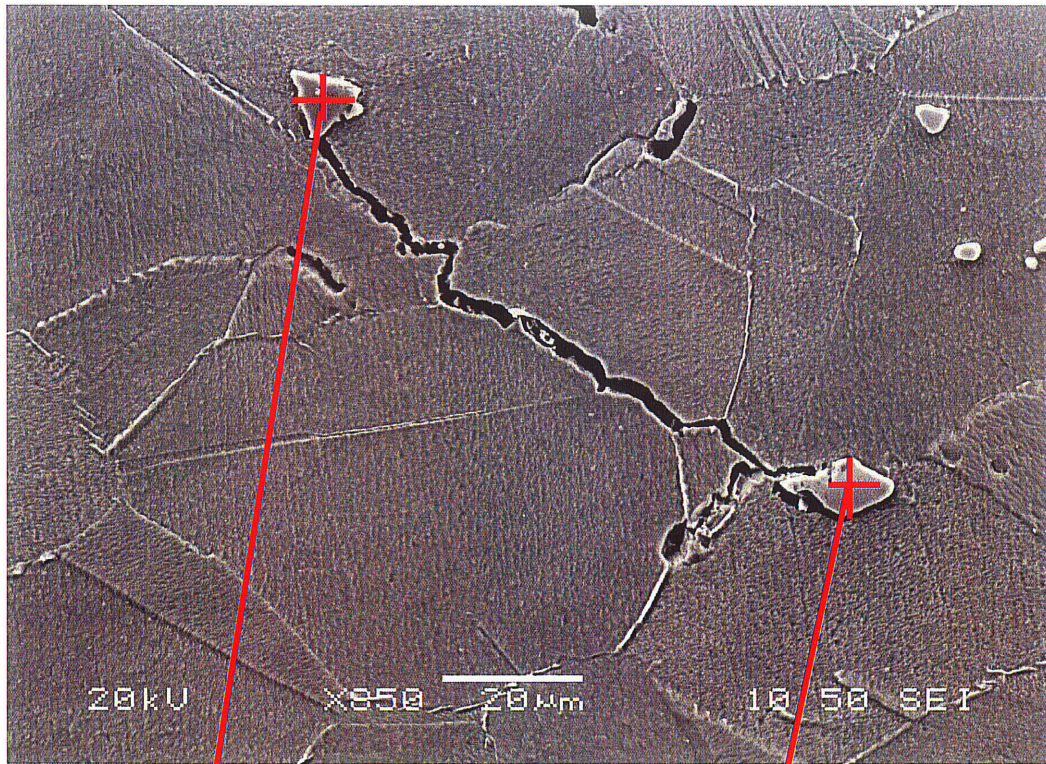


Fig.4-16. X-ray mapping revealing cracking occurred along B/Nb rich particles



Element	Wt%	At%
Ti K	63.42	74.14
Cr K	2.75	2.96
Fe K	0.99	0.99
Co K	1.06	1.00
Ni K	4.97	4.74
Nb L	26.81	16.16
Totals	100.00	100.00

Element	Wt %	At %
Ti K	7.94	14.21
Ni K	1.84	2.69
Nb K	90.22	83.10
Total	100.00	100.00

Fig.4-17. SEM micrograph shows a crack connected with two particles, EDS analysis showing one particle being rich in Nb, the being rich in Ti

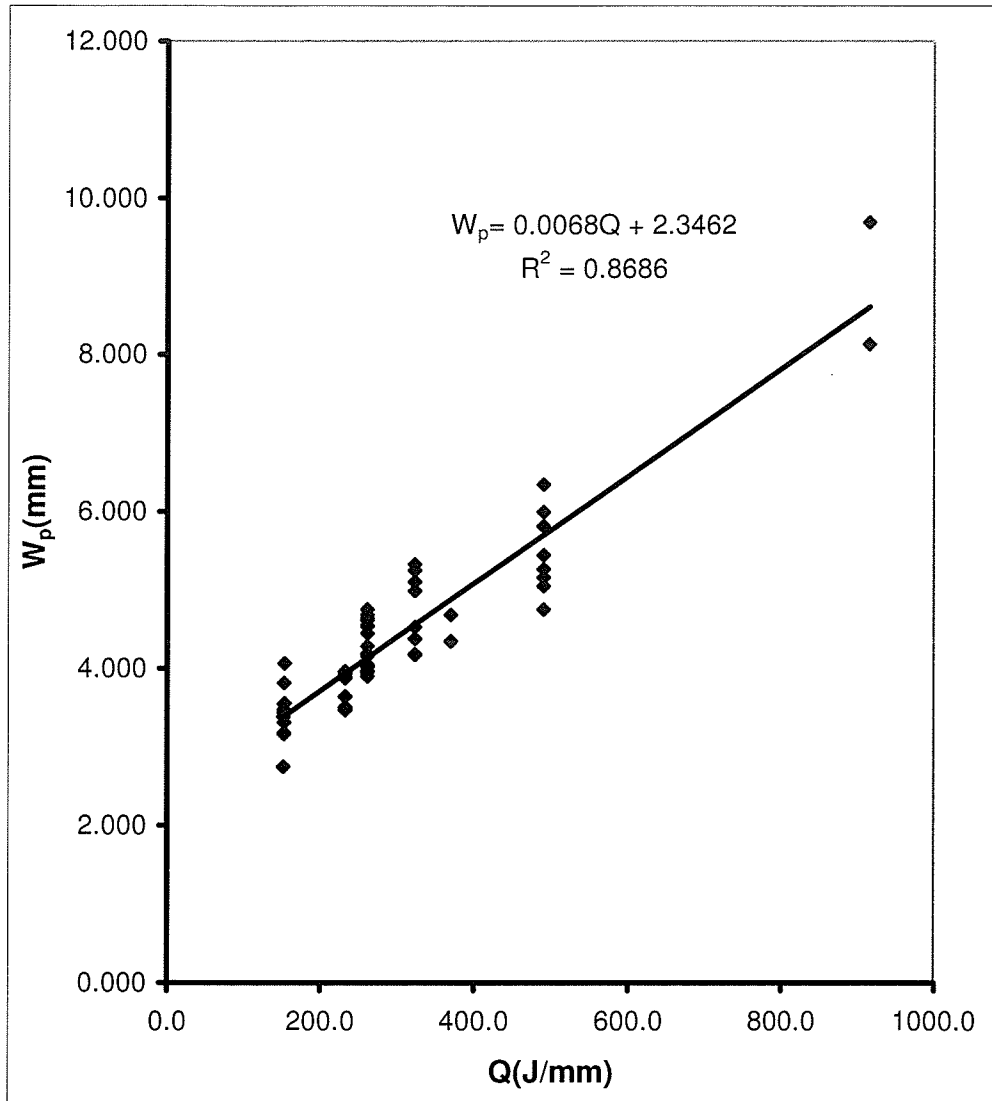


Fig.4-18. The top width of weld increases linearly with an increase of heat input rate (Q) in EB welding process.

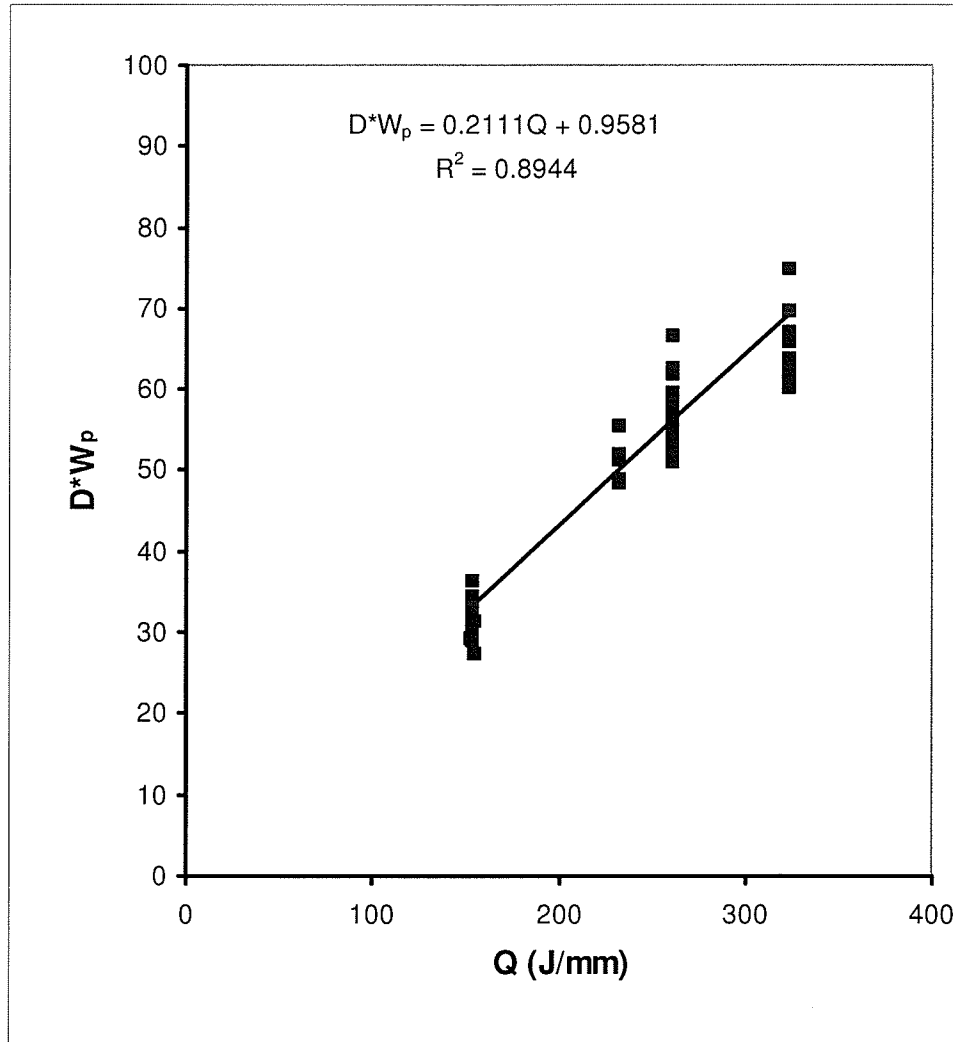


Fig.4-19. The product of top width time depth of welds linearly increasing with heat input rate.

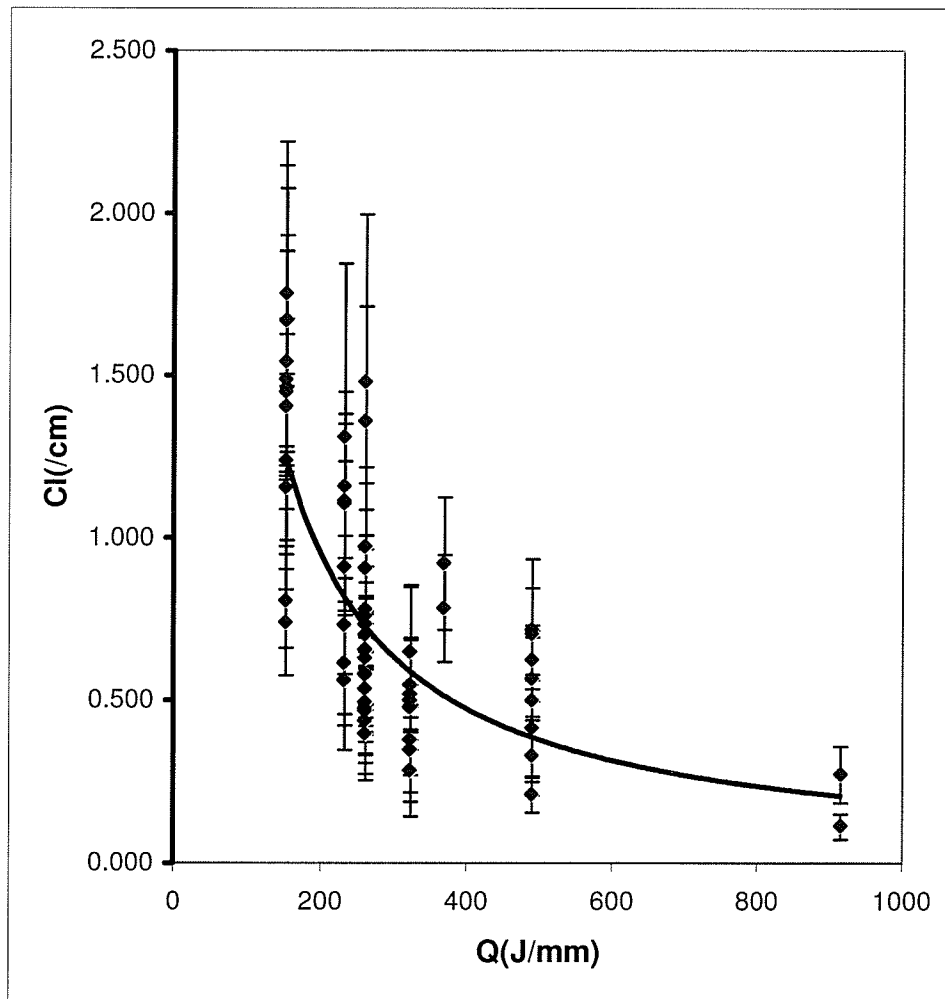
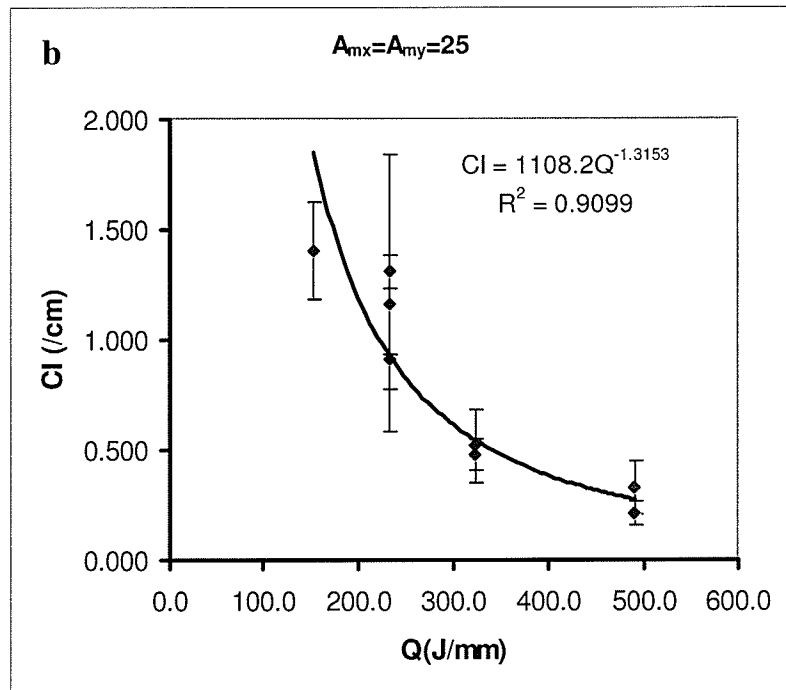
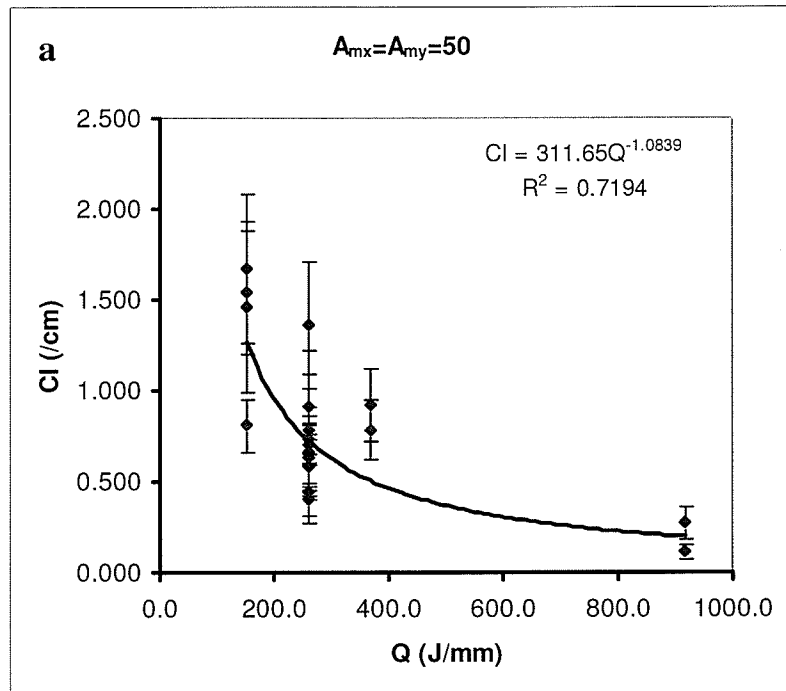
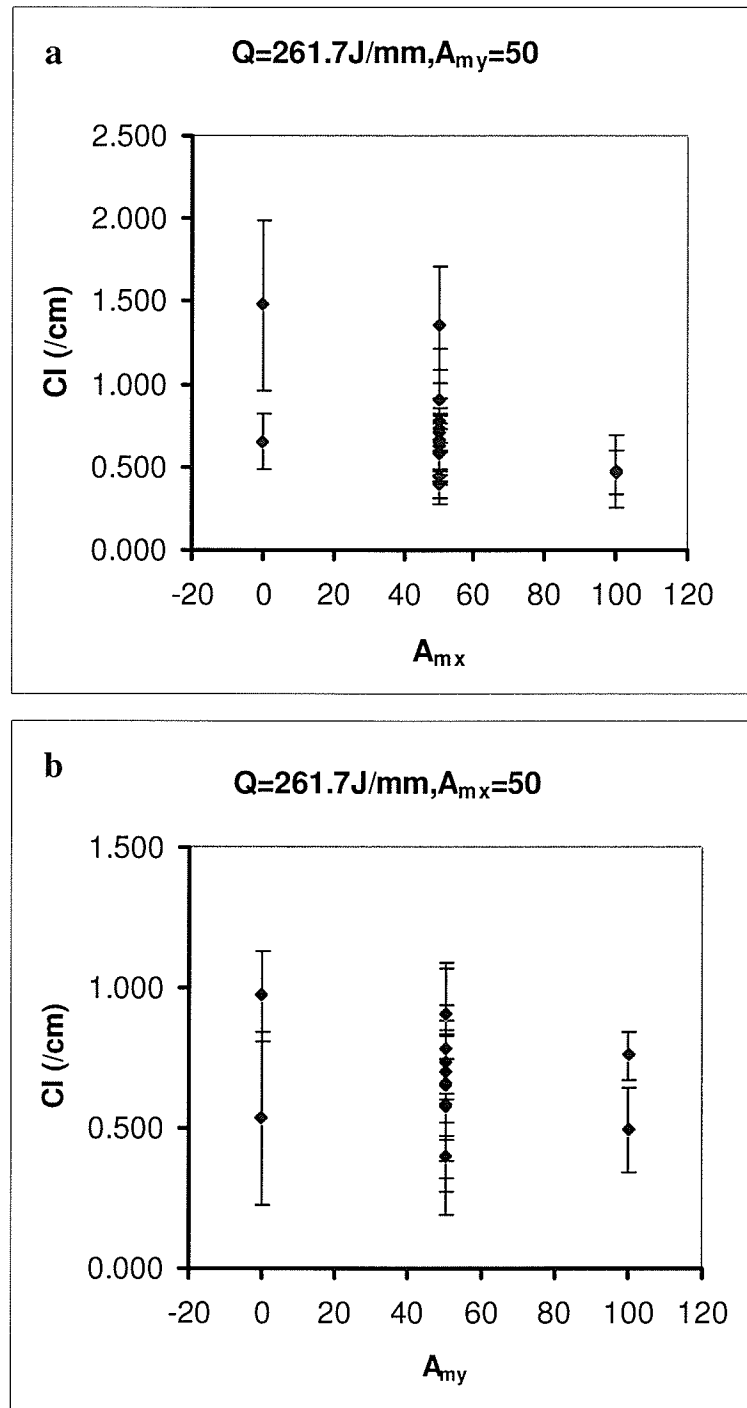


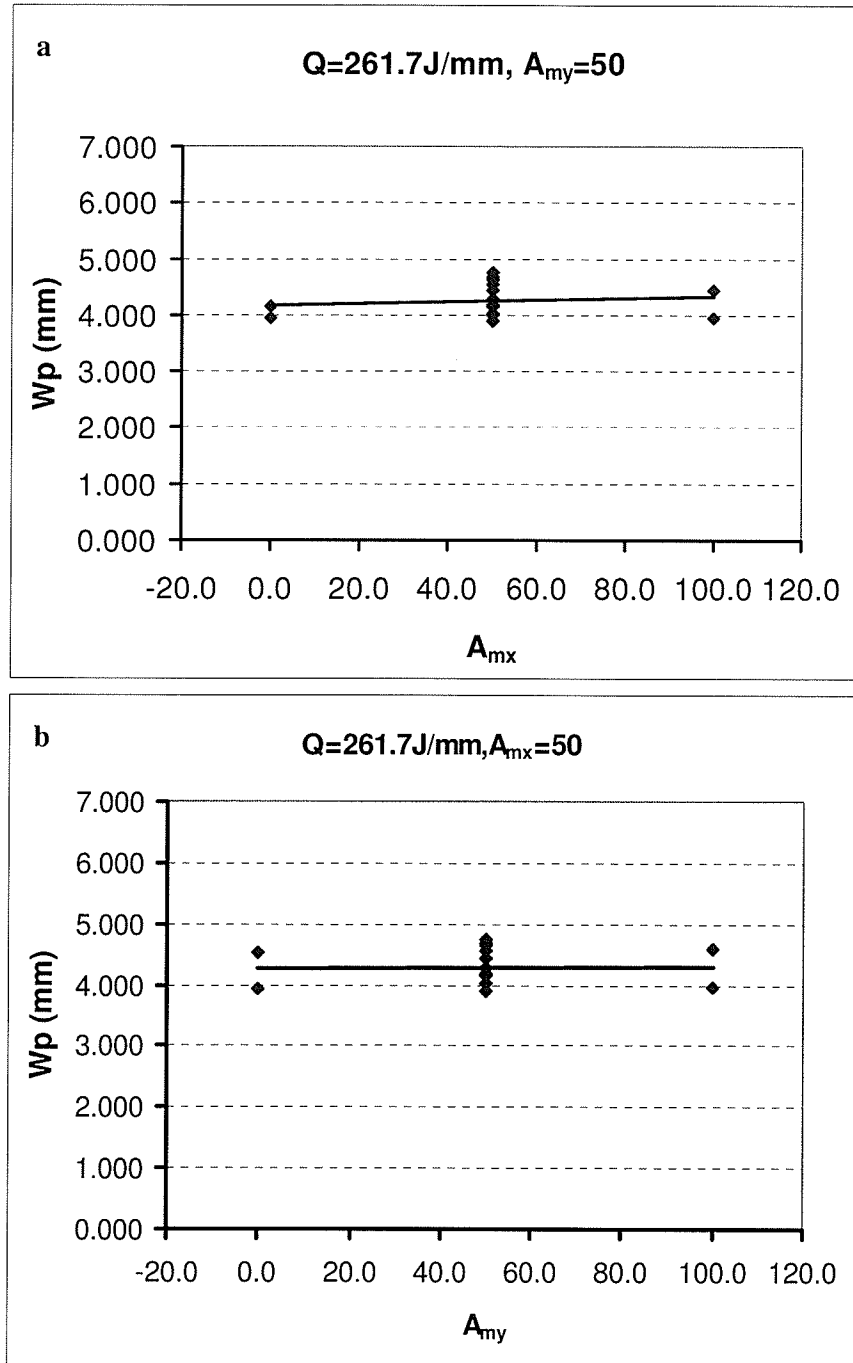
Fig.4-20 The crack index (CI) decreasing rapidly with an increase in heat input rate (Q) in EB welding process.



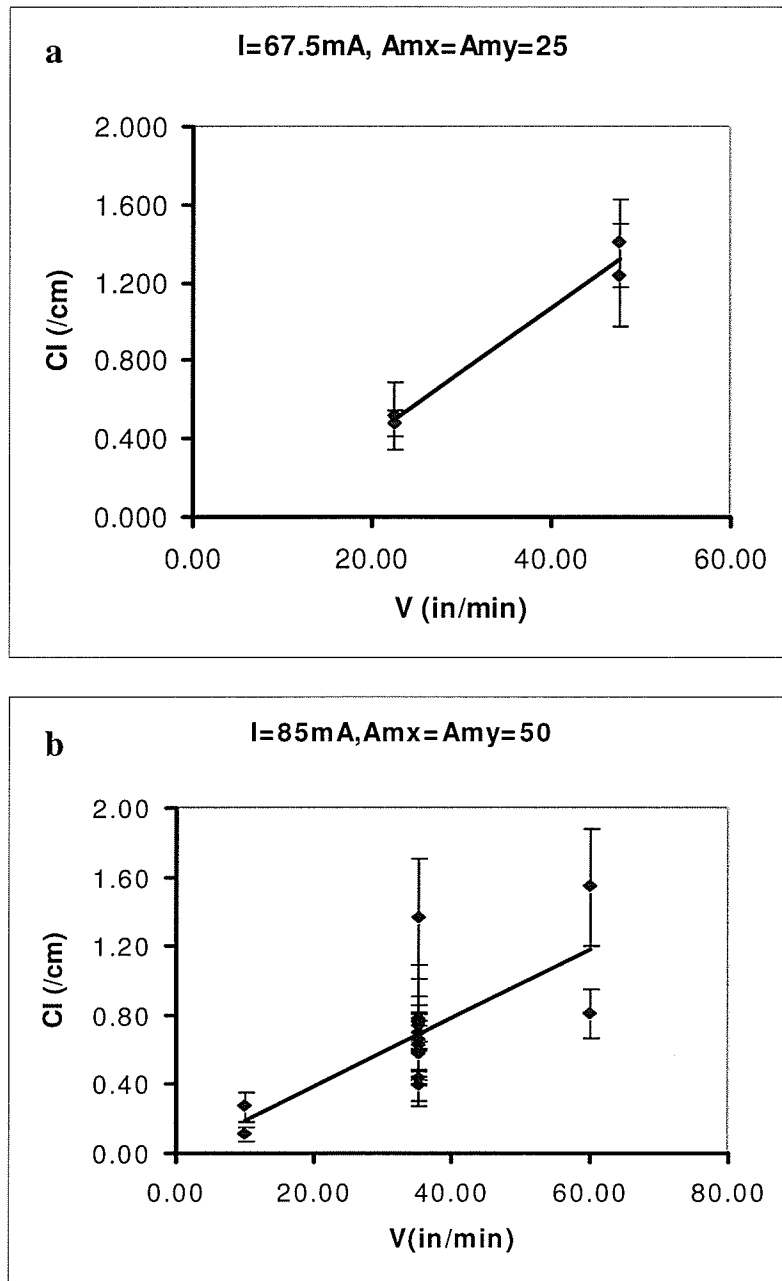
Figs.4-21. The CI decreasing rapidly with an increase in heat input rate when the oscillations were kept constant (a) $A_{mx}=A_{my}=50$,(b) $A_{mx}=A_{my}=25$.



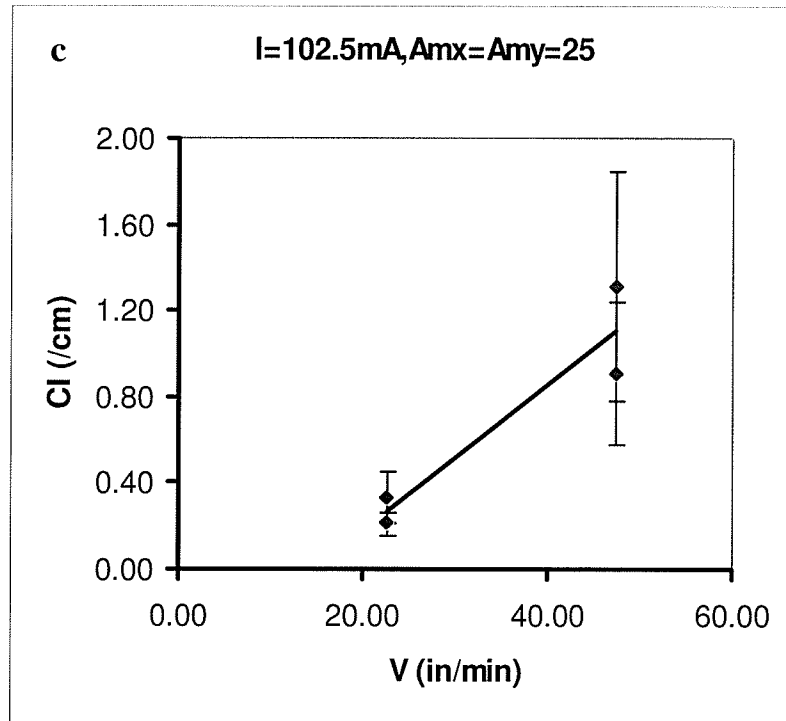
Figs.4-22. The relation between the CI and the oscillation score factor along tow directions when the other parameters are unchangeable (a) CI vs A_{mx} , (b) CI vs A_{my} .



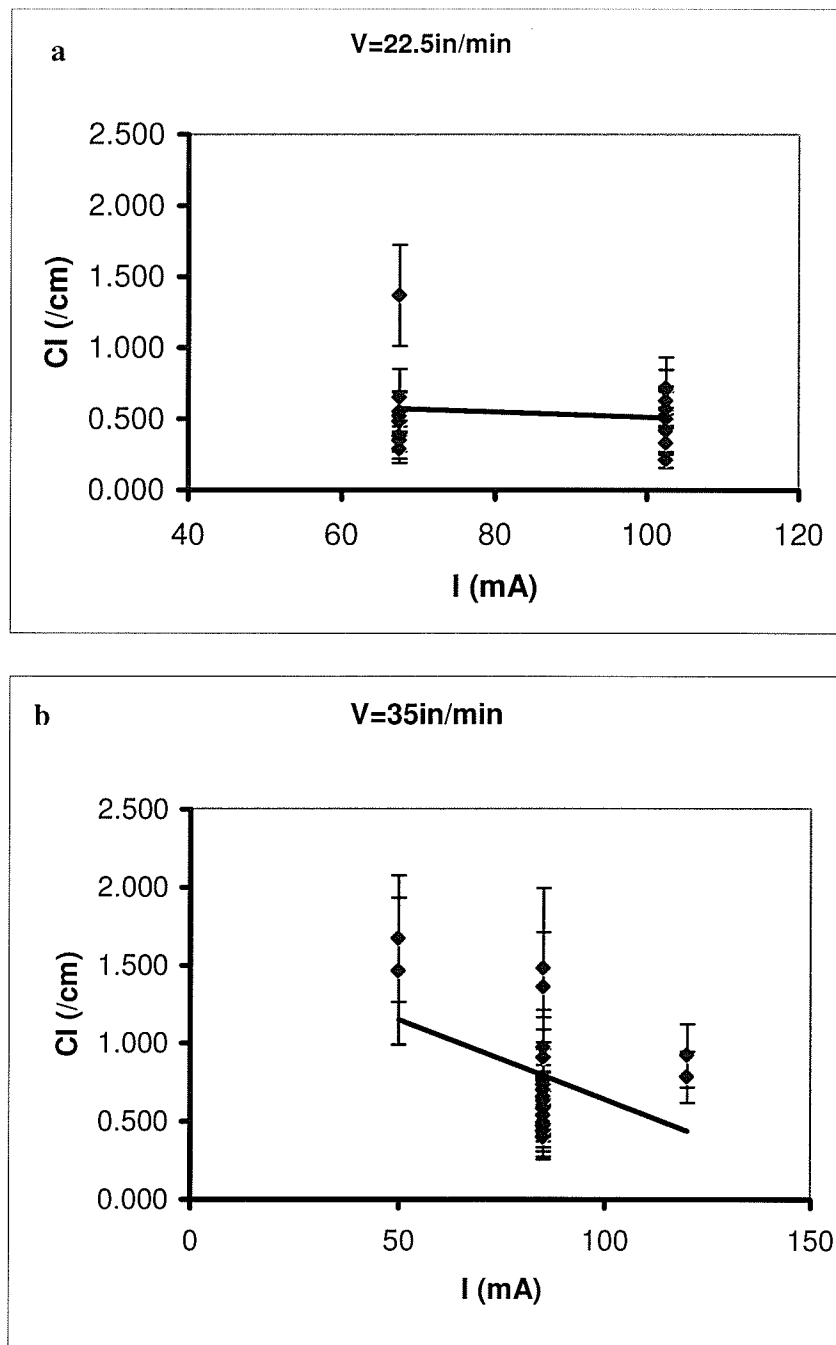
Figs.4-23. The top width of weld is not changed with the variation of oscillation score factor when the heat input rate is 261.7 J/mm (a) the oscillation score factor along the cross direction is a constant of 50, (b) the oscillation score factor along the longitudinal direction is a constant of 50.



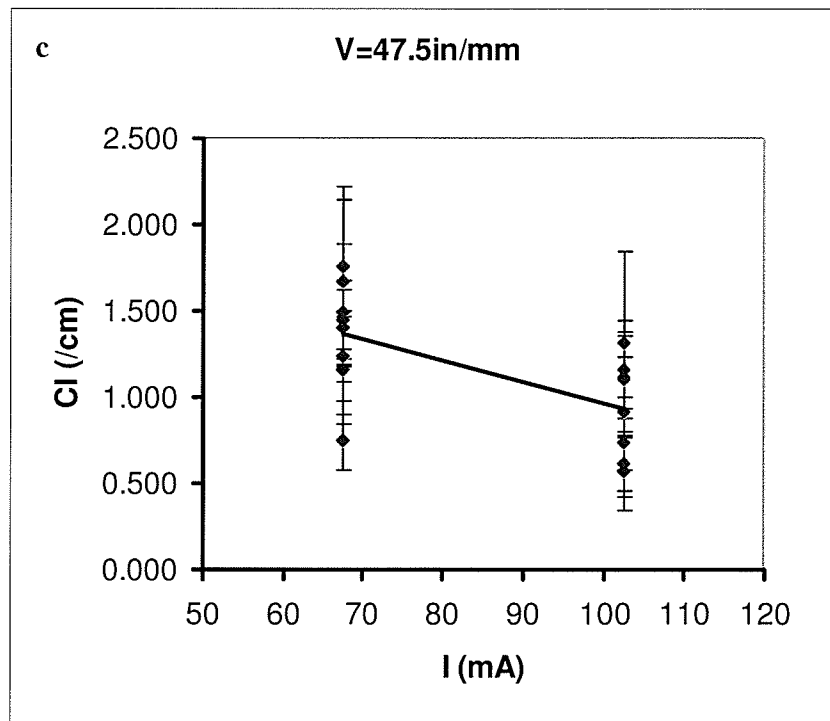
Figs.4-24. Diagrams showing the CI increasing with EB welding velocity when the other three parameters are kept at the constant, (a) beam current is 67.5mA, $A_{mx}=A_{my}=25$,(b) beam current is 85mA, $A_{mx}=A_{my}=50$,(c) beam current is 102.5mA, $A_{mx}=A_{my}=25$.



Figs.4-24. Diagrams showing the CI increasing with EB welding velocity when the other three parameters are kept at the constant, (a) beam current is 67.5mA, $A_{mx}=A_{my}=25$,(b) beam current is 85mA, $A_{mx}=A_{my}=50$,(c) beam current is 102.5mA, $A_{mx}=A_{my}=25$.



Figs.4-25. Diagrams showing the CI decreasing slightly with an increase of beam current when the welding velocity is unchangeable, (a) welding velocity is 22.5in/min. (b) welding velocity is 35in/min. (c) welding velocity is 47.5in/min.



Figs.4-25. Diagrams showing the CI decreasing slightly with an increase of beam current when the welding velocity is unchangeable, (a) welding velocity is 22.5in/min. (b) welding velocity is 35in/min. (c) welding velocity is 47.5in/min.

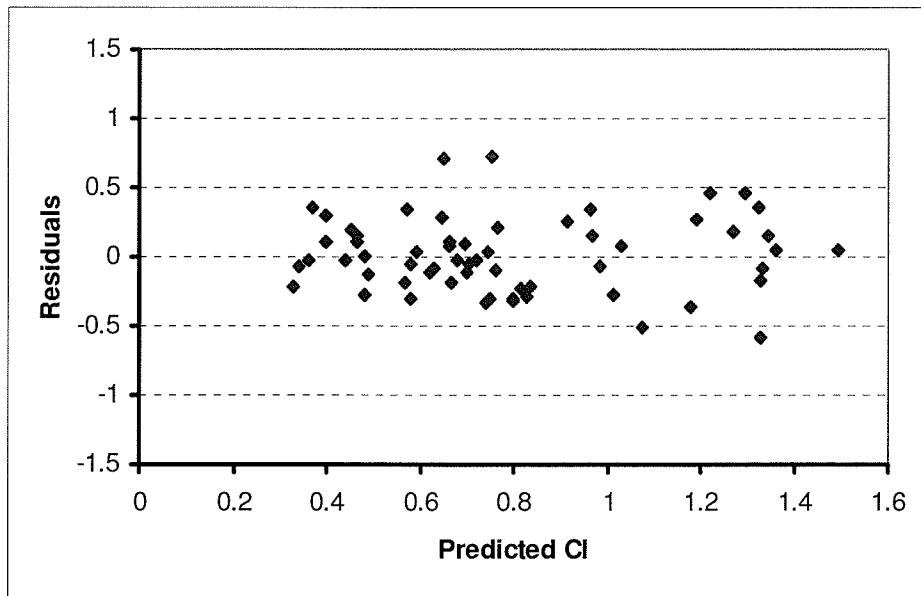


Fig.4-26. The plot of residual versus predicted CI

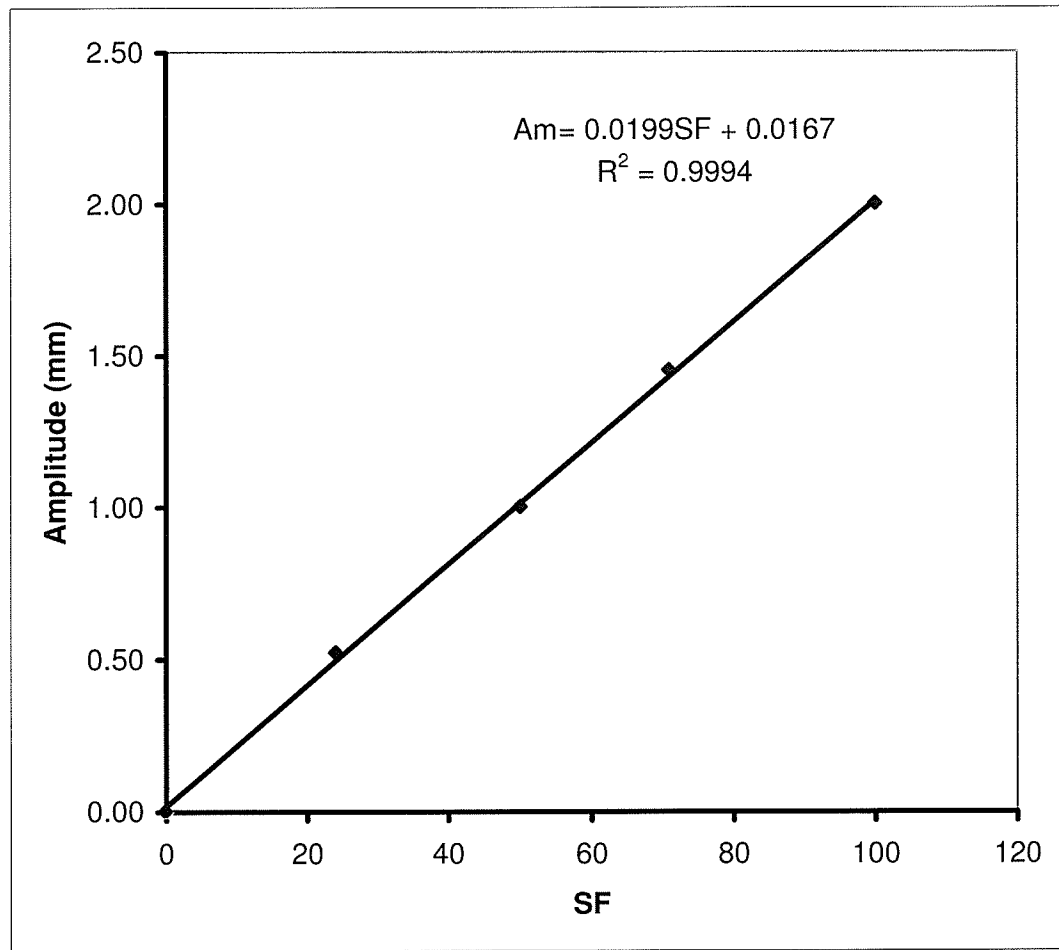
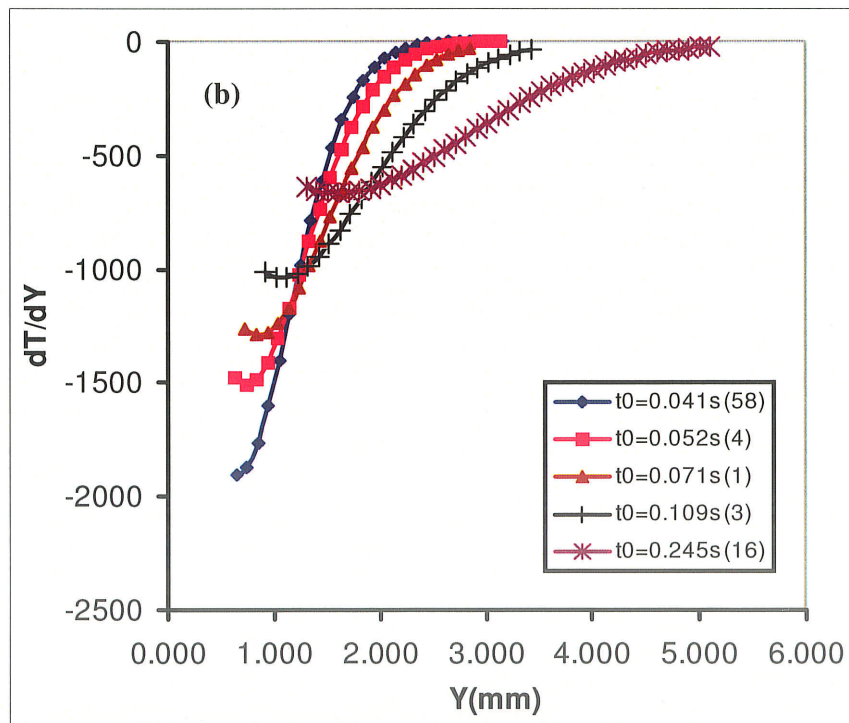
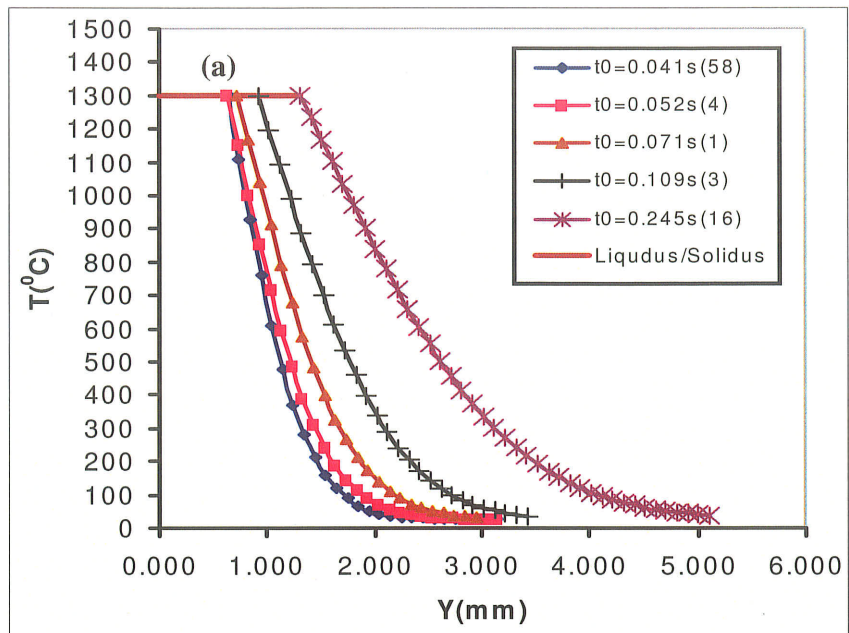


Fig.4-27. Electron beam oscillation amplitude vs score factor [68]



Figs.4-28. (a) Computed temperature distribution in HAZ at the neck of welds obtained in different welding velocities, (b) computed temperature gradient changes with respect to the distance from the fusion line.

Chapter 5

Conclusions

In the present study, the effect of electron-beam welding parameters on the heat-affected-zone cracking in AllVac 718Plus alloy, which was solution-heated at 950°C/1h+ water quenching, was investigated through sixty groups of welding parameters varied in beam current (I), welding velocity (V) and oscillation amplitudes in longitudinal and cross directions (A_{mx} and A_{my}). The average total crack length in HAZ in eight cross sections of a weld and the HAZ area were measured by means of an optical microscope equipped with image analysis system at a magnification of 500. The crack index (CI, i.e. total crack length per unit HAZ area) was used to evaluate the HAZ cracking trend of this alloy. The contributions of welding parameters to crack index were statistically analyzed. Microstructures in the base metal, and the HAZ of welds were examined by an analysis Scanning Electron

Microscope (SEM) and Transmission Electron Microscope (TEM) equipped with Energy-Dispersive-Spectroscopy (EDS). On the basis of an ideal plane heat source model, the temperature and its gradient distributions with respect to distance from fusion line were estimated. The following conclusions were obtained:

- 1) The microstructure of the base metal consists of γ phase, small γ' phase homogeneously distributed in the matrix, and δ phase around random grain boundaries, as well as several second phases such as carbides/borides.
- 2) Total crack length on each cross section and the average total crack length in eight cross sections as well as crack index varied with electron beam welding parameters, which were listed in Table 4-2.
- 3) The top width of welds increased linearly with heat input rate (Q), and crack index decreased rapidly with heat input rate. The smallest crack index (0.113, i.e. run16, $V=10\text{in}/\text{min}$, $I=85\text{mA}$) was related to the greatest heat input rate ($Q=916\text{J}/\text{mm}$). Statistical analysis results also showed the crack index significantly increased with welding velocity, and decreased with the electron beam current.
- 4) Some cracks were accompanied with re-solidified products that are rich in Nb. The observed morphology and the EDS analysis suggested that they were γ/Laves or γ/NbC eutectic structure. The observation and analysis in TEM showed further that re-solidified products within grain boundaries in the HAZ were Laves phase, which was formed due to grain boundary liquation.
- 5) In HAZ of welds, dissolution of δ phase around grain boundaries close to fusion line occurred during electron beam welding, which promoted grain boundary liquation.

- 6) The present microstructural observation indicated that there existed some cracks without accompanying with re-solidified products. The particles rich in boron were also found on some crack edges by mean of X-ray mapping technique in the SEM.
- 7) The HAZ cracking of this alloy during electron beam welding was mainly attributed to the grain boundary liquation and the segregation of detrimental elements such as boron.
- 8) On the basis of a plane heat source model, the temperature and temperature gradient in HAZ were calculated. The calculation showed that the temperature gradient increased with welding velocity. Combined with the measured total crack length, it would be known that the higher is the welding velocity, the steeper is the temperature gradient and the greater is CI.

Chapter 6

Future Work

Base on achievement in the present study, the following future works are suggested.

1. The present study shows that heat input rate plays a role in the HAZ cracking of this alloy, and the minimum crack index (CI) was obtained at the maximum heat input rate, thus, the HAZ cracking may be eliminated if the heat input rate is further increased. It is very important to study the effect of heat input rate on the HAZ cracking in high range of heat input rate.
2. The HAZ cracking seems more susceptible to the electron beam welding velocity than the other welding parameters. It is significant to investigate systematically the effect of electron beam welding velocity on the HAZ cracking of this alloy when fixing other electron welding parameters.

3. The trace elements distribution on grain boundaries should be examined by means of Secondary Ion Mass Spectroscopy (SIMS) technique, in order to ensure the mechanism of decreasing grain boundary strength (or ductility).
4. The accurate evaluation of transient temperature and its gradient across HAZ in three dimensions during electron beam welding is needed to do, because the liquation of grain boundary and the cracking are directly involved with the local temperature and the stress/strain.

References

- 1) Wei, D. C and Kennedy, R., Role of chemistry in 718-type alloys- Allvac[®] 718Plus[™] alloy development, Superalloys 2004, ed. Green, K. A. et al., pp90-99. (Proceedings of the 10th International Symposium on Superalloys, Sept. 19-23, 2004, Champion, Pennsylvania, USA..
- 2) Thompson, R.G. Dobbs, J.R., Mayo, D.E., The Effect of Heat Treatment on Microfissuring in Alloy 718, Weld. J. Vol. 65 (11), 1986, p. 299s-304s.
- 3) Thompson, R.G. Microstructure microfissuring of alloy 718 in the weld heat-affected zone, J. Metals. Vol.40 (7), 1988, p44-48.
- 4) Richards, N L, Huang, X. and Chaturvedi, M C, Heat affected zone cracking in cast Inconel 718, Material Characterization, Vol. 28,1992,p.179-187.
- 5) Chaturvedi, M C; Chen, W; Saranchuck, A; Richards, N L., The effect of B segregation on heat-affected zone microfissuring in EB welded Inconel 718, Superalloys 718, 625, 706 and Various Derivatives; Pittsburgh, Pennsylvania; USA; 1997. p. 743-751.
- 6) Chen, W., Chaturvedi, M.C., Richards, N.L. and McMahon,G., Grain boundary segregation of boron in Inconel 718, Metall. Mater. Trans. Vol. 29A (7), 1998, p.1947-1954.
- 7) Guo, H, Chaturvedi, M.C., Richards, N.L., and McMahon,G. S., Interdependence of character of grain boundaries, intergranular segregation of boron and grain boundary liquation in simulated weld heat-affected zone in Inconel 718, Scr. Mater. Vol. 40 (3), 1999, p.383-388.

- 8) Guo, H, Chaturvedi, M.C. and Richards, N.L., Effect of boron concentration and grain size on weld heat affected zone microfissuring in Inconel 718 base superalloys, *Science and Technology of Welding and Joining*. Vol. 4(4), 1999, p. 257-264.
- 9) Guo, H., Chaturvedi, M.C. and Richards, N.L., Effect of sulphur on hot ductility and heat affected zone microfissuring in Inconel 718 welds, *Sci. Tech. Weld. Join.*, Vol. 5 (6), 2000, p378-384.
- 10) Richards, N.L. and Chaturvedi, M.C., Effect of minor elements on weldability of nickel base superalloys, *Inter. Mater. Reviews*. Vol. 45(3), 2000, pp. 109-129.
- 11) Chen, W., Chaturvedi, M.C. and Richards, N.L., Effect of boron segregation at grain boundaries on heat-affected zone cracking in wrought Inconel 718, *Metall. Mater. Trans.A*, Vol.32A (4), 2001, p.931-939.
- 12) Benhadad, S; Richards, N L; Chaturvedi, M C, The Influence of Minor Elements on the Weldability of an INCONEL718-Type Superalloy, *Metall. Mater. Trans.A.*, Vol.33A (7), 2002, p2005-2017.
- 13) Richards, N L, Nakkalil, R. and Chaturvedi, M C, The influence of electron-beam welding parameters on heat-affected-zone Microfissuring in Incoly 903, *Metall. Mater. Trans A*, vol.25A, 1994, p.1733-1745.
- 14) ASM Handbook, "Welding, Brazing and Soldering" Vol.6, ASM International the Materials Information Society, pp254-256.
- 15) Meleka,A.H., *Electron-beam welding: Principles and practice*, McGRAW-HILL Publishing Company Ltd. 1971, London, New York, Toronto, Sydney, Johannesburg, Mexico,Panama, Dusseldorf., pp2-4.
- 16) Birnie, J.V., An introduction to electron beam welding, *Physics in Technology* Vol.7, 1976, p116-122.
- 17) Easterling, K. *Introduction to the Physical Metallurgy of Welding*, butterworth-Heinemann Ltd, Oxford, 1992, pp126.

- 18) Cho, L. T. and Chin, M. T. Heat flow in fusion welding, ASM Handbook, "Welding, Brazing and Soldering" Vol.6, ASM International The Materials Information Society, pp7-18.
- 19) Passoja,D.E. "Heat Flow in Electron Beam Welds ",welding research supplement, 1966, p379-s--384-s.
- 20) Binda,B. Capello,E. and Previtali,B. A semi-empirical model of the temperature field in the AISI 304 laser welding, J. Mater. Tech.Vol.155-156, 2004,p1235-1241.
- 21) Pavelic, V, Tanbakuchi,R, Uyehara,O.A, and Myers,P.S. Experimental and computed temperature histories in cast tungsten-arc welding of thin plates, welding Research Supplement, Vol.43 p. 295S-305S.
- 22) Friedman, E; Gickstein, S.S., Investigation of the Thermal Response of Stationary Gas W Arc Welds Weld. J. Vol. 55, no. 12, 1976, pp. 408s-420s.
- 23) Feng, Z; Zacharia, T; David, S A, Thermal stress development in a nickel based superalloy during weldability test , Welding Journal. Vol. 76, no. 11, 1997, p470s-483s.
- 24) Choi, J; Mazumder, J, Numerical and experimental analysis for solidification and residual stress in the GMAW process for AISI 304 stainless steel, Journal of Materials Science. Vol. 37, no. 10, 2002, p. 2143-2158.
- 25) Yang, Q X; Yao, M; Park, J, Numerical simulation on residual stress distribution of hard-face-welded steel specimens with martensite transformation, Materials Science and Engineering A. Vol. 364, no. 1-2, 2004, p. 244-248.

- 26) Ferro P., Zambon,A. and Bonollo,F., Investigation of electron-beam welding in wrought Inconel 706-experimentl and numerical analysis. *Material science and engineering*, A392, 2005,p94-105.
- 27) Zhu,X.K. and Chao,Y.J. Numerical simulation of transient temperature and residual stresses in friction stir welding of 304L stainless steel, *J. Mater. Processing Tech.* Vol.146, 2004,p263-272.
- 28) Feng, Z; Zhu, Y Y; Zacharia, T; Brand, P C; Fields, R J; Prask, H J;Blackburg, J, Modeling and validation of residual stress distribution in an HSLA-100 disk, *Trends in Welding Research. 4th International Conference; Gatlinburg, Tennessee; USA; 5-8 June 1995. pp. 105-110. 1996*
- 29) Yanjing, L. Juan, W. Maoai, C. and Xiaoqin, S. Finite element analysis of residual stress in the welded zone of high strength steel, *Bull. Mater. Sci.*, Vol. 27, No. 2, 2004, p. 127-132.
- 30) Bowles, C. Q., "Fracture and Structure" *ASM Handbook*, Vol.9, 1996, ASM International Materials Park OH, p 5-41.
- 31) Gross, T.S. "Micromechanisims of monotonic and cyclic crack growth", *ASM Handbook*, Vol.9, 1996, ASM International Materials Park OH, p42-60.
- 32) Pardoen,T. and Hutchinson, J.W., An extended model for void growth and coalescence, *J. Mech. Phys. Solids*, Vol.48, 2000, p2467-2512.
- 33) Shinozaki,K. *Welding and joining Fe and Ni-base superalloys*, *welding International* Vol.15(8), 2001,p593-610.
- 34) Argo,A.S. , Im,J. and Safoglu,R. cavity formation from inclusions in ductile fracture, *Metall. Trans A*, Vol.6A,1975,p825-837.

- 35) Hancock, J.W. and Thomson, R.D., Strain and stress concentrations in ductile fracture by void nucleation growth and coalescence, *Mater. Sci. Tech.*, Vol.1(9), 1985, p684-690.
- 36) Benson, D.J.; Fu, H.H. and Meyers, M.A. On the effect of *grain* size on yield *stress*: extension into nanocrystalline domain, *Materials Science and Engineering A*. Vol. 319-321, pp. 854-861. 2001.
- 37) Chaturvedi, M. C., Grain boundary, engineering and weldability of superalloys, ICAMMP-2002: International Conference on Advances in Materials Processing; Kharagpur, India; 1-3 Feb. 2002. p. 3-9.
- 38) A. Buchon, A. Menand and D. Blavette, Phase composition and grain-boundary segregation in a nickel base superalloy: A preliminary TEM-APFIM investigation. *Surface Sci.* Vol.246, 1991, pp. 218-224.
- 39) Richards, N.L. and Chaturvedi, M.C. Effect of minor elements on weldability of nickel base superalloys, *International Materials Reviews*. Vol. 45(3), 2000, p. 109-129.
- 40) Richards, N.L. and Chaturvedi, M.C., The Influence of Minor Elements on the Weldability of an INCONEL 718-Type Superalloy, *Metall. Mater. Trans.* Vol. 33A (7), 2002, pp. 2005-2017A.
- 41) Kou, S. Solidification and liquation issues in welding, *JOM*, NY, Vol.55 (6) 2003, p37-42.
- 42) Radhakrishnan, B; Thompson, R G. Solidification of the Nickel-Base Superalloy 718: a Phase Diagram, *Metall. Trans. A*. Vol. 20A, 1989, pp. 2866-2868.

- 43) Knorovsky, G.A., Cieslak, M.J., Headley, T.J, Romig,A.D., Jr. and Hammetter, W.F, Inconel718: A solidification Diagram, Metall. Trans. Vol.20A,1989,pp2149-2158.
- 44) Thompson, R.G and Genculu, S., Microstructural evolution in the HAZ of Inconel 718 and correlation with the hot ductility test, Welding Journal. Vol. 62(12), 1983, p. 337s-345s.
- 45) Vincent, R. Precipitation around welds in the nickel-base superalloys, Inconel 718, Acta, metal. Vol.33 (7), 1985, p1205-12126.
- 46) Baeslack, WAIII; Nelson, D E, Morphology of Weld Heat-Affected Zone Liquation in Cast Alloy 718, Metallography. Vol.19(3),1986, p. 371-379.
- 47) Radhakrishnan, B and Thompson,R.G, A quantitative microstructural study of intergranular liquation and its relationship to hot cracking, Metallography. Vol.21(4), 1988, p 453-471.
- 48) Chaturvedi, M.C. and Richards, N.L. Microstructures and HAZ cracking of EB welded Incoloy 903, Inter. J. Mater. Product. Tech. (Switzerland). Vol.11,(3-4), 1996,p. 253-270.
- 49) Thompson, R.G., Mayo, D.E. and Radhakrishnan, B., The relationship between carbon content, microstructure, and intergranular liquation cracking in cast nickel alloys 718, Metall. Trans. Vol.22A(2),1991,p557-567.
- 50) Huang, X; Chaturvedi, M C; Richards, N L; Jackman, J., The effect of grain boundary segregation of boron in cast alloy 718 on HAZ microfissuring--a SIMS analysis, Acta Mater. Vol. 45 (8), 1997, p.3095-3107.

- 51) Guo, H, Chaturvedi, M.C., Richards, N.L., Effect of nature of grain boundaries on intergranular liquation during weld thermal cycling of nickel base alloy, Science and Technology of Welding and Joining. Vol. 3 (5), 1998, p.257-259.
- 52) Ernest, S.C., Baeslack, W.A. and Lippold, J.C. Weldability of high-strength low-expansion superalloys, Welding Journal. Vol. 68 (10), 1989, p. 418s-430s.
- 53) Thompson, R.G., Radhakrishnana,B. and Mayo, D.E., Intergranular liquid formation, distribution and cracking in the HAZ of alloy 718 weld, in Superalloy 718- Metallurgy and Application, ed. Loria, E.A., The minerals, metal & materials society ,1989,pp437-455.
- 54) Radhakrishnan, B; Thompson, R G, Liquid Film Migration (LFM) in the Weld Heat Affected Zone (HAZ) of a Nickel-Base Superalloy, Scr. Metall. Mater. Vol. 24(3),1990, p. 537-542.
- 55) Nakkalil, R., Richards, N.L. and Chaturvedi, M.C., Grain Boundary Liquid Film Migration During Welding of Incoloy 903, Scr. Metall. Mater. Vol. 26 (10), 1992, p.1599-1604.
- 56) Chaturvedi, M. C., Richards, N L, Microstructures and HAZ cracking of EB welded Incoloy 903, Int. J.of Materials and Product Technology. Vol. 11 (3-4), 1996, p. 253-270.
- 57) Ojo, O.A., Richards, N.L., Chaturvedi, M.C., Liquid film migration of constitutionally liquated gamma' in weld heat affected zone (HAZ) of Inconel 738LC superalloy, Scr. Mater. Vol. 51 (2), 2004, p. 141-146.

- 58) He, X L; Djahazi, M; Jonas, J J; Jackman, J, The Non-Equilibrium Segregation of Boron During the Recrystallization of Niobium-Treated HSLA Steels, Acta. Metall. Mater., Vol. 39 (10), 1991, p. 2295-2308.
- 59) McLean, M; Strang, A, Effects of Trace Elements on Mechanical Properties of Superalloys, Met. Technol. Vol. 11, no. 10, pp. 454-464. Oct. 1984.
- 60) DuPont, J.N. Robino,C.V. Marder, A.R. and Notis, M. R. Solidification of Nb-bearing superalloys :Part II, pseudoternary solidification surfaces, Metall. Metar. Trans. Vol. 29A, 1998,pp2797-2806.
- 61) Williams, J. A. and Singer, A. R. E., Deformation, strength, and fracture above the solidus temperature, J. Inst. Metal, Vol.96,1968, p5-12.
- 62) Radavich J.F., The metallurgy of cast and wrought alloy 718, superalloy 718-metallurgy and applications. Ed. Lorida,E. A., 1989, pp229-240
- 63) DuPont, J.N. Robino,C.V. Marder, A.R. and Notis, M. R. Solidification of Nb-bearing superalloys :Part I, Reaction sequences, Metall. Metar. Trans. Vol. 29A, 1998,pp2785-2797.
- 64) Radhakrishnan, B and Thompson,R.G., A phase diagram approach to study liquation cracking in alloy 718, Metall. Trans.A, Vol.22A,1991,p887-902.
- 65) Lippold, J. C. "An investigation of heat-affected zone hot cracking in alloy 800" Welding J. Vol. 62, 1983, pp1s-11s.
- 66) Kijanpaa, V. P, David, S A and White, C L "Characterization of Heat-Affected Zone cracking in Austenitic stainless steel welds" Welding J. Vol.66, 1987, pp221s-228s.

Reference

- 67) Easterling, K. Introduction to the physical metallurgy of welding, Butterworth-Heinemann Ltd., Oxford, pp18-19.
- 68) Richards, N. L., Chaturvedi, M.C. and Liu, Y. G. and Mount, K, Optimization of electron beam welding parameters for Incoloy 903. Inter. J. Materials and Product Technology. Vol.11, 1996, pp284-299.